ucc

Coláiste na hOllscoile Corcaigh, Éire
University College Cork, Ireland

Atomic layer deposition and electrochemical characterization of TiO_2 as a potential candidate for a photoanode protective layer

Submitted by

Micheál Shine

For a Master of Science

Submitted to University College Cork, Ireland

Tyndall National Institute

Supervisor: Dr Ian Povey, Tyndall National Institute

Head of School: Prof. Anita McGuire, University College Cork

September 2024

Abstract

The search for alternative fuel sources has become more prevalent in recent years due to increasing energy demands as well as the detrimental effects fossil fuels have on the environment. Solar water splitting using semiconductor photoelectrochemical cells has long been viewed as a potential means of large-scale H_2 production from renewable resources.

A study was carried out to test the corrosion resistance performance of thin TiO_2 layers deposited by means of atomic layer deposition under oxidative conditions. Despite Silicon being considered one of the most promising semiconductors for use in photoelectrodes, its instability in aqueous solutions is one of its main limiting factors. TiO_2 film (~6 nm) were deposited on the anode surface, using atomic layer deposition and plasma enhanced atomic layer deposition (ALD), to act as corrosion protection and to passivate the electrode surface along with a 5 nm Nickel over layer to act as an oxygen evolution catalyst. The longevity of these photoanodes was the main focus of this work employing the techniques of cyclic voltammetry and chronoamperometry to evaluate electrochemical performance. Electron microscopy SEM was carried out, before and after the anodes underwent electrochemical testing, to gain insight into any surface degradation and morphological changes of the TiO_2 and Ni layers that may influence charge transfer and performance. Comparisons were drawn between photoanodes prepared by ALD and plasma enhanced atomic layer deposition (PE-ALD) to give a clearer picture of the limiting factors of charge carrier mobility and photoactivity. The estimated ratio of Ti^{3+} to Ti^{4+} and hence the oxygen vacancies, played an important role in the overall conduction of the device along with the % composition of impurities present due to incomplete reactions in the deposition process. This was tested by producing films with different oxygen doses during the deposition stage.

Contents

List of abbreviations

EM	electromagnetic radiation
PEC	photoelectrochemical cell
CB	conduction band
VB	valance band
V_{SC}	short-circuit voltage.
SBH	Schottky barrier height
PV	photovoltaic
QE	quantum efficiency
V_{OC}	open-circuit potential
R_s	series resistance
Mpp	maximum power point
FF	fill factor
PCE	power conversion efficiency
RHE	reversible hydrogen electrode
SCE	saturated calomel electrode
SHE	standard hydrogen electrode
OER	oxygen evolution reaction
HER	hydrogen evolution reaction
CER	chlorine evolution reaction
VBM	valance band maximum

CBM	conduction band minimum
DSSC	dye sensitized solar cell.
TMD	transition metal dichalcogenide
NM	noble metals
ALD	atomic layer deposition
CVD	chemical vapor deposition
ALE	atomic layer epitaxy
PEALD	plasma enhanced atomic layer deposition.
GPC	growth per cycle
UV	ultraviolet

Thesis motivation

As technology advances and population grows, the global energy demands are increasing while the fossil fuel reserves are depleting. The burning of these fuels also produces carbon dioxide, methane, nitrous oxide among others, which has a detrimental effect on the environment as well as the protective layers of the atmosphere. The ultimate goal is to reduce dependence on non-renewable fuel sources and shift the global energy supply to a more sustainable models. Hydrogen has long been a candidate for an alternative fuel source due to its abundance in the atmosphere in the form of H_2O and within the earth's crust in the form of fossil fuels such as natural gas, CH_4. Hopes for hydrogen powered vehicles were high in the 00's with some scientists predicting as much as 1.8 million H_2 vehicles sold by the year 2020 [1].

Currently, the majority (up to 95%) of the world's hydrogen is produced from fossil fuels by the oxidation of methane in a process called steam reforming [2]. The electrolysis of water is another alternative means of obtaining molecular hydrogen but requires mass amounts of energy to produce on a large scale. This has lead researchers around the world to pursue a cost effective and more renewable method of water splitting. In order to reduce production costs, researchers turned to solar-to-hydrogen systems which take advantage of the photovoltaic effect and use direct sunlight to aid or completely power this water splitting process. However, current materials demonstrated to initiate and maintain the dissociation of water are rare and expensive leading researchers to scale down the quantities required or find alternatives. The efficiencies of these systems depends on a lot of factors, for example, the stability of materials used, the electrolyte and amounts of sunlight available. Regardless of its abundance and relative safety, hydrogen cannot compete with fossil fuels due to the precious or noble metal catalysts and large amounts of energy required to produce it on a mass scale [3]. In order to make hydrogen readily available, a cheaper hydrogen harvesting alternative is required to properly realise the potential of hydrogen power.

Silicon is considered a promising material in the field of photoelectrochemical hydrogen production. Due to its high abundance and desirable bandgap (~1.12eV). This bandgap allows Si to absorb a wide range of the solar spectrum which is beneficial when trying to obtain a high photovoltage yield. However, Si on its own cannot be used in photoelectrochemical cells on its

own due to its instability in aqueous solutions. Thin layers of metal oxides such as TiO2 have been known to act as a protective and even catalytic layer when deposited on top of Si at the interface between the Si and the aqueous electrolyte. The aim of the following work is to gain more insight into how TiO2 performs as a protective layer under oxidative conditions within a photoelectrochemical cell.

Thin films are usually employed in order to allow the charge transport from the electrolyte through the thin film and also to allow the impinging light to penetrate the TiO_2 and reach the underlying Si. photoelectrochemical tests will also be carried out on films of different thickness to determine the nominal oxide thickness for the two mentioned conditions of a) charge transport and b) light penetration. Charge transport through the TiO_2 can heavily depend on phenomena such as oxide vacancies or site defects within the material. For this reason, TiO_2 deposited using varying oxygen concentrations is another area of interest and will investigate the degree to which oxygen vacancies plays a role in the resistivity of the protective layer.

The stability and charge transport ability of the TiO_2 passivation layer are the main focus of the following work and so electrochemical testing such as cyclic voltammetry and chronoamperometry will be employed to investigate this.

Initially, the focus of this study was meant to be on the performance of Ruthenium oxide as a catalytic layer for p+n photoanodes. This work commenced at the start of 2020 and was thus interrupted promptly by Covid-19. Due to the restrictions, There was little to no access to the lab until the following year in April 2021. Even at this time, access was still restricted and as is the nature with the $Ru(EtCp)_2$ precursor it had seemed to be decomposed within the container. Supply issues and time restraints meant that the focus of the work would switch to TiO2 instead, along with the study of the different types of underlying silicon.

Chapter 1

1. The Photoelectrochemical Cell

1.1 Hydrogen as fuel source

As technology advances and population grows, global energy demands are increasing while the fossil fuel reserves are depleting. The burning of these fuels also produces carbon dioxide, methane, nitrous oxide among others, which has a detrimental effect on the environment as well as the protective layers of the atmosphere. The ultimate goal is to reduce dependence on non-renewable fuel sources and shift the global energy supply to a more sustainable models. Hydrogen has long been a candidate for an alternative fuel source due to its abundance in the atmosphere in the form of H_2O and within the earth's crust in the form of fossil fuels such as natural gas, CH_4. Hopes for hydrogen powered vehicles were high in the 00's with some scientists predicting as much as 1.8 million H_2 vehicles sold by the year 2020 [1]. While pressurized hydrogen can be dangerous and can be explosive when in contact with a naked flame or spark, one of the advantages it has over petrol or diesel is that it is lighter than air. This can allow it to simply be purged into the atmosphere in a case of emergency while also not pooling around the vehicle as in the case of liquid carbon based fuels. Electricity produced using intermittent renewable sources like wind and solar can also use hydrogen production as a medium for storage which can then be used at a later date [1] . Currently, the majority (up to 95%) of the world's hydrogen is produced from fossil fuels by the oxidation of methane in a process called steam reforming [2]. The electrolysis of water is another alternative means of obtaining molecular hydrogen but requires mass amounts of energy to produce on a large scale. This has lead researchers around the world to pursue a cost effective and more renewable method of water splitting. In order to reduce production costs, researchers turned to solar-to-hydrogen systems which take advantage of the photovoltaic effect and use direct

sunlight to aid or completely power this water splitting process. However, current materials demonstrated to initiate and maintain the dissociation of water are rare and expensive leading researchers to scale down the quantities required or find alternatives. The efficiencies of these systems depends on a lot of factors, for example, the stability of materials used, the electrolyte and amounts of sunlight available. Regardless of its abundance and relative safety, hydrogen cannot compete with fossil fuels due to the precious or noble metal catalysts and large amounts of energy required to produce it on a mass scale [3]. In order to make hydrogen readily available, a cheaper hydrogen harvesting alternative is required to properly realise the potential of hydrogen power.

1.2 Photo electrochemical Cell

The first solar cell (photovoltaic) was designed by Edmond Becquerel shortly after his discovery of the photovoltaic effect in 1839. Solar cells are split into two classes, the first being a photovoltaic cell which produces electrical energy and a photoelectrolytic cell which uses incident light to cause a chemical reaction. Both of these devices are types of solar cell with the ability to convert incident electromagnetic radiation either directly into electrical power or initiate and sustain a chemical reaction to produce something which and be stored and later converted into electrical power (in this case hydrogen) [4]. This was first carried out by Fujishima and Honda in 1972, where the splitting of water molecules into oxygen and hydrogen ions by means of a photoelectrochemical reaction was carried out successfully using a TiO_2 photo anode.

The objective of a photo electrochemical cell (PEC) is to convert light energy from the sun into electrical/chemical energy by means of the photovoltaic effect which is shown in figure 1.3. This effect can be characterized as light being absorbed by a semiconductor material causing excitation of an electron, or other charge carriers, to a higher energy state resulting in the flow of a current. Each semiconductor material is characterized by its definite threshold energy or bandgap energy U_g which corresponds to the amount of external energy required to promote an electron from the valence band to the conduction band. The incident light from the sun consists of "quanta" of energy called photons which only interact with a single charge carrier in the material. It is only when

photons of light equal to or greater than the bandgap illuminate the material that charge carriers are promoted to the conduction band and are available to conduct electricity. [5]

1.2.1 Light Absorption

Semiconductors are a class of material which are often characterized by the position of their energy bands with respect to each other. This separation between the conduction and valence bands is called the bandgap E_g which is given by:

$$E_G = E_C - E_V \tag{1.1}$$

This bandgap is the lowest change in energy required to excite a charge carrier enough so that it can be liberated and participate in conduction. For semiconductors, in general, this bandgap is <4eV which falls within the range of radiation from the sun. The higher the bandgap the more energy it needs to absorb to excite the electron, but this also means that there will be more energy available for a reaction. For a semiconductor to absorb light, the incoming photon energy must either be equal to or greater than the bandgap energy E_G of the semiconductor:

$$E_G \leq E_\lambda \tag{1.2}$$

$$E_\lambda = \frac{hc}{\lambda} \tag{1.3}$$

Where h is Planck's constant, c is the speed of light and λ is the wavelength of the incident light. The sun emits EM radiation across most of the electromagnetic spectrum as can be seen in figure 1.2. The spectral irradiance of the sun is the most intense for the visible range ~ 380-750 nm which corresponds to 3.26 eV and 1.65 eV respectively. At wavelengths shorter than this, the ultraviolet region, the intensity of light decreases dramatically and makes up only ~ 8% of the total incident light. As previously mentioned, this light is not as abundant but because of its smaller wavelength it has a higher energy and is more energetic than light from the visible spectrum.

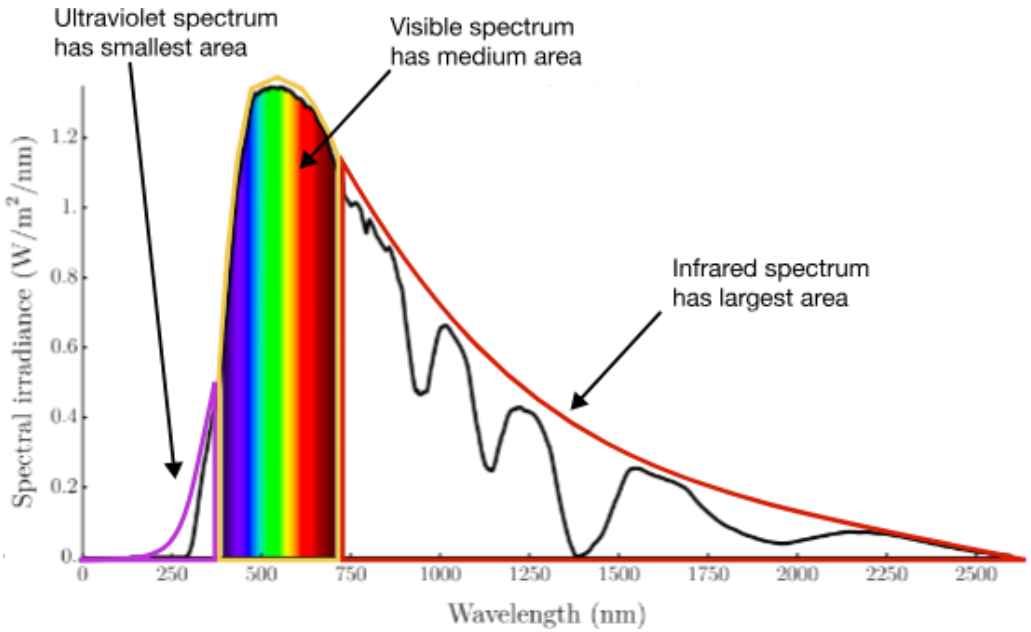

Fig 1.1: The solar spectrum with the three different regions labelled [94]

To make water-splitting viable, theoretically the bandgap of the semiconductor should at least be 1.23 eV but considering the losses due to kinetics, the bandgap should ideally be greater than 2 eV. In order to access a wider portion of the solar spectrum a 2 photo-electrode system can be employed, using semiconductors with differing bandgaps . For example, as demonstrated in [6], by careful selection of the bandgaps a two electrode system can be engineered, here short wavelength light was absorbed by an n-type semiconductor anode and the longer wavelengths passed through to be absorbed by a p-type cathode. One of the main small bandgap semiconductors used in the field is Silicon (1.1 eV) which can absorb wavelengths of up to 1120 nm whereas TiO_2, for example is a wide bandgap semiconductor with a bandgap ranging between 3-3.4 eV (depending on its morphology) [7]. Combining these two materials and utilizing their best properties can produce an oxidatively robust and efficient photoanode for water oxidation.

1.2.2 Semiconductor-electrolyte interface

A quantity of huge importance when it comes to semiconductors and PEC is the Fermi level. This Fermi level E_F signifies the energy level where the probability of charge occupancy is exactly 0.5. For intrinsic semiconductors this level would lie directly in the middle of the CB and VB because the number of holes and electrons is equal. In the case of doped semiconductors, this leads to a shift in the Fermi level depending on which dopant is present. An n-type semiconductor would have electrons as its majority charge carrier which would shift the Fermi level towards the conduction band while for a p-type semiconductor the shift would be towards the valence band edge as seen in figure 1.2. Figure 1.2(a) shows the energy level band diagram for a semiconductor (left) and a redox electrolyte (right) isolated from each other with respect the vacuum level. The χ represents the electron affinity while the φ represents the work function of the material. The two distribution functions re and ox on the right signify the density of ionic energy available for reduction and oxidation which overlap at the redox Fermi potential E^{O}_{Redox}. When a semiconductor is immersed in an electrolyte, the Fermi levels will sync up and match each other. In order for the interface to equilibrate a flow of charge from the higher Fermi level material to the lower is required which causes "band bending" within the semiconductor material. The before and after contact band diagrams are shown below in figure 1.2(b) and (c) for an n-type and p-type semiconductor respectively. This band bending results in a built in voltage in the system called V_{SC} as can be seen on the right hand side of the diagram. The excess charge does not lie on the surface but instead extends into the electrode to create an area called the space charge region/layer which has an associated electric field. This charge transfer results in charge of opposite signs accumulating at and near the interface. The nature of this charge distribution causes band bending within the electrode. For p-type semiconductors, an accumulation of excess positive holes gather at the interface which in turn is compensated by an accumulation of negative ions in the electrolyte. [8] The built in electric field, otherwise called the depletion region is characterized by the width that the field penetrates into the semiconductor called the depletion width w which can be determined using the equation:

$$w = \sqrt{\frac{2\varepsilon_o \varepsilon_r}{eN_D}(V_{sc} - \frac{k_b T}{e})} \tag{1.4}$$

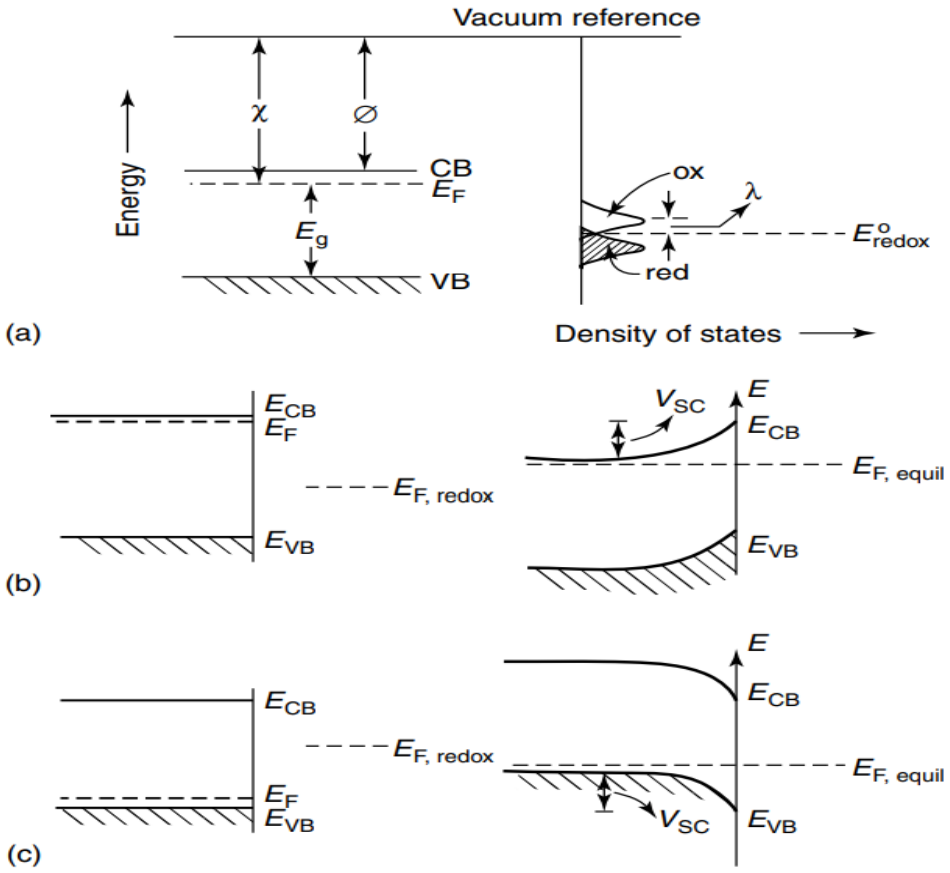

Figure 1.2: (a) the energy band diagram of an isolated semiconductor (left) and a redox electrolyte (right) (b) an energy band diagram of a semiconductor-electrolyte interface before (left) and after (right) reaching equilibrium for an n-type semiconductor and (c) energy band diagram before and after equilibrium for a p-type semiconductor [9]

Where ε_o and ε_r are the dielectric constant of vacuum and the material respectively, e is the electron charge, V_{sc} is the total amount of charge in the depletion region, N_D is the donor density, k_b is Boltzmann's constant and T is the temperature. From equation 1.4, it can be determined that the depletion layer width is dependent on the donor density. The applied voltage also plays a part in this with increasing the applied voltage resulting in increasing band bending. Each system will also have a flatband potential which is the potential that is applied in order for there to be no band bending [9].

1.3 PEC Operating principle

A PEC consists of 3 main components a cathode and anode which are connected by a metal wire and an electrolyte to carry the current between both electrodes. Initial development of a solar cell operating on the photovoltaic effect was credited to Alexander-Edmund Becquerel in 1839 when he discovered current flowing when a silver chloride coated electrode was illuminated by sunlight. He predicted that this current resulted from a chemical reaction at the electrode/electrolyte interface [10]. This phenomenon was first used in the electrolysis of water by Fujishima and Honda in 1972 where the splitting of water molecules into oxygen and hydrogen ions by means of a photo electrochemical reaction was carried out successfully. These early PEC cells used a simple semiconductor-liquid junction which had a critical dependence on the stability of the semiconductor material, due to constant oxidation/reduction, and the power conversion efficiency, which was also heavily dependent on the properties of the constantly changing semiconductor interface in the redox reaction environment [11] [12]. The PEC cells developed which used the photovoltaic effect can be split into two main categories, p-n junction and Schottky junction solar cells both of which primarily use silicon as a semiconductor.

The five main process which occur within a PEC are light absorption, charge separation, charge migration, charge recombination and redox reactions which can be seen in figure 1.3(a).

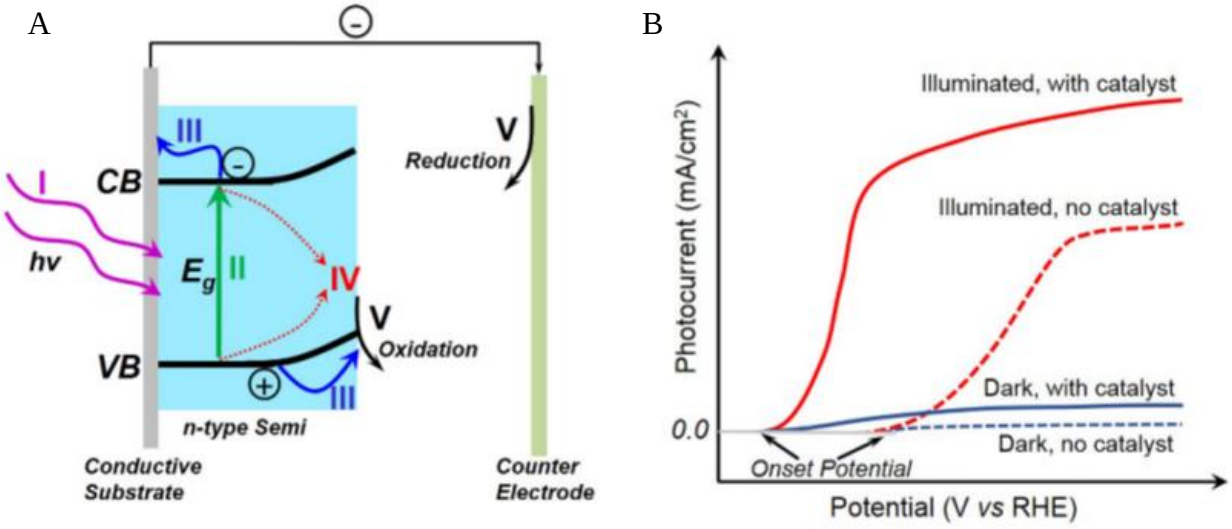

Figure 1.3: Schematic of (a) a photoelectrochemical cell utilizing an n-type photoelectrode which illustrates the five main elements that constitute the water splitting process (I) absorption (II) charge separation (III) charge migration (IV) charge recombination and (V)redox reaction and (b) the photocurrent density-voltage sweep of an n-type photoanode [98]

Conventional *p-n junction solar* cells are constructed using either homogenous or heterogeneous materials with the operating principal being the same. In heterotypic cells, the pn junction is the boundary area between the p-type and n-type material within the depletion region or "space charge region" shown in figure 1.4. In equilibrium, the free electrons from the n-type material diffuse over to the p-type while the p-type holes diffuse to the n-type region, like charges repel creating a region with an electric field that is free of mobile charges called the depletion region. When incident light is absorbed by the semiconductor it will dislodge an electron and mobile hole which then travel to the n-type region and p-type regions, respectively. It is this potential difference which drives the current produced by the photovoltaic effect.

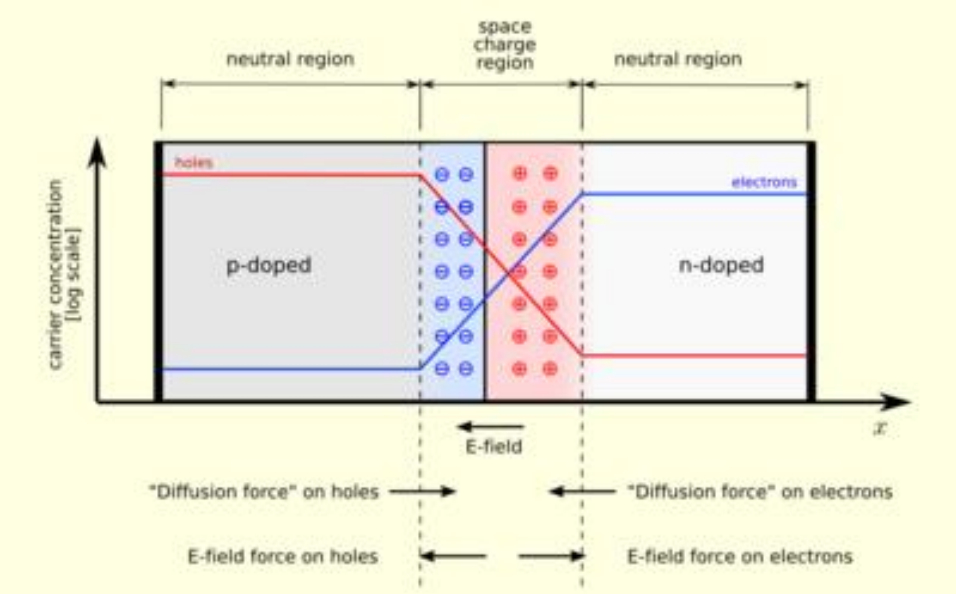

Figure 1.4: Schematic of a pn junction in equilibrium with zero bias voltage applied showing the neutral regions and the space charge region in the middle caused by the interface of n & p type regions[97]

A *Schottky Junction* is formed at the interface between a metal and semiconductor and causes the band-bending which is necessary for charge separation .This separation is due to the differing energy between the Fermi levels in both the metal and semiconductor. This effect works in a similar but opposite way for both n-type and p-type semiconductors. In the case of the n-type material in equilibrium, electrons will begin to flow from the metal and semiconductor causing a bending of the band structure (figure 1.2). The degree to which this band bends is called the Schottky barrier height SBH and is a direct measure for the mismatch of energy levels of the majority carriers between the metal and semiconductor. This name comes from the famous Schottky-Mott relationship that states:

$$\Phi^{0}_{B,n} = \varphi_M - \chi_S \qquad (1.5)$$

Where φ_M is the work function of the metal and χ_S is the electron affinity of the semiconductor. This working electrode can be the anode or the cathode part of the circuit depending on what the majority charge carrier of the material is. In a traditional water splitting PEC with a working anode, incident light excites electrons which can then travel to the cathode leaving behind positive holes.

These holes are available to combine with oxygen ions in the water to produce oxygen gas while at the cathode, the electrons combine with hydrogen ions producing hydrogen gas.

Several methods can be used for the photo generation of hydrogen vastly ranging in both price and complexity of the system. These systems range from separate PV cells with electrolysers, which separate the photovoltaics from the electrolysis system to wireless configurations that employ integrated cathode/anode systems where the light absorbing panel is directly submerged in water and the redox reactions occur at the electrode surfaces[6]. The main advantage of the latter technique is the cooling effect the electrolyte has on the semiconductor allowing for a constant and high photo voltage to be produced while simultaneously heating the electrolyte which lowers the reaction over potential allowing the use of more of the solar spectrum [13]

By evaluating each step of the PEC system namely, light absorption, charge separation, charge migration, charge recombination and redox reactions one can calculate the cells quantum efficiency *QE* which relates the cells produced photocurrent density J_{SC}, to the incident light spectrum. J_{SC} denotes the short circuit current which is the current through the cell when the potential across the cell is zero. J_{SC} is due solely to the generation and collection of light generated carriers and is therefore the maximum current produced by a solar cell. This photocurrent density can be written as:

$$J_{SC} = q \int b_s(E) QE(E) dE \qquad (1.6)$$

Where q is the charge on an electron, $b_s(E)$ is the spectral photon flux density and QE(E) is the quantum efficiency and E to E+dE is the energy range of photons which fall on the area of the anode per unit time. [14]

The photocurrent produced is actually a reverse bias current because electrons flow towards the cathode while the positive holes flow towards the anode. If a forward bias was applied it would compensate for the reverse photocurrent which will eventually turn the current flowing to zero, this is shown below in equation 1.7. The point at which this is achieved is called the open-circuit voltage or V_{OC}. The ideal diode (Shockley) equation gives:

$$J_{Dark} = J_0 \left((e^{\frac{q(V-JR)}{K_B T}} - 1) \right) \quad (1.7)$$

Where J_0 is the Saturation current density, k_B is the Boltzmann's constant, V is the applied voltage and T is the temperature in Kelvin. The total current in a solar cell can be expressed as the difference between the current density produced with and without illumination i.e. $J_{Total} = J_{Dark} - J_{Light(SC)}$ and thus:

$$J_{Total} = J_0 \left(e^{\frac{q(V-JR)}{K_B T}} - 1 \right) - J_{SC} \quad (1.8)$$

$$J_{Total} = J_{SC} - J_0 \left(e^{\frac{q(V-JR)}{K_B T}} - 1 \right) \quad (1.9)$$

Where J is the total current density, J_0 is the saturation current density K_B is the Boltzmann's constant and V is the voltage across the diode. Figure 1.7 shows the typical Current voltage characteristic for a solar cell. Solving equation 1.9 for V then gives:

$$V = \frac{K_B T}{q} \ln \left(\left(\frac{J}{J_0} \right) + \left(\frac{J_{Light}}{J_0} \right) + 1 \right) + J(RA) \quad (1.10)$$

Where R is the series resistance in ohms and A is the cross sectional area of the device. By setting J to 0 and V to V_{OC} in equation 1.10, the open circuit voltage can be obtained:

$$V_{OC} = \frac{k_B T}{q} \ln \left(\frac{J_{SC}}{J_0} + 1 \right) \quad (1.11)$$

The J_L and J_{SC} terms denote the internal current produced within the solar cell and the short circuit current respectively. Since at short circuit conditions these values are equal so the terms can be used interchangeably. Equation 1.11 above shows ideal diode conditions where the series resistance is negligible and so in the case of an increasing series resistance these values tend to stray further from each other [14]. This series resistance R_s is the cell materials resistance to current

flow, contact resistance at differing material interfaces and the resistance of the metal contacts and increases with increasing current density. Shunt resistance R_{SH} is another form of resistance incorporated within the solar cell which runs parallel to the solar cell as seen below in the simplified solar cell diagram, figure 1.5. This is caused by a diversion of the charge carriers due to manufacturing/ material defeats and/or leakage of current at the edges of the cell which diverts current from the cell itself reducing the voltage produced. As opposed to series resistance, the effect of shunt resistance is particularly severe at low levels of illumination, since the light generated current will be low.

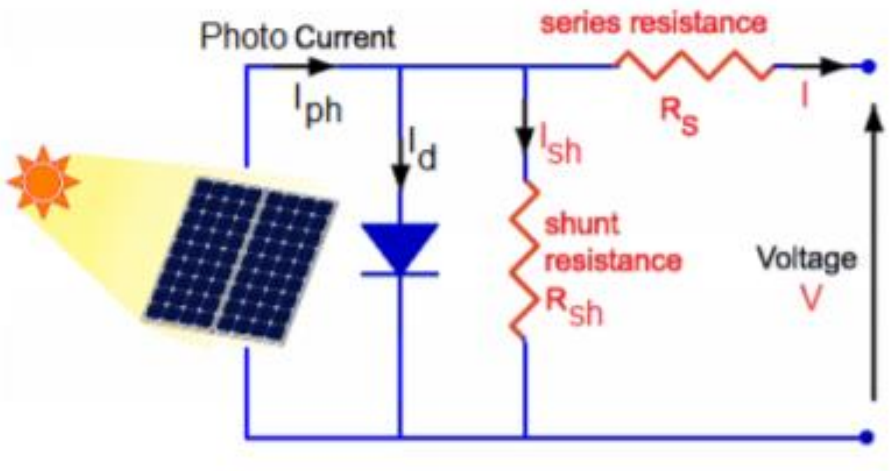

Fig 1.5: Simplified circuit diagram of a typical solar cell [16]

With regards figure 1.5, in order to ensure the maximum amount of current travels through the diode a large shunt resistance is required along with a small series resistance. For a non-ideal diode with the shunt and series resistance incorporated, the total current density is now given as:

$$J = J_{Light} - J_{Dark} - J_{Sh} \tag{1.12}$$

Where J_{SH} is the current density leaking through the shunt resistance. This term is obtained by dividing the ideal diode voltage by the shunt resistance. Using the above equation 1.12 (for total J) and our term for J_{Sh} :

$$J_{Sh} = \frac{V + JR_s}{R_{Sh}} \tag{1.13}$$

$$J = J_{Sc} - J_0\left(e^{\frac{q(V+JR_s)}{nK_BT}} - 1\right) - \frac{V + JR_S}{R_{Sh}} \tag{1.14}$$

Where n is the diode ideality factor. This expression gives the overall current under illumination of a solar cell device. The graphical representation of the JV characteristic for a solar cell is shown in figure 1.6 and, as can be seen, the cell acts as a current source at short circuit and as a voltage source near the open circuit point [15]. An increase in the series resistance will result in a decrease the short circuit current density while an increase in the shunt resistance will increase the open circuit voltage [16].

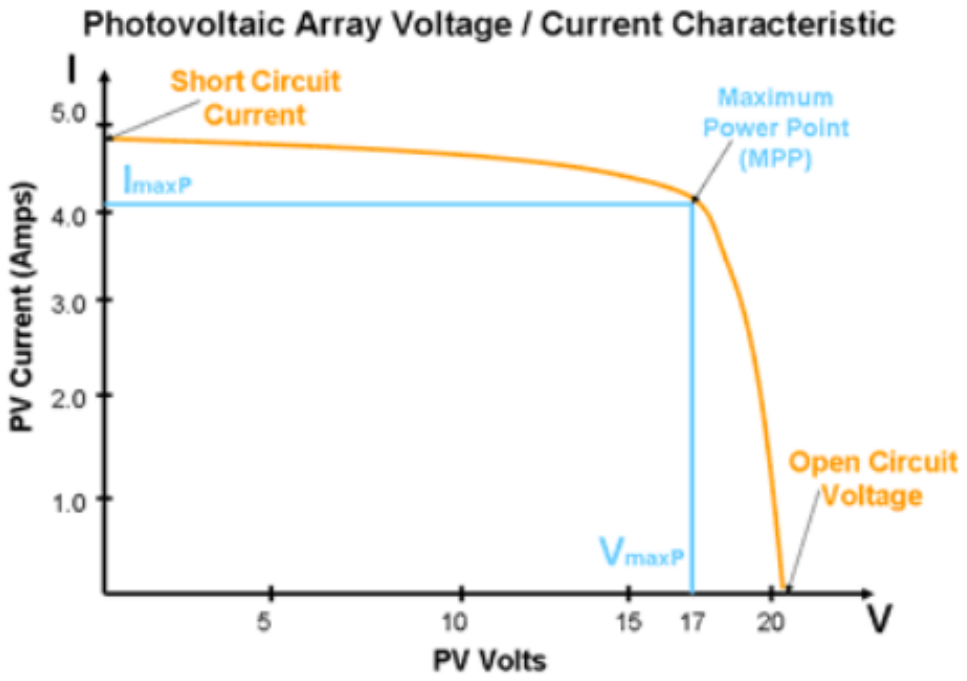

Fig 1.6: Current/voltage characteristic of a typical solar cell. Where MMP indicates the point at which a cell is at its minimum power output. [95]

The point on this curve (fig 1.6) where the power output of the device is at a maximum is of particular interest and is referred to as the maximum power point *mpp* where $V=V_{mp}$ and $J=J_{mp}$.

The mpp point defines a rectangle whose area is $P_{mp} = V_{mp}J_{mp}$ and is the largest rectangle which can be made from any point on the JV curve. The outer rectangle defined by V_{OC} and I_{SC} can be used in conjunction with the inside rectangle to describe the available power at the maximum power point of the cell. The fill factor is a ratio of the maximum power output of the cell to the ideal cell output. The fill factor or FF is given by:

$$FF = \frac{V_{mp}J_{mp}}{V_{oc}J_{sc}} = \frac{P_{mp}}{V_{oc}J_{sc}}$$

The overall efficiency is defined as the ratio of the power produced by the cell to the power of the incident light on the cell. This can be calculated by rearranging equation 1.15 in terms of P_{mp} so:

$$\mu = \frac{Power\ Produced}{Incident\ Power} = \frac{P_{mp}}{P_{in}} \quad (1.16)$$

$$\mu = \frac{FFV_{oc}J_{sc}}{P_{in}} \quad (1.17)$$

Where μ is the overall power conversion efficiency or PCE. The incoming light radiation is also a key component to consider when designing a PEC and external quantum efficiency measurements are sometimes taken in order to assist in PEC material selection. This is defined as the number of charge carriers the solar cell collects to the number of incident photons that shine on the cell or:

$$EQE = \frac{electrons/sec}{photons/sec} \quad (1.18)$$

1.4 Water/Brine splitting

The photo electrochemical cell uses the solar cell configuration in order to turn photon energy into electrochemical energy which directly splits water into oxygen and hydrogen turning it into

chemical energy. The energy required for the overall reaction, seen below in equation 1.19, to split one molecule of H_2O into its constituent molecules H_2 and ½ O_2 is ~1.23V per electron transferred [17] . This requires the semiconductor within the PEC to absorb photons of energy > 1.23 V. The PEC's path to water splitting involves two separate reduction and oxidation half reactions which occur at the cathode and anode respectively. Three main conditions need to be met in order to do so, 1) Solar response of the PEC system must optically match the incident light spectrum 2) The produced photo charges must be separated efficiently in order to prevent recombination and loss of photocurrent 3) The excited charges must have sufficient energy to be able to carry out the water splitting reaction.

$$H_2O + hv \longrightarrow {}^{1}/_{2}\ O_2 + H_2 \qquad (1.19)$$
$$\Delta E = -1.23V \qquad vs\ RHE$$

This negative ΔE value indicates that this water cleavage reaction is not spontaneous and requires external energy to do so. The driving force behind this reaction is the photo voltage V_{ph}, which due to losses such as spontaneous emission and non-radiative recombination, will always be less than the material bandgap. These losses result in the V_{oc} being some 400-500mV below the bandgap E_g for almost all standard solar cells [18] [19]. This would suggest that E_g should be ≥1.63V and ideally much greater in order to run the redox reaction at a significant rate. A trade-off between bandgap energy and amount of light absorbed exists due to larger bandgaps not being able to absorb as much light. . Both the hydrogen evolution potential and oxygen evolution potential should ideally lie between the conduction and valence bands of the selected material. *Tamirat et al* compiled a graph of some semiconductor band edge positions relative to E_{NHE} and included the HER and OER potentials, figure 1.7 WO_3 for example, has a nominal bandgap of ~2.6eV however the conduction band is too positive to be able to perform and maintain the HER whereas in the case of CdSe the valence band is too negative [20]. Employing a tandem cell system, with an active photocathode and photoanode, can sometimes be advantageous when constructing a PEC because each of the semiconductors only need have one band suitable for each respective reaction (HER & CER). This will be discussed more in the following sections.

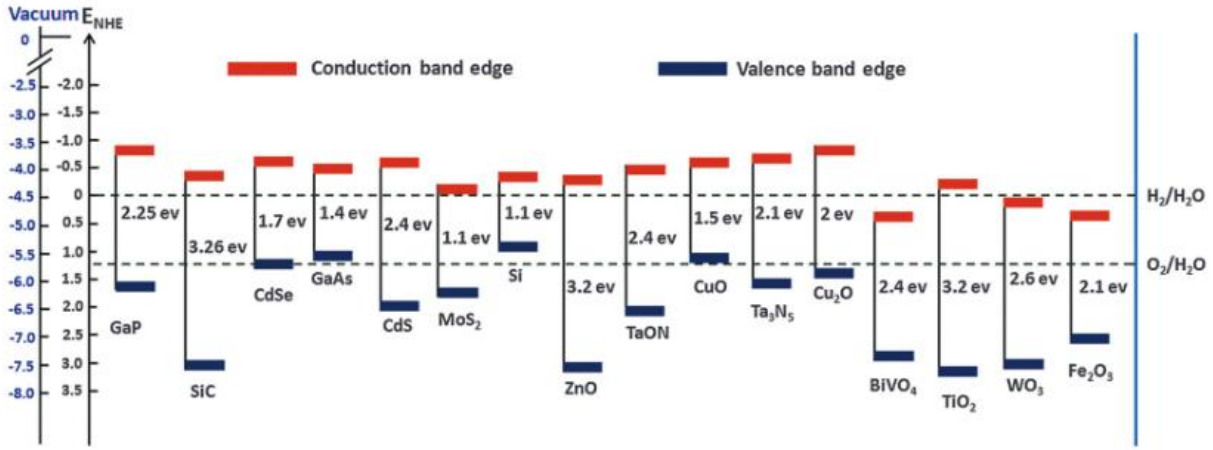

Figure 1.7 Band edges of semiconductors commonly used in Photoelectrochemical cells with respect to the Vacuum and NHE potentials. Water reduction and oxidation potentials are also marked by horizontal dashed lines [20]

Compared to the photo cleavage of water, the electrolysis of brine has not been as widely studied despite the numerous advantages associated with this reaction. Although the redox potential for the chlorine reaction requires a higher potential, ($E^{\circ}(O_2/H_2O)$=1.23V ($E^{\circ}(Cl_2/Cl^-)$=1.36V, the over potential is significantly reduced when compared to that of OER, ~50mV at 10mA cm^{-2}. This is partly due to the overall brine cleavage reaction requiring a two electron transfer as opposed to the four electron transfer in the overall H_2O splitting reaction [21]. The by-products from the oxidation of chlorine will be H_2 and, depending on the electrolyte pH and the presence of a separation membrane, either be chlorine gas or hypochlorite NaOCl. Either of these products can be used as a surface disinfectant and also to generate potable water. This does not come without its drawbacks however, as chlorine is a powerful oxidant, with a water solubility of ~ 0.092 mol dm^{-3} atm^{-1} , some 70 times stronger than water which will increase the oxidation and corrosion of cell components thus cementing the need for an optimal material with desired conductive and protective properties [22].

1.4.1 Photo-Catalysts:

The reaction kinetics at the electrolyte-semiconductor interface have a huge effect on the reduction or oxidation of water. While the materials above in figure 1.7 could be coupled with a platinum electrode to perform water oxidation/reduction, the overall solar-to-hydrogen efficiency would be low due to the slow kinetics of the multiple particle OER and HER and low photon absorption. The hole transfer across the anode-electrolyte interface should be fast enough to avoid the accumulation of charge at the interface which in turn can lead to the recombination of charge. To counteract this and minimize the losses, the photoelectrode is usually coated with a thin oxidation/reduction catalyst.

Water splitting as a whole is seen as a non-spontaneous or "uphill" reaction which means that as well as the 1.23V required for the oxidation of water, an additional activation energy is also required to initiate and maintain the reaction. [23] The role of a photocatalyst is to reduce this activation energy, which is referred to as the overpotential, by increasing the reaction kinetics at the interface. The binding energy of the catalyst must be in an optimal range for it to act as a good catalyst (Sabatier principle) meaning that if the interaction is too weak, the molecule will fail to bind to the catalyst and no reaction will take place but if it is too strong the products will fail to dissociate [24]. Platinum group metals such as Iridium and Ruthenium have showed some of the best results as catalysts for water oxidation but due to their high costs research has tried to minimise their use or find alternatives. A thin layer of Nickel over a protective layer on Si is widely used and has proved to be a very capable catalyst [25]. Nickel slows down the oxidation of the underlying Si while also exhibiting very high oxygen evolution activity in alkaline conditions [26]. In such alkaline conditions, the surface Ni can react with the OH^- to form NiOOH. This in turn makes Nickel the reactive surface species by following the reaction mechanisms:

$$Ni + 2OH^- \longleftrightarrow Ni(OH)_2 + 2e^- \quad (1.20)$$

$$Ni(OH)_2 + OH^- \longleftrightarrow NiOOH + e^- \quad (1.21)$$

This reaction is accompanied with a change in the surface Ni oxidation state from II^+ to III^+, which is the accepting of a hole from the anode surface in turn, allowing the catalyst to accept an electron from the electrolyte. Under these alkaline conditions the Ni may also undergo hydration leading

to the formation of a Nickel hydroxide layer on the surface which also exhibits high activity towards oxygen production [27]. The Ni-semiconductor interface forms a junction which promotes band bending which in turn favours the charge separation and motion of the photoexcited holes towards the catalyst-electrolyte interface. As well as this, the Ni film thickness can provide a degree of tunability of the built-in potential and photovoltage [28].

1.4.2 pH dependence

The redox potentials for water reduction and oxidation are heavily pH dependant. Ions must be present in order to conduct electricity through the electrolyte, which are H+ and OH- in the case of an acidic and alkaline electrolyte respectively. In general, acidic electrolyte is more favourable for the HER process due to the abundance of H+ ions. These ions associate with an electron in the solution and attach to the catalyst, combining with another adsorbed H* while also accepting an electron from the electrode producing hydrogen gas. Alkaline electrolyte does not have a high concentration of H+ ions and so the H-O-H bond needs to be broken before HER can commence which requires a higher energy than the reduction of H+. Conversely, an abundance of hydroxide ions is required to initiate the OER process which means that an alkaline electrolyte is more favourable for this step. These OH- ions reduce and attach to the catalyst where a second reduction occurs and results in the formation of a water molecule. This leaves adsorbed O* which bond to another adsorbed O giving off O_2 gas. Similar to the above case for HER, the breaking up of water molecules requires more energy than reduction of OH- ions and so, in general, OER prefers a more alkaline electrolyte [29].

1.4.3 Redox Reactions

1.4.3.1 Hydrogen Evolution Reaction

Once photoelectrons are released from the semiconductor material, they will migrate towards the cathode surface where they are free to react with intermediate hydrogen within the electrolyte. There are two widely accepted mechanisms for the HER process namely Volmer-Tafel and

Volmer-Heyrovsky both of which involve the Volmer step which describes the adsorption of Hydrogen ions on the electrode surface. This process is as follows:

In Acidic Solution:

$$2H_{aq}{}^{+} + 2e^{-} \longrightarrow H_{2(g)} \quad (1.22)$$

$$H^{+} + e^{-} \longrightarrow H_{ad} \quad (1.23)$$

$$2H_{ad} \longrightarrow H_2 \quad (1.24)$$

$$H^{+} + H_{ad} + e^{-} \longrightarrow H_2 \quad (1.25)$$

In Alkaline Solution:

$$2H_2O + 2e^{-} \longrightarrow H_{2(g)} + 2OH_{(aq)}{}^{-} \quad (1.26)$$

$$2H_2O + 2e^{-} \longrightarrow 2H_{ad} + 2OH^{-} \quad (1.27)$$

$$2H_{ad} \longrightarrow H_2 \quad (1.28)$$

$$H_2O + H_{ad} + e^{-} \longrightarrow H_2 + OH^{-} \quad (1.29)$$

Where H_{ad} represents adsorbed hydrogen atom on the cathode surface. Equation 1.22 and 1.26 represent the overall reaction while equations 1.23 – 1.25 and 1.27 – 1.29 represent the Volmer, Tafel and Heyrovsky mechanisms respectively. Note that for HER in an alkaline solution, dissociation of water is required and so the reaction rate is usually several orders of magnitude less than that of Acidic solution [30].

At low pH, the HER process occurs mainly by the reduction of protons while at high pH water is primarily reduced to form hydroxide ions [31]. Henceforth the reaction using acidic solution will be referred to because of its wider use and greater potential for water splitting. It is the second step that produces molecular Hydrogen and this can occur as a chemical or electrochemical reaction. This chemical reaction is known as the Tefel reaction where two adsorbed hydrogen atoms combine to form H_2 seen in equation 1.24. The electrochemical reaction, shown in equation 1.25, also known as the Heyrovsky reaction combines a proton, electron and adsorbed atomic hydrogen

to produce the molecular hydrogen [32]. Depending on the kinetics of each of the above reactions, one of them will ultimately be the rate determining step for HER. If proton adsorption (Volmer) is rate limiting for the process, increasing the available adsorption sites on the electrode surface by having more cavities and edges will help improve the electron transfer. If the desorption and diffusion of H_2 from the electrode is the rate limiting step, then a rougher or perforated surface will also increase the electron transfer by means of increasing reaction area and/or prevent bubbles from growing which would form an unwanted barrier [32]. The energy conversion efficiency of the HER, with the help of surface passivation, protective layers and catalysts, has achieved levels as high as 11.5% in recent years compared to previously achieved efficiencies of > 6% 15 years ago [33] [34] [35] [36]The standard reaction potential for the HER is ~0V.

1.4.3.2 Oxygen Evolution Reaction

The creation of an oxygen molecule at the photoanode requires the transfer of $4e^-$ and the removal of $4H^+$ from water which means the reaction rate for this step is usually very slow. This is one of the main reason preventing the widespread use and implementation of water splitting systems [37]. This low reaction rate is coupled with the fact that due to the highly oxidizing environment at the photoanode, the presence of thick oxide protection layers on silicon will further hinder the transport of the charge. However, the incorporation of photoactive materials into this protection layer can help reduce the bandgap and over potential and thus increasing the reaction rate. The following equations are the OER reactions in an acidic and alkaline solution:

In acidic media:

$$H_2O \Longleftrightarrow OH_{ads} + H^+ + e^- \tag{1.30}$$

$$OH_{ads} \Longleftrightarrow O_{ads} + H^+ + e^- \tag{1.31}$$

$$O_{ads} + H_2O \Longleftrightarrow OOH_{ads} + H^+ + e^- \tag{1.32}$$

$$OOH_{ads} + H_2O \Longleftrightarrow O_2 + H^+ + e^- \tag{1.33}$$

In alkaline media:

$$OH^- \Longleftrightarrow OH_{ads} + e^- \quad (1.34)$$

$$OH_{ads} + OH^- \Longleftrightarrow O_{ads} + H_2O + e^- \quad (1.35)$$

$$O_{ads} + OH^- \Longleftrightarrow OOH_{ads} + e^- \quad (1.36)$$

$$OOH_{ads} + OH^- \Longleftrightarrow O_2 + H^+ + e^- \quad (1.37)$$

As previously mentioned, OER has more is more complex and thus has more sluggish reaction kinetics due to the need for transfer of 4 e^- and removal of 4 H^+ from the water to produce one oxygen molecule. Noble metal based materials are usually required to maintain stable PEC OER in acidic media. Some of the main candidates for protective layers in the OER are namely RhO_2, IrO_2, RuO_2 , with IrO_2 being considered the most suitable due to its high photo activity and the lowest over potential for water splitting out of the current OER protective layers [38]. While these protective layers display ideal photo activity and conduction properties, an overlying catalyst such as Co or Ni may be required. While transition metals such as the aforementioned Rh, Ir, Ru are the ideal candidates for the photocathode, the high cost and low abundance of these metals requires them to be used sparingly and in conjunction with more abundant metals such as Ti, W and Ni.

1.4.3.3 Chlorine Evolution Reaction

Compared to the photo cleavage of water, the photo-electrolysis of brine has a smaller over potential partly due to the 2 electron transfer process as opposed to the 4 electron system of water [39] [40] However, because of its relatively high equilibrium potential (E◦(Cl2/Cl−) = 1.36 V) compared to that of water (E◦(O2/H2O) = 1.23 V) the CER process can be very energy intensive . Moreover, chlorine is an aggressive oxidant that could damage the semiconductor photo anode [21]. Another complication is there is a selectivity issue with a competing oxygen evolution side reaction in the same potential window as the CER which becomes more significant at higher current densities. The reversible electrode potential for CER is pH independent (but is dependent

on Cl_2 and Cl^- concentrations) as opposed to OER where the potential increases with a decrease in the electrolyte pH. The selectivity can therefore be shifted towards a preferred CER by keeping the pH of the electrolyte low and the Cl^-, Cl_2 concentrations high. *Sohrabnejad-Eskan et al*. concluded that the system is also temperature dependant through changes in electrolyte viscosity, half-cell reaction potential, exchange current density, reference electrode potential and also the overall selectivity of the OER and CER [41]. A variety of different mechanisms for chemisorbed intermediates have been proposed recently by Tilak and more recently *Rosestolato et al*. based on experimental analysis such as Tafel slopes and order of reaction [39] [42]. For the case of CER, The pathway is described by the Volmer-Heyrovsky mechanism [43] [44].

$$O_{ot} + 2Cl^- \longrightarrow OCl_{ot} + e^- + Cl^- \quad (1.38)$$

$$OCl_{ot} + e^- + Cl^- \longrightarrow O_{ot} + Cl_2 + 2e^- \quad (1.39)$$

Where the O_{ot} is the "on top" oxygen atoms on the electrode catalyst surface where adsorption can occur, in the case of CER, usually RuO_2. The adsorption of chloride from the electrolyte is described in the Volmer step which is followed by the recombination of an adsorbed species of chlorine with another incoming chloride ion in the electrolyte to form molecular chlorine (Heyrovsky). The CER over RuO_2 requires the formation of O_{ot} and OCl_{ot} intermediate adsorbates as seen above in equation 1.38. When deriving current-potential models for CER, the Volmer step is assumed to be in a quasi-equilibrium state and so the rate limiting step is either recombination or the electrochemical desorption of Cl_2 (equation 1.39).The current density is then dependent on surface coverage of the electrode by chemisorbed Cl_{ot} or Cl_2 in a similar fashion as with the OER reaction [37].

1.5 Stability

For an electrochemical cell to be viable for real world applications, the semiconductor within it must be stable in under water splitting conditions for prolonged periods of time. Photo-corrosion

is one of the main limiting factors with regards to PEC cells with the oxidation or reduction of the semiconductor itself often being in competition with the oxidation of water. Photo-passivation is also a limiting factor which occurs when the semiconductor reacts with oxygen in aqueous electrolytes and an oxide forms on the surface, thus passivating the surface making the surface inactive for water oxidation [45]. If corrosion happens, the extent of it depends heavily on the applied potential to the system as well as the pH of the electrolyte used. An Alkaline electrolyte tends to be favoured over an acidic one when using transition metal protective layers due to the formation of oxides or hydroxides in the latter [46].

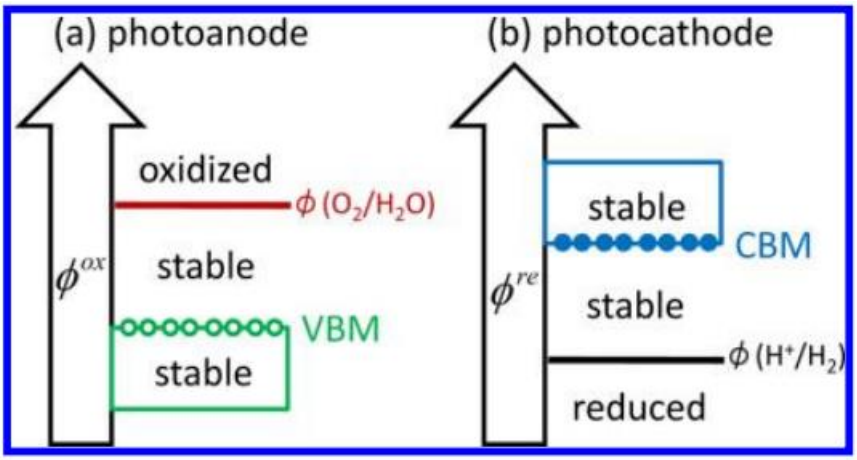

Figure 1.8: Diagram showing (a) how the stability of a photoanode will decrease as its oxidation potential shifts from its VBM (valance band maximum) to the water oxidation potential $\varphi(O_2/H_2O)$ and (b) how the stability of a photocathode will decrease as its reduction potential shifts from its CBM (conduction band minimum) to the water reduction potential $\varphi(H^+/H_2)$ [96]

The position of the band edges with respect to the water oxidation and reduction potentials also influence the stability of the anode. Since the photo-generated electrons can oxidize the material itself, the semiconductors alignment of its oxidation potential relative to the oxidation potential of water O_2/H_2O tells us about its resistivity to photo corrosion. In the case of a photocathode, it is the materials reduction potential position relative to the reduction potential of water H^+/H_2 that determines if this corrosion will occur as seen in figure 1.8 above. Figure 1.9 is similar to figure 1.8 but as well as the conduction (blue column) and valance band (green column) edges, it also includes the oxidation φ^{ox} (red bar) and reduction potentials φ^{re} (black bar) of each material [47]. As in figure 1.8 a material is considered stable against hole oxidation if its oxidation potential φ^{ox}

is lower than that of the oxidation potential of water O_2/H_2O or the valence band maximum VBM. Conversely, a material is considered stable vs electron reduction if its reduction potential φ^{re} is higher than that of the reduction potential of water H^+/H_2.

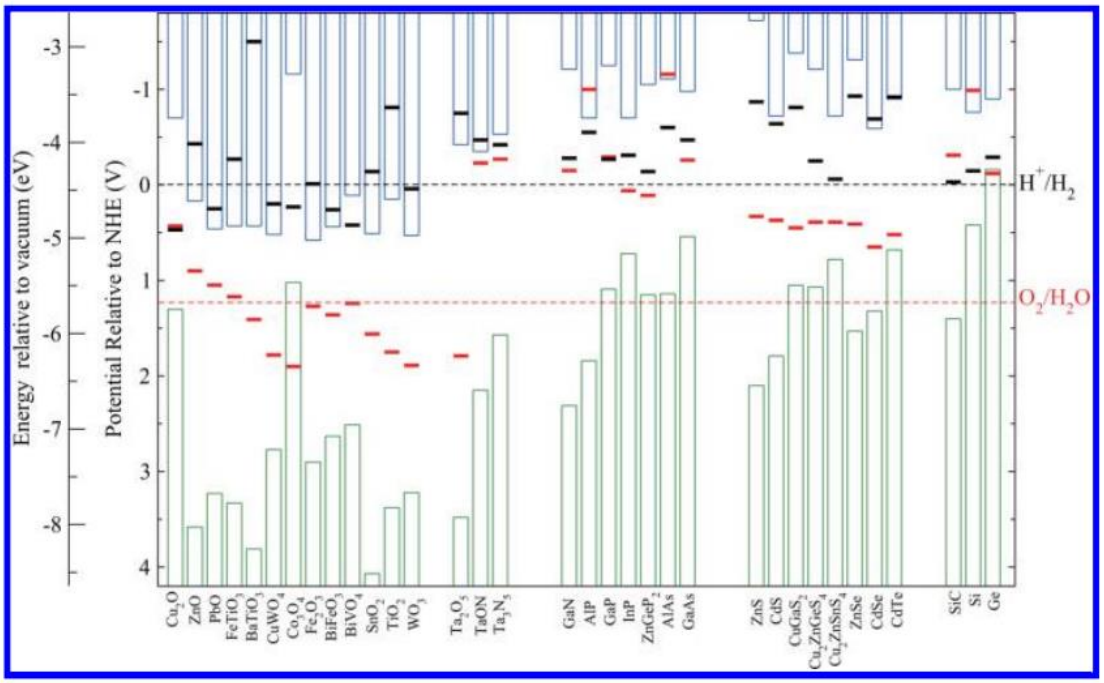

Figure 1.9: Calculated oxidation potentials (red bars) and reduction potentials (black bars) for a number of semiconductors commonly used in photoelectrochemical cells relative to the vacuum and NHE levels at pH0. Water oxidation and reduction potentials are also signified with horizontal dashed lines at 1.23V and 0V relative to the NHE respectively. The calculated valence (green column) and conduction (blue column) band edges are also plotted[96]

In the case of Si, it can be seen that the VBM and φ^{ox} are not both lower than the water oxidation potential and so it would not be a stable photoanode against oxidation. It is also worth noting that its reduction potential is more positive than its oxidation potential meaning that it will undergo corrosion even when experiments are carried out in the dark. This is one of the main reason Si photoanodes tend to require a more stable protection layer to increase stability. Some of these materials such as ZnO can look an unsuitable candidate for water oxidation but ultimately it is down to the reaction kinetics at the interface. The introduction of a suitable catalyst can ensure that the oxidation of water is the favoured reaction mechanism [26].

1.6 Charge Transport

Charge transport in a material is dictated by the materials charge carrier mobility which is a characteristic of the material itself. This mobility is often related to the morphology and crystallinity of the material. In general, charge is transported easier through a crystalline material as opposed to an amorphous one due to the defect locations within amorphous materials acting as an area where recombination can occur. Electrons and holes have different mobility's through a material owing to the fact that holes have a larger mass, and they are on a fixed path dictated by a conversely traveling electron [48]. Electrons have different mobility's depending on their location with regards to the atom they are orbiting. When an electron is liberated from the valence band it is transported to the valence band with a higher energy level. A semiconductors conductivity is given by the following equation:

$$\sigma = neu_e + peu_h \tag{1.40}$$

Where n is concentration of electrons in the conduction band, p is the concentration of holes in the valence band, e is the electron charge and u_e and u_h are the electron and hole mobility's respectively [45] [49].

The two main methods of charge transport within thin films are direct tunnelling and transport through defect sites. In order for tunnelling to occur, the film must be sufficiently thin (~5 nm) with the potential for tunnelling increasing as film thickness decrease.

Charge also gets transported through a material through site defects in the material, namely oxygen vacancies, interstitial defects or substitutional defects. Defects can act as a charge trap or a recombination centre. The difference between these two is that, in n-type semiconductor, a trap temporarily removes a charge carrier from the valence band depending on its energy level and releases it at a later time depending on the energy of the incoming photon as opposed to a recombination centre where the charge carrier is removed permanently without any useful photoconversion. Some oxygen vacancies can have energy levels which lie within the bandgap which can then be used as a sort of intermediate platform to hop between the valence and conduction band but this transport method is relatively slow. In the case of TiO_2, as will be

discussed in chapter 5, these oxygen vacancies have a detrimental effect on the charge transport through the photoanode and result in a more resistive TiO_2 film. Defect sites act as a better transport system for charge within a thin film. The use of organic precursors for thin film deposition increases the possibility of interstitial atom deposition such as N and C which can have a positive effect on transport due to the fact that atoms from these defect sites can have a smaller bandgap that TiO_2 and in turn act as intermediate energy levels within the TiO_2 bandgap.

1.7 Material Selection

Early photo electrochemical cells relied on applied external bias or a pH gradient in order to maintain water decomposition and even then, finding anode and cathode materials with sufficient negative and positive critical photo potentials respectively, was a major obstacle. Advancements were made on the work of Fukishima and Honda's TiO_2 and Platinum electrode system with the use of n-$SrTiO_3$, n-CdS, n-GaAs photoanodes and p-CdTe, p-GaP photocathodes among others [50] [51] [52] [53]but these lacked suitable redox couple and due to the decomposition of the semiconductor material itself under irradiation. The band bending in semiconductor-liquid PEC's is the only thing that determines the charge separation which is extremely sensitive to the material properties thus overtime as oxidation of the semiconductor takes place the photocurrent will diminish [54]

In recent years, the metal(oxide)-insulator-semiconductor model has become prevalent, using doped Si as the semiconductor. Crystalline-Si is an indirect bandgap material susceptible to oxidization, hence the metal-oxide should offer protection from oxidation but also encourage the flow of charge between the semiconductor and electrolyte. Degeneratively doped Si (n+,p+,p++) has been used in the water splitting process, providing sufficient mobility in order to counteract the non-radiative recombination in the Silicon of the majority carriers, seen in figure 1.10(a) and (b) below. High photovoltages have been achieved with these devices with a protective layer and catalyst [55] [56] [57]. However, the absence of the previously mentioned inbuilt p-n junction would see the recombination of minority carriers making it unsustainable for a continuous water splitting process. Implanting a p type region in an n-type semiconductor insulator interface figure

1.10(c) presents an advantage over degenerative Si in that it ensures a high hole density, which is independent of illumination, due to the diffusion of electrons to the p-type region and holes to the n-type region [58].

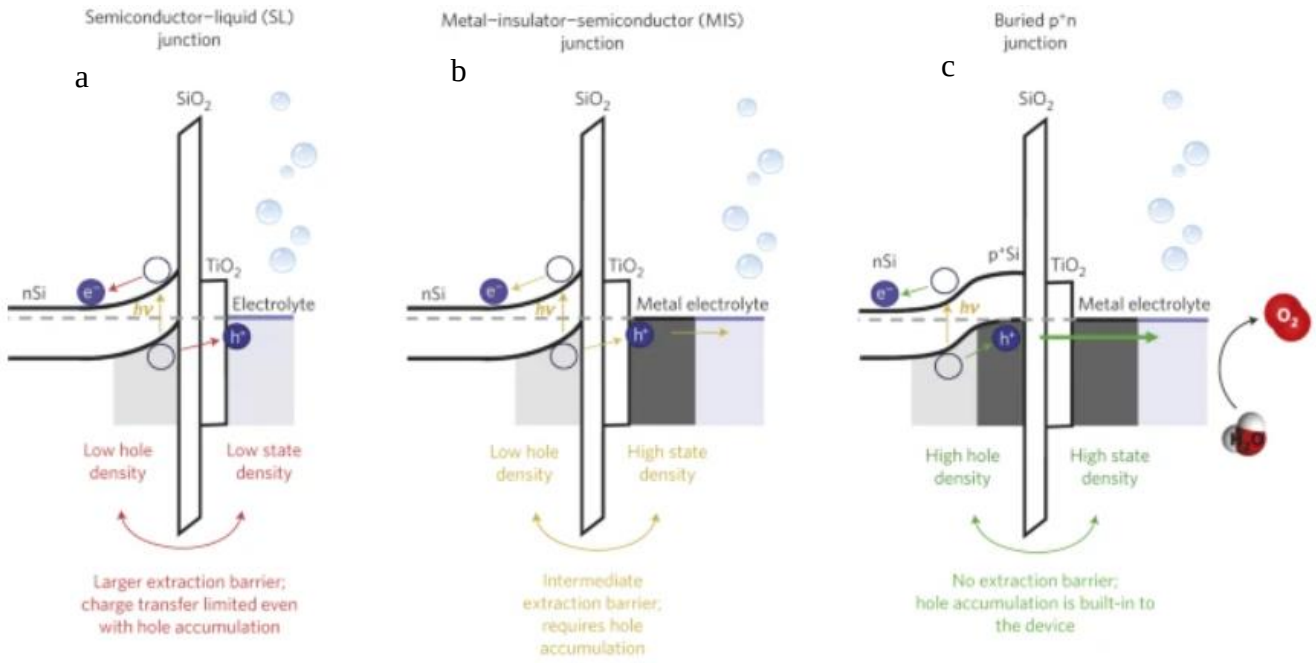

Figure 1.10: Schematic of different types of n type semiconductor in contact with a redox electrolyte each protected with a TiO2 protective layer. (a) Regular semiconductor/liquid interface. A low density of holes is present at the interface due to the absence of a metal catalyst. (b) A metal-insulator-semiconductor device which increases density of states at the interface due to the catalyst present at the surface but is limited by the thickness of protective/catalyst layers blocking illumination. (c) buried p+n junction device where the p+ region ensures a high density of holes at the interface regardless of illumination thus greatly reducing the extraction barrier [58].

This brings about the presence of a depletion region which shows itself in the form of band bending which is shown in figure 1.2. The addition of protective and conductive layers to the Si allows for bandgap tuneability as well as improved stability and photo activity. The selection of materials depends on whether the photo anode or photocathode will be the working electrode due to the need of different charge carrier concentrations at either electrode surface. An effective layer should be stable within the high or low pH water/brine splitting environment, electrically conductive, optically transparent and for mass production purposes, relatively cheap and earth abundant.

Ideally these protective layers should hold shielding and catalytic properties, but a trade-off always exists between these two properties which is why there has been an abundance of studies into electrode capping layers.

Metals have been used as protective layers without reducing the charge transfer due to their intrinsic conductive properties. Introducing a metal with a higher work function than Si like Ni (~5.1eV) can set the Schottky junction between the semiconductor and metal improving charge separation and carrier transport [59] [60] Used in conjunction with a basic 1M KOH electrolyte, Ni showed promising results as a electro catalyst as well as a protection layer with high PEC activity with relatively low activation potentials ~1.07 vs RHE, good durability as well as high photocurrent production [28]. The use of metallic Ti has also been studied for a photocathode and anode protective layer [61] however, metals such as Ni and Ti on their own are not transparent and while the thickness is in the nm-µm range they will absorb the light preventing it from reaching the underlying Si. Metal oxides provide a more suitable anodic protective layer because of their much higher work-functions than metals; owing to the oxygen vacancies and cation oxidation states [62]. These oxides, namely of the platinum group elements (Ru, Ir) along with Co Ni and Ti serve as excellent water oxidation catalysts. Mixtures of Cobalt and Nickel oxides such as $NiCo_2O_4$ and $CoNi_2O_4$ have been used in alkali media but have shown weaker activity towards OER than RuO_2. However, RuO_2 lacks long-term stability in alkali and acidic media because of possible oxidation to the soluble Ru(VI), Ru(VII), or volatile Ru(VIII) compounds [63]. *Mei et al* employed a Ir/IrO_x Catalytic layer on p+n-Si obtaining as much as 18 hour of stable water oxidation in 1mol/L H_2SO_4 producing a current density of $10mA/cm^2$ without an additional protective layer [64].

Zhang et al. used a TiO_2 thin film as the only protective/catalytic layer in a dye sensitized solar cell (DSSC) with varying results [65]. Using atomic layer deposition, a thin film of TiO_2 was deposited and covered with a molecular Ruthenium dye to enhance solar absorption. While efficiency was enhanced ~28%, the porous nature of the TiO_2 layer left the anode partially uncovered leading to the oxidation of the underlying semiconductor. Studies would suggest that TiO_2 protective layers do not have the conductive properties to function as a photoanode coating alone. One of these being the stoichiometry and phase of the TiO_2. Any deviation from stoichiometric TiO_2 has a detrimental effect on the flat band voltage and so the threshold potential

of the photoanode while also increasing the bandgap [66]. *Mei and Pederson et al* , showed that the protective TiO_2 layer in fact acts as an ohmic contact relying on electron transfer rather than hole transfer through the conduction band. Previously mentioned degenerately doped Si can be used to enhance charge transfer through the TiO_2 protective layer [67]. Incorporating a protective and catalytic layer on the same photoanode has been the main approach of recent works. Band engineering has become a critical process in achieving efficient PEC's in more recent times. This is achieved by controlling the composition of the oxide alloy or layering different oxide materials in order to change the bulk materials bandgap. The electrical performance of a photoanode with and without a catalyst layer has been studied previously [68]. *Steinmiller et al* used ZnO and a cobalt based layer as a protective and catalytic layer respectively. Their results showed that the photocurrent produced at constant bias' of 0.0V and +0.2V were roughly 2 times greater when using Co-based photocatalysts as opposed to just using a ZnO protection layer [68].

A Co-based catalytic coating also resulted in a negative onset voltage shift of ~0.23V. Previous work concluded that the flatband voltage of both photoanodes under test were similar, so this negative onset potential shift was attributed to the Co-based catalyst decreasing the unwanted electron-hole recombination near the flatband voltage [68]. Thus, a thin OER/CER catalyst at the electrode/electrolyte interface exhibits the ability to use the photogenerated holes in the underlying protection layer to enhance the generated photocurrent and in turn, the O_2/Cl_2 evolution. In general, the protection layer oxide thickness plays a critical role in determining carrier mobility. Band tunability was achieved by Kennay et al. by varying the protection/catalyst layer thickness respectively [69]. Metallic Ni was deposited at a range of thickness between 2 nm-20 nm with a NiOx catalytic capping layer . The OER onset potential was positively increased by almost 300 mV with an increase in Ni film thickness from 2-5 nm. The 2 nm Ni protective layer is ultra-thin and did not show properties similar to that of bulk Nickel. The greater inbuilt potential can therefore be attributed to an increased work function due to the interface being a mixture of Ni/NiOx and the electrolyte as opposed to just bulk Ni and the electrolyte. Several methods have been employed to improve the reaction kinetics on the anode surface including nanotubes, nanoparticles and nanowires. These possess properties to enhance PEC efficiency such as a high surface to volume ratio resulting in low recombination rate, minimises trapping events and enhancing light scattering events [70]. Comparisons between their efficiencies and optical and electrical characteristics can be seen in this work [71].

To improve the interfacial reaction kinetics, noble materials have been required to drive the OER/CER reaction and serve as an anticorrosive layer. Currently, the most widely used catalysts for industrial OER and CER are Ruthenium and Iridium due to their high catalytic activity and stability under both acidic and alkaline conditions. These materials are far superior with regards stability than transition metal oxides and so only a thin film ~3 nm can be enough to create a DSA. RuO_2 has been mainly used with inexpensive transition metal oxides such as TiO_2 because the ohmic nature of TiO_2 will promote excellent charge transfer at the oxide catalyst interface. Transition metal oxides can also be alloyed with synergistic conduction and photoactive abilities [72]. *Uddin et al*. calculated the difference in bandgap between TiO_2 and RuO_2 is ~ 2.4eV which

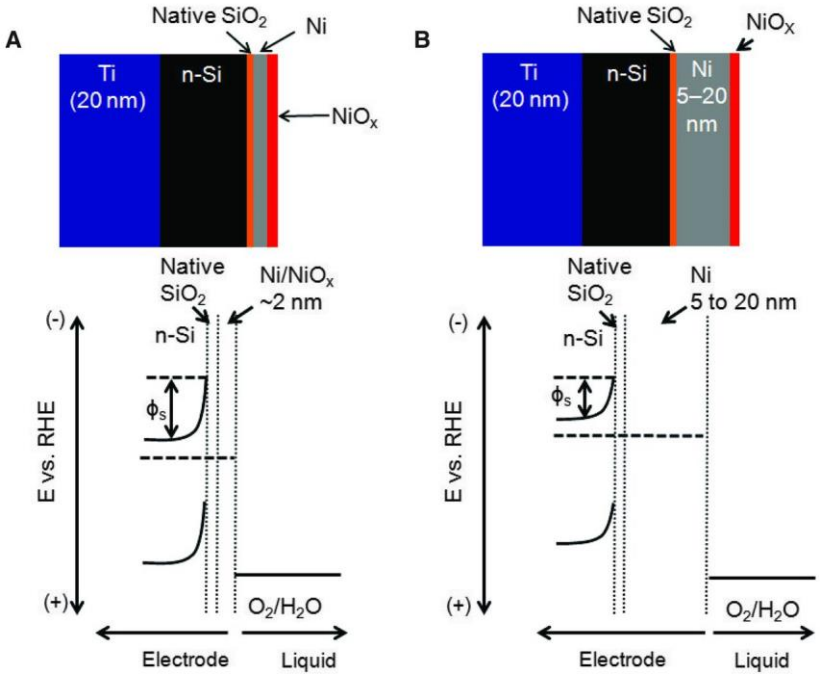

1: Schematic of an Ni/n-Si photoanode (A) utilizing an ultra-thin Ni/NiOx catalyst layer which results in a high built in potential φ_s and produced photocurrent as can be seen by the high degree of band bending in the band diagram and (B) The same device with a thicker Ni/NiOx layer which results in a lower built in potential φ_s and photovoltage due to the higher extraction barrier present.

leads to an overall band bending of ~1.22eV due to the alignment of the fermi levels. A decreasing bandgap, allowing for more of the visible range to be absorbed, was seen with increasing the %wt

of RuO_2 within the layer, from 3.23eV for pure TiO_2 to 3.19eV, 2.98eV, and 2.85eV for 1, 2.5 and 5 wt % of RuO_2 in TiO_2 respectively, [73]. A later study built on this by increasing the RuO_2 to 13-46 % wt RuO_2 in TiO_2 with excellent photo voltage results ~570 mV for films >16% wt. The conductivity of the produced film also did not change with a thicknesses range of 3-45 nm. A 2 nm TiO_2 capping layer was also used to great effect as a protection layer without having detrimental effect on half peak to peak splitting due to the charge carrier's ability to tunnel. Increased photovoltages from 500 mV – 53 3mV were also recorded when using a NiOx catalyst layer, however, photovoltages above 500 mV were obtained regardless of presence of a 2 nm protection layer, presence of catalyst, alloy layer film thickness or % composition [74]. P+n substrates were also used for this work to increase hole concentration at the interface. Ni, Fe and Co based earth abundant metal oxides catalyst and protective layers have been produced with a better OER activity compared to that of even RuO_2 and IrO_2. The reduced stability however, and the need for alkaline based electrolyte requires the protective layers to be much thicker than that of Pt group oxides. This will reduce absorbance of the incident light while also decreasing the exchange current density due to longer diffusion paths. [75]

When utilizing just one working electrode, i.e., a photoanode for OER, a stable metal such as Pt or even Al is used as a cathode. More recent studies have utilised a tandem cell system where a photoanode and cathode are used together. This system is used increasingly by researchers to achieve and sustain unassisted water/brine splitting. The presence of two photoelectrodes allows for semiconductor materials with a reduced bandgap to be utilised due to the fact that each photoelectrode only needs to provide enough potential for a half reaction. This reduction in bandgap allows for more of the solar spectrum to be absorbed resulting in a more efficient system [76].

Early p-type materials used for photocathodes include InP(bandgap=1.42eV) and $GaInP_2$ (bandgap=1.83eV) because previously used metal oxides like $KTaO_3$ and ZrO_2 showed low energy harvesting abilities due to their large (>3eV) bandgap [77]. These III-V materials were susceptible to corrosion in the dark (corrosion due to contact with the electrolyte solution, without net charge transfer through the electrode) The state of the art in recent years for Si based photocathodes is n+p Si substrates which work in a similar way but opposite to the previously mentioned p+n substrates by ensuring a high density of electrons at the semiconductor/protective/ catalytic layer

[58]. Metallic protective layers are, as is the case for photoanodes, one of the main candidates for photocathodic protection owing to their conductive properties along with the relatively simple fabrication process compared to that of metal oxides. Studies have shown that the introduction of a metallic Ti layer into MoSx/InP had improved PEC onset potential as well as providing and improved stability [78] [79]. This increased performance comes at a price however due to metals absorbing the incident light before it reaches the underlying Si (Not a transparent protective layer). Earth abundant metal oxide protective layers are the obvious candidate for protection layers for PC's because of availability and cost-effectiveness. As is the case with photoanodes, TiO_2 is one of the most widely used PC protection layer owing to its excellent optical transparency and exceptional carrier mobility [80]. The crystal structure of TiO_2 has a significant effect on fill factor, charge mobility and conductivity with more crystalline TiO_2 having superior electrical properties. *Ros Et al.* showed that a higher deposition temperature encourages more stable TiO_2 phases as well as a thin seed metallic Ti layer helped promote nucleation and crystallisation. A 10 fold increase in current density along with a ~3 fold increase in FF was obtained by increasing the deposition temp from 100°C-300°C [81]. No visible dissolution was recorded after a 300 hour stability test of crystalline TiO_2 in 0.5M H_2SO_4 as opposed to amorphous TiO_2 which seems to dissolve in acidic and basic media, a 10% current reduction over this time was attributed only to poorly attached Pt catalyst on the TiO_2 surface [82]. Additional layers have been used in unison with TiO_2 to obtain synergistic effects such as a carbon layer at the oxide-semiconductor interface or using TiO_2 to modify the surface of $CuInS_2$ which suggests TiO_2 requires the help of more conductive and or photoactive material to be used to act as a HER catalyst [83] [84] [85]. Materials do not have to possess optimal protective and conduction properties in order to be considered for a cathode overlayer as alloying or creating a "stack" can utilise each materials desired properties, i.e. TiO_2 & SnO_2 (protective & conductive layers respectively), although a surface catalyst is usually required to sustain HER [86]. Other transparent metal oxides such as Al_2O_3 has also been used as a passivation layer for photocathodes to enhance the HER performance as well as protect the underlying Si electrode [87]. A similar trade-off between conductivity and corrosion resistance exists however, when dealing with Al_2O_3 as with TiO_2. The greatest overpotential reduction occurred for *Park et al.* using a 1.4 nm thick Al_2O_3 layer on an Si electrode; the low thicknesses promoting tunnelling. Thicker layers cannot rely on tunnelling for charge transfer to the detriment of the overall conductivity. The greatest reduction in overpotential was 150 mV at 20 mA/cm^2

with no reduction in current density being observed over a 20 hour stability test. The optimal thickness of Al_2O_3 protective layers, when considering short term performance characteristics falls in the 1~4 nm range, exhibiting the desired overpotential reductions and conductivities however, long-term stability is not met and a catalytic overlayer such as NiOx or Pt is required [88]. Efforts were made to combat this using surface modification including using nanoporus Si [89] and even creating nano-pyramid structures on the Si surface by anisotropic alkali etching [90], with the later achieving 100 hour stability with only minor fluctuations in current density; attributed to the release of H_2 from the surface of the electrode. Stability, conductivity, charge transport tends to rely on more than just a materials electrical and anti-oxidation properties but also simply on the geometry and the density of available surface sites (surface area) of the electrode. For example. this can be seen with the transition metal dichalcogenide (TMD) MoS_2 , where edge sites provided the HER activity while the planer terrace sites are inert to HER providing a protection layer [91]. By engineering these planer layers to expose as much edge sites as possible, as well as ensuring full coverage of the Si, long term stability ~ 100 hour is achievable [92]. Benck et al. produced thin MoS_2 films with an underlying metallic Mo layer as well as films using a $[Mo_3S_{13}]^{2-}$ catalytic layer which produced results compared similarly to that of Pt. The use of Si with GaN has provided the best stability at high current density to date in 2018 where Vanka et al. achieved ~100 hour of stable photocurrent density at ~35 mA/cm^2. III-nitride materials possess strong ionic bonds which leads to surface states congregating at the band edges as opposed to the forbidden bandgaps which hinders recombination of charge leading to the long-term stability at such high current densities [93].

In general, previously discussed protection layers for photoelectrodes have performed well in the absence of the leading photocatalysts such as Pt, Ru, Ir, Rh etc. but in most cases lack either the long term stability or the photo activity of noble metals. Keeping these noble catalysts and scaling down of the % of NM content and incorporating earth abundant materials seems a promising area of research into highly efficient, highly stable photoelectrodes.

Bibliography

[1] P. Edwards, V. Kuznetsov, W. David and N. Brandon, "Hydrogen and fuel cells: Towards a sustainable energy future," *Energy Policy*, vol. 32, no. 12, pp. 4356-4362, 2008.

[2] K. Lie, V. Subramani and C. Song, Hydrogen and Syngas Production and Purification Technologies, Wiley, Pennsylvania, 2009.

[3] R. Chaubey, S. Sahu and O. James, "A review on development of industrial processes and emerging techniques for production of hydrogen from renewable and sustainable sources," *Renewable and Sustainable Energy Reviews,* vol. 23, pp. 443-463, 2013.

[4] R. Williams, "Becquerel photovoltaic effect in binary compounds," *The Journal of Chemical Physics,* vol. 32, no. 5, pp. 1505-1514, 1960.

[5] L. Vayssieres, On Solar Hydrogen and Nanotechnology, Wiley, Tsukuba, 2009.

[6] Q. Chen, G. Fan, H. Fu, Z. Li and Z. Zou, "Tandem photoelectrochemical cells for solar water splitting," *Advances in Physics,* vol. 3, no. 1, pp. 863-884, 2018.

[7] D. Su, S. Dou and G. Wang, "Anatase TiO2: Better Anode Material Than Amorphous and Rutile Phases of TiO2 for Na-Ion Batteries," *Chemistry of Materials,* vol. 27, no. 7, pp. 622-629, 2015.

[8] C. Grimes, O. Varghese and S. Ranjan, Light, Water, Hydrogen: The Solar Generation of Hydrogen by Water Photoelectrolysis, Springer, New York, 2008.

[9] K. Rajeshwar, "Fundamentals of Semiconductor Electrochemistry and Photoelectrochemistry," *Encyclopedia of Electrochemistry,* Wiley, Arlington, 2007.

[10] R. Williams, "Becquerel Photovoltaic Effect in Binary Compounds," *The Journal of Chemical Physics,* vol. 32, no. 5, pp. 1505-1514, 1960.

[11] A. Heller and B. Miller, "Some Recent Progress in Semiconductor-Liquid Junction Solar Cells," *Electrochemica Acta,* vol. 25, pp. 29-41, 1980.

[12] H. Gerischer, "Electrochemical Photo and Solar Cells Principles and some Experiments," *Electroanalytical Chemistry and Interfacial Electrochemistry,* vol. 58, pp. 263-274, 1975.

[13] S. Tembhurne, F. Nandjou and S. Haussener, "A thermally synergistic photo-electrochemical hydrogen generator operating under concentrated solar irradiation," *Nature Energy,* vol. 4, pp. 399-407, 2019.

[14] J. Nelson, The Physics of Solar Cells, Imperial College Press, London, 2003.

[15] L. D. P. Lewis M. Fraas, Solar Cells and Their Applications 2nd edition, Wiley, New, Jersey, 2010.

[16] A. Hussein, "A simple approach to extract the unknown parameters of PV modules," *Turkish Journal of Electrical Engineering & Computer Sciences,* vol. 25, pp. 4431-4444, 2017.

[17] M. G. Walter, E. L. Warren, J. R. McKone, S. Boettcher, Q. Mi and E. Santori, "Solar Water Splitting Cells," *Chemical Reviews,* vol. 110, no. 11, pp. 6446-6473, 2010.

[18] Z. Chen, T. Deutsch, H. Dihn, K. Domen and K. Emery, Photoelectrochemical Water Splitting, Springer, New York, 2013.

[19] A. Polman and H. Atwater, "Photonic design principles for ultrahigh-efficiency photovoltaics," *Nature Materials,* vol. 11, pp. 174-177, 2012.

[20] A. Gedamu, J. Rick, A. Aregahegn and B. Hwang, "Using hematite for photoelectrochemical water splitting: a review of current progress and challenges," *Royal Society of Chemistry,* vol. 1, pp. 243-267, 2016.

[21] R. Tang-Kong, C. O'Rourke and A. Mills, "Silicon Photoanodes for Solar-Driven Oxidation of Brine: A Nanoscale, Photo-Active Analog of the Dimensionally-Stable Anode," *Journal of The Electrochemical Society,* vol. 165, no. 16, pp. 1072-1079, 2018.

[22] L. McCafferty, C. O'Rourke, A. Mills, A. Kafizas and I. Parkina, "Light-driven generation of chlorine and hydrogen from brine using highly selective Ru/Ti oxide redox catalysists," *The Royal Society of Chemistry, Sustainable Energy Fuels,* vol. 1, no. 2, pp. 254-257, 2017.

[23] J. Yang, D. Wang, H. Han and C. Li, "Roles of Cocatalysts in Photocatalysis and Photoelectrocatalysis," *Accounts of Chemical Research,* vol. 46, no. 8, pp. 1900-1909, 2012.

[24] H. Ooka, J. Huang and K. Exner, “The Sabatier Principle in Electrocatalysis: Basics, Limitations, and Extensions,” *Electrochemical Energy Conversion and Storage,* vol. 9: 654460, 2021.

[25] J. Malik, A. Mandani and B. Pieber, “Evidence for Photocatalyst Involvement in Oxidative Additions of Nickel-Catalyzed Carboxylate O-Arylations,” *J. Am. Chem. Soc.,* vol. 142, no. 25, pp. 11042-11049, 2020.

[26] B. Hunter, H. Gray and A. Muller, “Earth-Abundant Heterogeneous Water Oxidation Catalysts,” *Chemical Reviews,* vol. 116, no. 22, pp. 14120-14136, 2016.

[27] M. Lyons, R. Doyle, I. Godwin, M. O'Brien and L. Russell, “Hydrous Nickel Oxide: Redox Switching and the Oxygen Evolution Reaction in Aqueous Alkaline Solution,” *Journal of the Electrochemical Society,* vol. 159, no. 12, pp. 932-944, 2012.

[28] M. Kenney, “High-Performance Silicon Photoanodes Passivated with Ultrathin Nickel Films for Water Oxidation,” *Science,* vol. 342, pp. 836-840, 2013.

[29] Q. Lei, B. Wang, P. Wang and S. Liu, “Hydrogen generation with acid/alkaline amphoteric water electrolysis,” *Energy Chemistry,* Vols. 162-169, 2019.

[30] S. ayabal, S. Govindarajan, W. Jian, Y. Liu and D. Geng, “Understanding High-Electrocatalytic Performance of Two-Dimensional MoS2 Nanosheets and Their Composite Materials,” *Journal of Materials Chemistry,* vol. 5, no. 47, 2017.

[31] B. E. Conway and M. Salamon, “ELECTROCHEMICAL REACTION ORDERS :APPLICATIONS TO THE HYDROGEN- AND OXYGEN-EVOLUTION REACTIONS,” *Electrochimica Acta,,* vol. 9, no. 12, pp. 1599-1615, 1964.

[32] S. Bajracharya, A. Elmekawy, S. Srikanth and D. Pant, Microbial Electrochemical and Fuel Cells. Fundementals and Applications, Egypt, Elsevier Ltd, 2016.

[33] Z. Yin, R. Fan, G. Huang and M. Shen, “11.5% efficiency of TiO2 protected and Pt catalyzed n+photocathodes for photoelectrochemical water splitting:manipulating the Pt distribution and Pt/Si contact,” *Chemical Communiacations,* vol. 54, no. 5, pp. 543-546, 2018.

[34] G. Huang, J. Mao, R. Fan, Z. Yin, X. Wu and J. Jie, “Integrated MoSe2 with n1p-Si photocathodes for solar water splitting with high efficiencies and stability,” *Applied Phys Letters,* vol. 112, 2017.

[35] R. Fan, J. Mao, Z. Yin, J. Jie, W. Dong, L. Fang and F. Zheng, “Efficient and Stable Silicon Photocathodes Coated with a Vertically Standing Nano-MoS2 Films for Solar Hydrogen Production,” *Applied Materials and Interfaces,* vol. 9, no. 7, pp. 6123-6129, 2017.

[36] E. L. Warren, J. McKone, H. Atwater, H. Graya and N. Lewis, “Hydrogen-evolution characteristics of Ni–Mo-coated, radial junction, n+p-silicon microwire array photocathodes,” *Energy and Enviromental Science,* vol. 5, no. 11, pp. 9653-9661, 2012.

[37] J. Vos, Z. Liu, F. Speck, N. Perini, W. Fu and S. Cherevko, “Selectivity Trends Between Oxygen Evolution and Chlorine Evolution on Iridium-Based Double Perovskites in Acidic Media,” *ACS Catalysis,* vol. 9, pp. 8561-8574, 2019.

[38] F. E. Osterloh, “Inorganic nanostructures for photoelectrochemical and photocatalytic water splitting,” *Chem Soc. Review,* vol. 42, pp. 2294-2320, 2013.

[39] B. Tilak, “Kinetics of Chlorine Evolution—A Comparative Study,” *Journal of The Electrochemical Society,* vol. 126, no. 8, pp. 1343-1348, 1979.

[40] H. A. Hansen, I. Man, F. Studt, F. Abild-Pedersen and T. Bligaard, “Electrochemical chlorine evolution at rutile oxide (110) surfaces,” *Phys. Chem. Chem. Phys,* vol. 12, pp. 283-290, 2010.

[41] I. Sohrabnejad-Eskan, A. Goryachev, K. S. Exner, L. A. Kibler, E. Hensen and J. P. Hofmann, “Temperature-Dependent Kinetic Studies of the Chlorine Evolution Reaction over RuO2,” *ACS Catalysis,* vol. 7, no. 4, pp. 2403-2411, 2017.

[42] D. Rosestolato, J. Frengoni, S. Ferro and A. De Battisti, “Influence of the Nature of the Electrode Material and Process Variables on the Kinetics of the Chlorine Evolution Reaction. The Case of IrO2-Based Electrocatalysts,” *Electrochimica Acta,* vol. 139, pp. 180-189, 2014.

[43] L. J. Janssen, L. M. Starmans, J. Vrssmt and E. Barendrecht, “MECHANISM OF THE CHLORINE EVOLUTION ON A RUTHENIUM OXIDE/TITANIUM OXIDE ELECTRODE AND ON A RUTHENIUM ELECTRODE,” *Electrochemica Acta,* vol. 22, pp. 1093-1100, 1976.

[44] K. Exner, J. Anton, T. Jacob and H. Over, “Controlling Selectivity in the Chlorine Evolution Reaction over RuO2-Based Catalysts,” *Agnewandte Chemie,* vol. 126, pp. 11212-11215, 2014.

[45] L. Vayssieres, On Solar Hydrogen & Technology, Wiley, Japan, 2009.

[46] Y. Li, L. Zhoua and S. Guo, “Noble metal-free electrocatalytic materials for water splitting in alkaline electrolyte,” *EnergyChem,* vol. 3:100053, 2021.

[47] T. Bak, J. Nowotny, M. Rekas and C. Sorrell, “Photo-electrochemical hydrogen generation from water using solar energy. Materials-related aspects,” *Hydrogen Energy,* vol. 27, no. 10, pp. 991-1022, 2002.

[48] unacademy, “unacademy- mobility in semiconductors,” [Online]. Available: https://unacademy.com/content/upsc/study-material/physics/mobility-of-electrons-and-holes/#:~:text=The%20Mobility%20of%20electron%20particles%20is%20higher%20than%20that%20of,gap%20created%20by%20missing%20electrons.. [Accessed September 2022].

[49] R. Van de Kron and M. Graetzel, Photoelectrochemical Hydrogen Production, Springer, New York, 2012.

[50] K. Ohashi, J. McCann and J. Bockris, “Stable photoelectrochemical cells for the splitting of water,” *Nature,* vol. 266, pp. 610-612, 1977.

[51] A. J. Bard, “Photoelectrochemistry,” *Science,* vol. 207, no. 4427, pp. 139-144, 1980.

[52] R. Memming, “SOLAR ENERGY CONVERSION BY PHOTOELECTROCHEMICAL PROCESSES,” *Electrochemica Acta,* vol. 25, no. 1, pp. 77-88, 1980.

[53] A. J. Nozik, “Photoelectrochemical Cells,” *Philosophical Transactions of the Royal Society of London,* vol. 295, pp. 453-470, 1980.

[54] N. Guijarro, M. Prévot and K. Sivula, “Surface modification of semiconductor photoelectrodes,” *Physical Chemistry Chemical Physics,* vol. 7, no. 24, pp. 15655-15674, 2015.

[55] Y. W. Chen, J. Prange, S. Duhnen, Y. Park, M. Gunji, C. Chidsey and P. McIntyre, “Atomic layer-deposited tunnel oxide stabilizes silicon photoanodes for water oxidation,” *Nature Materials,* vol. 10, no. 7, pp. 539-544, 2011.

[56] A. G. Scheuermann, J. D. Prange, M. Gunji, C. Chidsey and P. McIntyre, “Effects of catalyst material and atomic layer deposited TiO2 oxide thickness on the water oxidation performance of metal–insulator–silicon anodes,” *Nature Materials,* vol. 6, no. 8, pp. 2487-2496, 2013.

[57] Z. Yu, P. Yang, S. Chen, M. Zhang and G. Shi, "NiFe Alloy Protected Silicon Photoanode for Efficient Water Splitting," *Advanced Enegy Materials,* vol. 7, no. 6, 2016.

[58] A. G. Scheuermann, J. Lawrence, K. Kemp, T. Ito, A. Walsh, C. Chidsey and P. McIntyre, "Design principles for maximizing photovoltage in metal-oxide-protected water-splitting photoanodes," *Nature Materials,* vol. 15, pp. 99-105, 2016.

[59] H. Wang, L. Zhang, Z. Chen, J. Hu and S. Li, "Semiconductor heterojunction photocatalysts: design, construction, and photocatalytic performances," *Chem Soc. Review,* vol. 43, no. 15, pp. 5234-5244, 2014.

[60] F. A. Laskowski, M. R. Nellist, R. Venkathkarthick and S. W. Boettcher, "Junction Behavior of n-Si Photoanodes Protected by Thin Ni Elucidated from Dual Working Electrode Photoelectrochemistry," *Energy and Enviromental Science,* vol. 10, no. 2, pp. 570-579, 2017.

[61] Q. Zhang, T. Li, J. Luo, B. Liu, J. Liang, N. Wang, Z. Kong and B. Li, "Ti/Co-S catalyst covered amorphous Si-based photocathodes with high photovoltage for the HER in non-acid environments," *Journal of Materials Chemistry,* vol. 6, pp. 811-816, 2018.

[62] M. T. Greiner, L. Chai, M. G. Helander, W.-M. Tang and Z.-H. Lu, "Transition Metal Oxide Work Functions: The Influence of Cation Oxidation State and Oxygen Vacancies," *Advanced Functional Materials,* vol. 22, no. 21, pp. 4557-4568, 2016.

[63] K. Juodkazis, J. Juodkazyte, R. Vilkauskaite, B. Sebeka and V. Jasulaitiene, "Oxygen evolution on composite ruthenium and nickel oxides electrode," *Chemija,* vol. 9, no. 1, pp. 1-6, 2008.

[64] B. Mei, B. Seger, T. Pedersen, M. Malizia, O. Hansen and I. Chorkendorf, "Protection of p+-n-Si Photoanodes by Sputter-Deposited Ir/IrOx Thin Films," *Journal of Physical Chemistry Letters,* vol. 5, no. 11, pp. 1945-1952, 2014.

[65] H. Yu, S. Zhang, H. Zhao, B. Xue, P. Liu and G. Will, "High-Performance TiO2 Photoanode with an Efficient Electron Transport Network for Dye-Sensitized Solar Cells," *J. Phys Chem,* vol. 113, pp. 16277-16282, 2009.

[66] M. Radecka, A. Trenczek-Zajac, K. Zakrzewska and M. Rekas, "Effect of oxygen nonstoichiometry on photo-electrochemical properties of TiO2−x," *Journal of Power Sources,* vol. 173, no. 2, pp. 816-820, 2007.

[67] B. Mei, T. Pedersen, P. Malacrida, D. Bae, R. Frydendal and O. Hansen, “Crystalline TiO2: A Generic and Effective Electron Conducting Protection Layer for Photo-anodes and -Cathodes,” *The Journal of Physical Chemistry,* vol. 119, no. 27, pp. 15019-15027, 2015.

[68] E. M. Steinmiller and K.-S. Choi, “Photochemical deposition of cobalt-based oxygen evolving catalyst on a semiconductor photoanode for solar oxygen production,” *Proceedings of the National Academy of Sciences,* vol. 106, no. 49, pp. 20633-20636, 2009.

[69] M. Kenney, M. Gong, Y. Li, J. Wu, J. Feng, M. Lanza and H. Dai, “High-Performance Silicon Photoanodes Passivated with Ultrathin Nickel Films for Water Oxidation,” *Science,* vol. 342, no. 6160, pp. 836-840, 2013.

[70] H. M. A. Javad, W. Que and Z. He, “Anatase TiO2 Nanotubes as Photoanode for Dye-Sensitized Solar Cells,” *Journal of Nanoscience and Nanotechnology,* vol. 14, no. 2, pp. 1085-1098, 2014.

[71] A. A. Tahir, M. A. Ehsan, M. Mazhar and K. U. Wijayantha, “Photoelectrochemical and Photoresponsive Properties of Bi2S3 Nanotube and Nanoparticle Thin Films,” *Chemistry of Materials,* vol. 22, no. 17, pp. 5084-5092, 2010.

[72] E. C. Elzbieta Kusmierek, “Application of TiO2–RuO2/Ti electrodes modified with WO3 in electro- and photoelectrochemical oxidation of Acid Orange 7 dye,” *Journal of Photochemistry and Photobiology A: Chemistry,* vol. 302, pp. 59-68, 2015.

[73] T. Uddin, Y. Nicolas, C. Olivier, T. Toupance and M. Muller, “Preparation of RuO2/TiO2 Mesoporous Heterostructures and Rationalization of Their Enhanced Photocatalytic Properties by Band Alignment Investigations,” *The Journal of Physical Chemistry,* vol. 117, no. 42, pp. 22098-22110, 2013.

[74] O. Hendricks, A. Scheuermann, M. Schmidt, P. Hurley, P. Mcintyre and C. Chidsey, “Isolating the photovoltaic junction: atomic layer deposited TiO2-RuO2 alloy Schottky contacts for silicon photoanodes,” *Applied Materials and Interfaces,* vol. 8, no. 36, p. 23763–23773, 2016.

[75] R. Fan, Z. Mi and M. Shen, “Silicon based photoelectrodes for photoelectrochemical water splitting,” *Optics Express,* vol. 27, no. 4, pp. 51-80, 2019.

[76] Z. Li, W. Luo, M. Zhang, J. Feng and Z. Zou, "Photoelectrochemical cells for solar hydrogen production: current state of promising photoelectrodes, methods to improve their properties, and outlook," *Royal Society of Chemistry,* vol. 6, pp. 347-370, 2012.

[77] J. A. T. Oscar Khaselev, "Electrochemical Stability of p-GaInP2 in Aqueous Electrolytes Toward Photoelectrochemical Water Splitting," *J. Electrochem. Soc,* vol. 145, no. 10, pp. 3335-3339, 1998.

[78] Q. Li, M. Zheng, M. Zhong, L. Ma, F. Wang, L. Ma and W. Shen, "Engineering MoSx/Ti/InP Hybrid Photocathode for Improved Solar Hydrogen Production Improved Solar Hydrogen Production," *Nature: Scientific Reports,* vol. 6(1):29738, 2016.

[79] R. Fan, G. Huang, Y. Wang, Z. Mi and M. Shen, "Efficient n+p-Si photocathodes for solar H2 production catalyzed by Co-W-S and stabilized by Ti buffer layer," *Applied Catalysis B: Environmental,* vol. 237, pp. 158-165, 2018.

[80] S. Murthy, P. Effiong and C. C. Fei, "Metal oxide nanoparticles in biomedical applications," in Y. Al-Douri, *Metal Oxide Powder Technologies,* pp. 233-251, 2020.

[81] C. R. Orcid, T. Orcid, M. D. Hernandez-Alonso and G. Penelas-Pérez, "Charge Transfer Characterization of ALD-Grown TiO2 Protective Layers in Silicon Photocathodes," *Applied materials and Interfaces,* vol. 9, no. 21, pp. 17932-17941, 2017.

[82] D. Bae, S. Shayestehaminzadeh, E. B. Thorsteinsson and T. Pedersen, "Protection of Si photocathode using TiO2 deposited by high power impulse magnetron sputtering for H2 evolution in alkaline media," *Solar Energy Materials and Solar Cells,* vol. 144, pp. 758-765, 2016.

[83] X. Sun, J. Jiang, Y. Yang, Y. Shan, L. Gong and M. Wang, "Enhancing the Performance of Si-Based Photocathodes for Solar Hydrogen Production in Alkaline Solution by Facilely Intercalating a Sandwich N-Doped Carbon Nanolayer to the Interface of Si and TiO2," *Applied Materials and Interfaces,* vol. 11, no. 21, pp. 19132-19140, 2019.

[84] J. Zhao, T. Minegishi, L. Zhang, M. Zhong and M. Nakabayashi, "Enhancement of Solar Hydrogen Evolution from Water by Surface Modification with CdS and TiO2 on Porous CuInS2 Photocathodes Prepared by an Electrodeposition–Sulfurization Method," *Angewendte Chemie,* vol. 53, no. 44, pp. 11808-11812, 2014.

[85] W. Vijselaar, R. M. Tiggelaar, H. Gardeniers and J. Huskens, “Efficient and Stable Silicon Microwire Photocathodes with a Nickel Silicide Interlayer for Operation in Strongly Alkaline Solutions,” *ACS Energy Letters,* vol. 3, no. 5, pp. 1086-1092, 2018.

[86] M. G. Kast, L. J. Enman, N. J. Gurnon, A. Nadarajah and S. Boettcher, “Solution-Deposited F:SnO2/TiO2 as a Base-Stable Protective Layer and Antireflective Coating for Microtextured Buried-Junction H2-evolving Si Photocathodes,” *Applied Materials and Interfaces,* vol. 6, no. 24, pp. 22830-22837, 2014.

[87] W.-c. Wang, C.-W. Lin, H.-J. Chen, C.-W. Chang, J.-J. Huang and M.-J. Yang, “Surface Passivation of Efficient Nanotextured Black Silicon Solar Cells Using Thermal Atomic Layer Deposition,” *Applied Materials and Interfaces,* vol. 5, no. 19, pp. 9752-9759, 2013.

[88] M.-J. Park, J.-Y. Jung, S.-M. Shin, J.-W. Song, Y.-H. Nam, D.-H. Kin and J.-H. Lee, “Photoelectrochemical oxygen evolution improved by a thin Al2O3 interlayer in a NiOx/n-Si photoanode,” *Thin Solid Films,* vol. 599, pp. 54-58, 2016.

[89] M. J. Choi, J.-Y. Jung, M.-J. Park, J.-W. Song, J.-H. Lee and J. H. Bang, “Long-term durable silicon photocathode protected by a thin Al2O3/SiOx layer for photoelectrochemical hydrogen evolution,” *Journal of Material Chemistry,* vol. 2, pp. 2928-2933, 2014.

[90] R. Fan, W. Dong, L. Fang, F. Zheng, X. Sua, S. Zou, J. Huang and X. Wang, “Stable and efficient multi-crystalline n+p silicon photocathode for H2 production with pyramid-like surface nanostructure and thin Al2O3 protective layer,” *Applied Physics Letters,* vol. 106:013902, 2015.

[91] K. P. J. J. B. J. H. N. S. H. I. C. Thomas F. Jaramillo, “Identification of Active Edge Sites for Electrochemical H2 Evolution from MoS2 Nanocatalysts,” *Science Reports,* vol. 317, pp. 100-102, 2007.

[92] J. Benck, S. C. Lee, K. L. Fong, J. Kibsgaard, R. Sinclair and T. F. Jaramillo, “Designing Active and Stable Silicon Photocathodes for Solar Hydrogen Production Using Molybdenum Sulfide Nanomaterials,” *Advanced Energy Materials,* vol. 4(18):1400739, 2014.

[93] S. Vanka, E. Arca, S. Cheng, K. Sun, G. Bottom, G. Teeter and Z. Mi, “High Efficiency Si Photocathode Protected by Multifunctional GaN Nanostructures,” *Nano Letters,* vol. 18, no. 10, pp. 6530-6537, 2018.

[94] Brilliant, “Brilliant,” [Online]. Available: https://brilliant.org/practice/spectral-properties-sunlight/. [Accessed 14 November 2021].

[95] mPowerUK, “Electropedia: Battery and Energy Technologies,” mPowerUK, 2005. [Online]. Available: https://www.mpoweruk.com/solar_power.htm. [Accessed 13 December 2021].

[96] S. Chen and L.-W. Wang, “Thermodynamic Oxidation and Reduction Potentials of Photocatalytic Semiconductors in Aqueous Solution,” *Chemistry of Materials,* vol. 24, pp. 3659-3666, 2012.

[97] “pn junction,” Physics stuff, 30 October 2017. [Online]. Available: http://physicstuff.com/p-n-junction/. [Accessed 2022 January` 3].

[98] J. Li and N. Wu, “Semiconductor-Based Photocatalysts and Photoelectrochemical Cells for Solar Fuel Generation: A Review,” *Catalysis Science & Technology,* vol. 5, pp. 1360-1384, 2015.

Chapter 2

2. Atomic Layer Deposition

2.1 ALD Overview

Atomic Layer Deposition (ALD) is an important technique which enables the miniaturisation of semiconductor devices. ALD is a thin film deposition technique which is a variant of the Chemical Vapour Deposition (CVD) process. Thin film deposition is carried out by repeating a series of self-limiting surface reactions by introducing a metal precursor and a co-reagent to the surface with an intermittent purge sequence. ALD was developed, independently by two different research team. The first form of ALD called "Molecular Layering" was created in the former Soviet Union by Stanislav Koltsov, Valentin Aleskovsky and colleagues and the second named "atomic layer epitaxy" by Tuomo Suntola in Finland [1]. Koltsov and colleagues published the first paper regarding Molecular Layering in 1967 depositing thin films of TiO_2 and GeO_2 on silicon at 180ºC [2],. further work on Molecular Layering with TiO_2 and SiO2 resulted in a number of papers over the following ten years [3] [4] [5] [6] [7]. Tuomo Suntola would make the same discovery as Koltsov and colleagues , roughly ten years later, whilst developing flat panel displays. Suntola and team realised conventional thin film techniques such as vacuum evaporation or sputtering didn't have precise enough control over the deposited film, zinc sulfide, as a consequence they developed "Atomic Layer Epitaxy" ; a patent for the ALE operating method was submitted and granted by 1985 followed shortly by a patent for the apparatus used [8] [9]. The method was adapted in the 1980's to deposit compound semiconductors, in particular III-V compound [10] and garnered a lot of interest despite no real commercial success. The Early 90's saw a rapidly increasing interest in ALD from the silicon-based microelectronics industry, where the requirement for thin metal oxide films were key to maintaining progress in line with Moore's' law. The highly controllable nature

of ALD ensured a high aspect ratio along with a low pin-hole density at the surface on the nanometre scale.

2.2 ALD Cycle

Thin films are grown by means of self-limiting half reactions on a substrate surface. This is carried out by a series of alternating precursor and reactant cycles, separated by an inert gas purge, which form the thin film in a stepwise uniform fashion. The cycle begins with a pulse of a gas phased precursor into the reactor chamber where the substrate is present. This causes a reaction between the precursor and the reactive surface sites on the sample surface. This is followed by a pulse of inert gas which evacuates the chamber of any physiosorbed species, by products and excess precursor to avoid undesired gas phase reactions with the reactant. A reactant pulse followed by another gas purge complete the cycle (Figure 2.1).

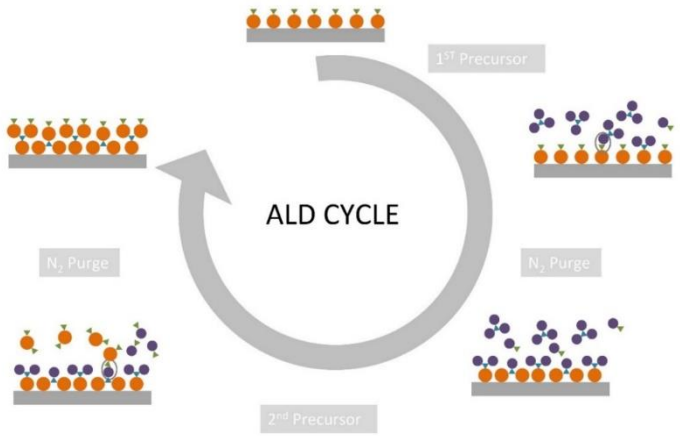

Figure 2.1 Schematic of the full ALD cycle including the surface reactions and precursor pulse [36]

uniformity under ideal conditions. The thickness of the deposited film can then be digitally controlled by varying the number of cycles. The stepwise introduction of the precursors as opposed to the CVD regime allows for ultra-precise thickness control.

2.3 Thermal ALD

The thermal ALD process is the most widely used form of ALD. This form of ALD uses only thermal energy to carry out the surface reactions which is provided by the reactor chamber itself. Once the sample is loaded it is important to allow the substrate to reach the reactor chamber temperature. For metal oxides H_2O is the preferred oxygen source for the thermal ALD process as it reacts with a wide variety of precursor types namely metalorganic and halogenated metal precursors. Similar to CVD, the ALD reaction depends on a binary process of A + B = Products although it employs a sequential ABAB reaction sequence. An example of this binary growth below is the deposition of TiO_2 and ZnO and their corresponding enthalpies: [11]

$$TiCl_4 + 2H_2O \longrightarrow TiO_2 + 4HCl \qquad (2.1)$$
$$\Delta H = -16kcal$$

$$Zn(CH_2CH_3)_2 + H_2O \longrightarrow ZnO + 2C_2H_6 \qquad (2.2)$$
$$\Delta H = -70kcal$$

These ALD processes have negative heats of reaction and occur spontaneously at various temperatures without the aid of a plasma and are referred to as thermal ALD processes. The most common of these systems are the deposition of binary metal oxides such as Al_2O_3, TiO_2, ZnO, ZrO_2, SnO_2 and HfO_2. Metal nitride thin films such as TiN and TaN are also common in ALD although NH_3 is the common reactant for such material. [11]

2.4 Plasma Enhanced ALD

The overall process sequence for PE-ALD is quite similar to thermal ALD processes. This process is characterized by 4 steps: precursor exposure, inert purge, reactant exposure, inert gas purge. Where PE-ALD differs from conventional ALD is the introduction of plasma during the reactant exposure step. The plasma acts by dissociating the gas to produce radicles, electrons and ions. This increased reactivity speeds up the deposition process and reduces the number of unreacted species. The PE-ALD system has several benefits over the thermal ALD process mainly by reducing the deposition temperature and widening the process window. O_2 plasmas are extremely effective reactants for removing organic ligands and perform better than its H_2O counterpart [12] [13].This is beneficial because the complete purge of water molecules and hydrogen ions can be difficult as well as a number of materials and substrates being water sensitive. Another feature of PE-ALD is its ability to modify the substrate surface by exposing it to plasma. The discharge ions and electrons produced by the induced plasma are physically sputtered or chemically react with the material surface altering its structure. However, higher controllability of the PE-ALD system allows for the enhancement of surface properties, lower deposition temperatures and phase selectivity. [14] [15]

2.5 Growth Per Cycle

The growth per cycle or GPC is defined as the thickness increase of a deposited layer after a single ALD cycle. This is of particular interest as it gives information about the nucleation behaviour This value can only be calculated post deposition as it depends on the deposited film thickness and the number of ALD cycles. GPC is dependent on a number of factors which include deposition temperature, precursor pulse/purge times and number of available active sites. [16]

$$Growth\ per\ Cycle = \frac{Film\ Thickness}{Number\ of\ cycles} \tag{2.3}$$

The film thickness here is usually in the nm or μm range and so when divided by the number of cycles the GPC is usually given in Å or nm. GPC is defined as the growth per cycle usually averaged over several hundred cycles however the growth rate of thin films can differ over the course of the ALD process. Effects such as steric hindrance caused by bulky precursor ligands can have a negative effect on the growth rate by blocking active surface sites which leads to the GPC being generally less than the thickness of a single monolayer [17]. For example, *Nazarov et al. performed a* comprehensive study of Tin precursors demonstrating that precursors with bulkier ligands such as Sn(tbba) have lower growth rates at similar temperatures to say TDMASn [18]. In general, a precursor with a smaller molecule size is desirable due to more coverage and hence quicker saturation of the substrate surface. Complete surface saturation may present itself initially as island type growth when analysing at a per cycle growth level. The nature of the ALD cycle and the reaction mechanism on the substrate surface allows for a complete coverage of a monolayer of oxide before another monolayer is deposited on top. This gives excellent control over thickness of a thin film providing the ALD cycle is optimized.

2.6 Self-Limiting regime

Precise control over the thickness of a deposited thin film is achieved due to the stepwise nature of the ALD process. As mentioned previously, the majority of ALD process involve a binary reaction arrangement which uses two precursors and two inert purge steps in between. A finite number of active surface sites are available on the substrate surface and so only a finite number of surface species can undergo reaction which leads to a smooth pin-hole free surface. Precursor flux will differ throughout the reaction chamber depending on the delivery system, but this does not have a detrimental effect on deposition process as the number of reactions depends on the number of available active sites [11]. Precursor molecules first chemisorbed to the surface while additional molecules may physisorb when no reactive sites are available . The role of the inert gas purge is to remove any gas phase precursor and to remove weakly bonded physiosorbed species from the surface. If these physiosorbed species are not removed, they can remain causing impurities and

non-conformal films. As a consequence, the length of a purge is significant in a growth process and has a direct effect on film quality. The number of monolayers that can be produced from one ALD pulse is given by:

$$\theta = \frac{(I_i - I_e)t_i}{\theta_i}$$

Where θ_i is the atomic density for a single monolayer of coverage, I_i is the number of atoms impinging per second on the substrate surface, I_e is the number of atoms per second reevaporated from the substrate surface during deposition and t_i is the pulse duration. Equation 2.4 shows that the monolayer coverage is defined by the number of atoms that remain on the substrate surface divided by the number of atoms that are needed in order to create one monolayer of coverage [19]. In an ideal system a monolayer of the first precursor remains while its physiosorbed species are reevaporated and similarly with the second precursor once it is chemisorbed then the physiosorbed species will reevaporate also. Chemisorption happens in the ALD regime in 3 different ways, Ligand exchange, association and dissociation.

2.7 Ligand Exchange

Ligand exchange is a form of chemical reaction where a ligand is replaced with another on the surface. The reactant molecule here is denoted by ML_n where M is the metallic atom and L is the accompanying ligand [16]. The reactant molecule splits on reaction and one of its ligands then combines with a surface ligand -a which forms a volatile gas-phased by product, aL, which is then released. This reaction is:

$$|| - \boldsymbol{a} + \boldsymbol{ML_n}(\boldsymbol{g}) \Leftrightarrow || - \boldsymbol{ML_{n-1}} + \boldsymbol{aL}(\boldsymbol{g}) \qquad (2.5)$$

Here the || denotes the surface.

- *Dissociation*

Dissociation is defined as the splitting of an incoming precursor molecule (ML_n) into separate fragments which occupy separate reactive sites (M′-L) as in equation :

$$|M' - Z|| + ML_n(g) \Leftrightarrow ||M' - L + ||Z - ML_{n-1} \quad (2.6)$$

Similar to the previously mentioned ligand exchange, dissociation reactions may continue to occur on the surface. This however has little to no effect on the number of bonded atoms or ligands. [16] [17]

- *Association*

The association method involves the incoming reactive molecule ML_n forming a bond with an active surface site. The molecule is chemisorbed without the detachment of the ligand.

$$| + ML_n(g) \Leftrightarrow || \dots ML_n \quad (2.7)$$

This bond can either form between the central ion M and the surface site or the ligand L and the surface site. [16] [17]

2.8 ALD Temperature Window

The temperature window is the range in which an ALD process displays well behaved self-limiting film growth. For ALD, this window is usually in the range of 150- 400°C, although exceptional cases do exist for thermally fragile substrates such as polymers or biological samples. Deposition attempts below the lower boundary of the temperature window will result in non-ALD type deposition. Depending on the individual precursor, deposition below the deposition window can result in an increased or decreased GPC. The lack of heat energy can result in incomplete surface reactions which would reduce the GPC due to a larger number of cycles needed to obtain saturation. At even lower temperatures, precursors tend to condense on the substrate surface without chemisorption which can increase the GPC dramatically. Alternatively, at temperatures above the temperature window the precursor molecule, or reactant molecule [20] [21] can decompose before reacting or desorb from the surface after reacting resulting in an increased and decreased GPC respectively. [11] [22]

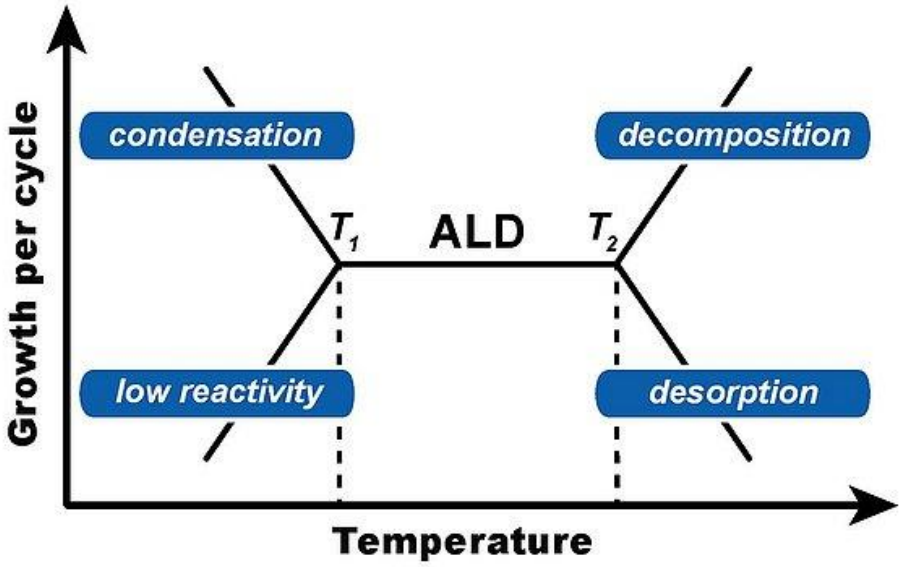

Figure 1.2 Schematic of a general deposition temperature window including the effects of low and high temperatures on the precursor *[32]*

2.9 ALD of Titanium Dioxide

2.9.1 $TiCl_4$ precursor

Titanium is a transition metal which is found in nature only as an oxide as rutile, anatase and brookite. Due to its high refractive index, high stability and suitable bandgap, it is widely used in paint and sunscreen, and other applications which require it to absorb harmful UV rays. This property also means that it acts as an effective photocatalyst for photoelectron-chemical cells. TiO_2 has been shown to be resistant to corrosion when placed in aqueous environments due to its smooth and conductive layers [23]. The first work on ALD mechanism of TiO_2 on silica was in the early 90's *Ritala et al.* and used an inorganic $TiCl_4$ precursor and H_2O as its reactant. This precursor was

a suitable candidate for this work as it is highly reactive towards hydroxyl groups as shown in the reaction mechanism below:

$$n(-OH) + TiCl_4(g) \longrightarrow (-O-)_n\, TiCl_{4-n}(s) + n\, HCl(g) \quad (2.8)$$

$$(-O-)_n\, TiCl_{4-n}(s) + (4-n)H_2O(g) \rightarrow (-O-)_n TiCl_{4-n}(s) + (4-n)HCl(g) \quad (2.9)$$

When the $TiCl_4$ is introduced to the reaction chamber and exposed to the hydroxyl covered surface, it reacts very readily producing HCl gas as seen in equation 2.8. In the following reactant pulse, the surface $(-O-)_n\, TiCl_{4-n}(s)$ species react with the incoming water which again produces HCl resulting in a hydroxyl terminated surface.

As previously mentioned, this is the ideal theoretical reaction mechanism and in reality, there are many competing reactions at play. It is unlikely for the surface hydroxyl groups to be completely terminated as there may be bridged hydroxyl groups between two surface cations. This will result in different chemical behaviour for each ALD cycle. Bridging hydroxyl groups are polarized by the cations and are thus more acidic and so terminated groups are more basic [24]. In ideal cases, the surface hydroxyl groups would only react with the incoming $TiCl_4$ but instead they can condense with each other:

$$Ti(OH) - O - Ti(OH)(s) \longrightarrow Ti(-O-)_2\, Ti(s) + H_2O\ (g) \quad (2.10)$$

$$2 - Ti(OH)(s) \longrightarrow -Ti - O(s) + -Ti(s) + H_2O \quad (2.11)$$

Equation 3.10 shows the case where the hydroxyls are adjacent to each other. The remaining oxygen coordinates with the remaining oxygen. This mechanism is present at low temperatures when the terminal hydroxyls are adjacent to the hydrogen bond interaction [25]. In the case that they are isolated as in equation 3.11, the leftover oxygen is coordinated to only one cation, leaving the other one unsaturated. As mentioned, reaction 2.10 is more favourable at lower temperatures due to hydrogen bonded hydroxyls being more susceptible to dihydroxylation than the isolated hydroxyls in reaction 2.11. The above mechanisms assume that the precursor only reacts with the hydroxyl groups but it can also react with the oxygen bridges:

$$Ti(-O-)_2Ti + TiCl_4 \longrightarrow Ti(Cl) - O - Ti(OTiCl_3)(s) \quad (2.12)$$

The absence of a gaseous product from this reaction makes it less entropically favourable than 2.8. Another element that can complicate the film growth is the possibility of HCl adsorption to the TiO_2 surface:

$$Ti - OH(s) + HCl(g) \longleftrightarrow Ti(H_2O) - Cl \longleftrightarrow Ti - Cl(s) + H_2O(g) \quad (2.13)$$

$$Ti(-O-)_2\, Ti(s) + HCl(g) \longleftrightarrow Ti(OH) - O - Ti - Cl(s) \quad (2.14)$$

The complicated nature of this reaction results in competing reactions within the reaction chamber. During the ALD cycle, the hydroxyls on the sample surface can react with the incoming $TiCl_4$ as in equation 2.8 or with HCl as in equation 2.13. The only reactions from this set that results in a deposited TiO_2 film are equations 2.8 and 2.13 but the alternative dehydroxylation reactions, equations 2.10 and 2.11 must also be considered.

Halogenated precursors are commonplace in ALD process due to their high reactivity and relatively small ligand size, the latter being beneficial by not blocking the active surface sites resulting in better coverage. There are some major drawbacks to these precursors however, in this case, unintentional contamination of the Cl within the film being deposited and the highly corrosive nature of the by-products (HCl). Industry has been making the switch to metal-organic precursors in recent years which by in large require less harsh growth by-products and a higher growth rate at lower temperatures [26].

2.9.2 TDMAT Precursor

The TDMAT precursor is widely used in ALD due to its deposited film being more uniform and more conductive than its organo-metallic competitors like TTIP [27]. Compared to the previously

mentioned $TiCl_4$, TDMAT has a relatively low vapour pressure and so significant precursor heating is required, however the growth temperature can be significantly lower and a more linear GPC trend with temperature is observed.[28] TDMAT can be used in conjunction with H_2O, H_2O_2 and O_3 gasses to deposit TiO_2 films with H_2O being the most widely used reactant. The ability of TDMAT to deposit at lower temperatures makes it a good candidate when depositing on temperature sensitive materials such as electronics or adding layers to already deposited thin films that maybe thermally sensitive.

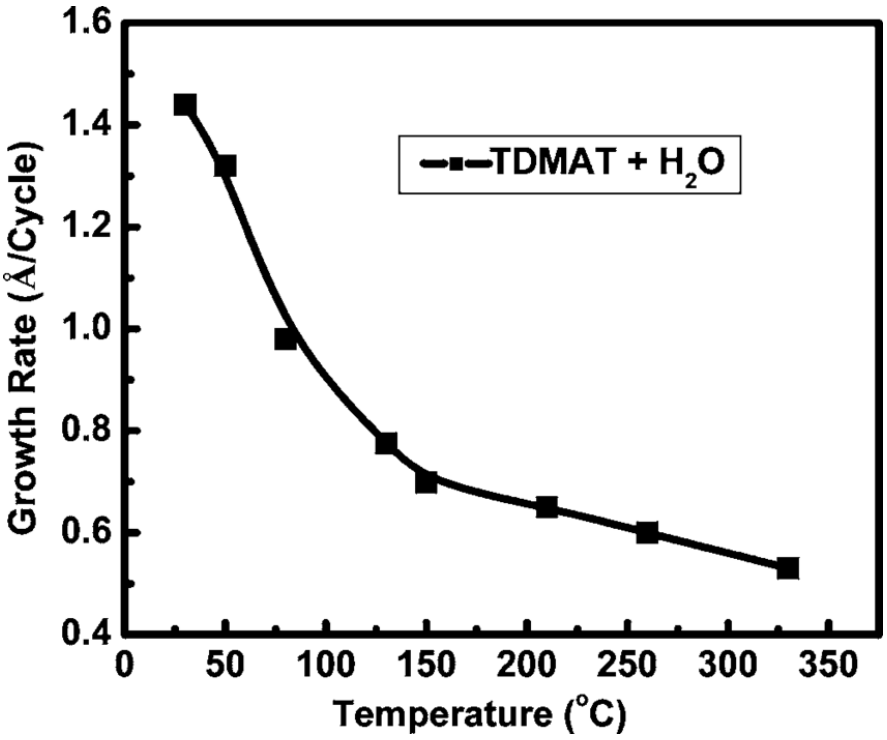

Figure 2.3: GPC of TiO_2 deposited using TDMAT and H2O as a function of deposition temperatures. [37]

Problems can arise at higher deposition temperatures however as TDMAT starts to decompose at ~250°C [29]. The growth rate throughout the deposition window can be seen in figure 2.3 above. There can be a sharp increase in GPC above 250°C in some cases, this can be attributed to said decomposition of TDMAT and also an increasing chemical vapour deposition effect [30].

The reaction mechanism for TDMAT and H_2O is split into 2 half reactions:

$$Ti(N(CH_3)_2)_4 + TiO_2 - OH^* \longrightarrow NH(CH_3)_2 + TiO_2 - O - Ti(N(CH_3)_2)_3 * \quad (2.15)$$

$$Ti\,O_2 - O - Ti(N(CH_3)_2)_3{}^* + 2H_2O \longrightarrow Ti\,O_2 - Ti\,O_2 - OH^* + 3(NH(CH_3)_2) \quad (2.16)$$

Bibliography

[1] R. L. Puurunen, "A Short History of Atomic Layer Deposition: Tuomo Suntola's Atomic Layer Epitaxy," *Chemical Vapour Deposition, vol. 20, pp. 332-344,* 2014.

[2] E. Ahvenniemi, "Virtual PRoject on the History of ALD," American Vacuum Society, vol.86, 2017.

[3] G. Sveshnikova and S. Kol'tsov, "Interaction of titanium tetrachloride with hydroxylated silicon surfaces," *Journal of Applied Chemistry,* vol. 43, pp. 432-434, 1970.

[4] V. B. Aleskovskii, "Chemistry and technology of solids," *J. of Applied Chemistry,* vol. 47, pp. 2207-2217, 1974.

[5] A. Malkov, S. Kol'tsov and V. Ivin, "Effect of surface modification of carbon fibers with titanium oxide groups on their reactivity," *J. Applied Chemistry,* vol. 49, pp. 1650-1652, 1976.

[6] V. Krilov, M. Mironova and V. Drozd, "Influence of oxides interlayers on the properties of contact metal-semiconductor," *Fizika i Technika Poluprovodnikov,* vol. 13, pp. 2272-2274, 1979.

[7] S. Kol'tsov and A. Volkova, "The method of synthesis of Cr(III) and P(V) oxide layers on the silicagel surface.". USSR Patent 422446, 5 April 1972.

[8] T. Suntola, "Apparatus for performing growth of compound thin films". Finland Patent US4389973A, 28 June 1983.

[9] T. Suntola, "Method for performing growth of compound thin films". Finland Patent US4413022A, 1 November 1983.

[10] S. Bedair, M. Tischler, T. Katsuyama and N. El-Masry, "Atomic layer epitaxy of UI-V binary compounds," *AIP*, vol. 47, no. 51, 1985.

[11] S. M. George, "Atomic LAyer Deposition: An Overview," University of Colorado, Boulder, 2010.

[12] L. Gwangpyo Choi, "Effect of process parameters on surface morphology and characterization of PE-ALD SnO2 thin films for gas sensing," *Applied Surface Science*, vol. 252, no. 22, pp. 7878-7883, 2006.

[13] J. Musschoot, D. Deduytsche and H. Poelman, "Comparison of Thermal and Plasma-Enhanced ALD/CVD of Vanadium Pentoxide," *J of The Electrochemical Society*, vol. 156, no. 7, pp. 122-126, 2009.

[14] O.-K. Kwon and J.-H. Kim, "Atomic Layer Deposition of Ruthenium Thin Films for Copper Glue Layer," *Journal of The Electrochemical Society*, vol. 151, no. 2, pp. 109-112, 2004.

[15] D. R. Borris, V. D. Wheeler and N. Nepal, "The role of plasma in plasma-enhanced atomic layer deposition of crystalline films," *J. of Vacuum Sciences and Technology*, vol. 38, no. 4, 040801, 2020.

[16] R. Puurunen, "Growth Per Cycle in Atomic Layer Deposition: A Theoretical Model," *Chemical Vapour Deposition*, vol. 9, no. 5, pp. 249-257, 2003.

[17] R. L. Puurunen, "Surface chemistry of atomic layer deposition: A case study for the trimethylaluminum/water process," *Journal of Applied Physics*, vol. 97, no. 12, 2005.

[18] E. a. D.V Nararov, "Atomic Layer Deposition of Tin Dioxide Nanofilms: A Review," Advanced Study Centre, St Petersburg, 2015.

[19] M. Pessa and C. H. Goodman, "Atomic Layer Epitaxy," *Journal of Applied Physics,* vol. 60, no. 3, pp. 65-82, 1986.

[20] J. W. Elam, D. A. Baker and A. J. Hryn, "Atomic layer deposition of tin oxide films using tetraki(dimethylamo) tin," *Jornal of Vacuum Science & Technology,* vol. 26, no. 2, pp. 244-252, 2008.

[21] T. Muneshwar, G. Shoute and D. Barlage, "Plasma enhanced atomic layer deposition of ZnO with diethyl zinc and oxygen plasma: Effect of precursor decomposition," *J. Vacuum Science & Technology,* vol. 34, no. 5, 050605, 2016.

[22] J. S. Ponraj and G. Attolini, "Review on Atomic Layer Deposition and Applications of Oxide Thin Films," *Critical Reviews in Solid State and Materials Sciences,* vol. 38, no. 3, pp. 203-233, 2013.

[23] Y. Chen, J. Prange and S. Duhnen, "Atomic layer-deposited tunnel oxide stabilizes silicon photoanodes for water oxidation," *Nature Materials, vol. 10, pp. 539-544,* 2011.

[24] M. M.Ritala, "Growth of titanium dioxide thin films by atomic layer epitaxy," *Thin Solid Films, vol. 225, no. 1, pp.288-295,* 1993.

[25] M. Primet, P. Pichat and M. Mathieu, "Infrared Study of the Surface of Titanium Dioxides.," *The Journal of Physical Chemistry, vol. 75, no. 9, pp. 1216-1220,* 1970.

[26] T. Uustare, J. Aarik, A. Aidla and H. Mandar, "Atomic layer deposition of titanium dioxide from TiCl4 and H2O: investigation of growth mechanism," *Applied Surface Science,* vol. 172, no. 1, pp. 148-158, 2001.

[27] M. Dunfond, M. Diouf, C. Badie and C. Laffon, "Quantifying the Extent of Ligand Incorporation and the Effect on Properties of TiO2 Thin Films Grown by Atomic Layer

Deposition Using an Alkoxide or an Alkylamide," *Chemistry of Materials,* vol. 32, no. 4, pp. 1393-1407, 2020.

[28] Q. Xie and Y.-L. Jiang, "Atomic layer deposition of TiO2 from tetrakis-dimethyl-amido titanium or Ti isopropoxide precursors and H2O," *Journal of Applied Physics, vol. 545, pp. 176-182,* 2007.

[29] D. Nazarov, I. Ezhov and N. Yudintceva, "MG-63 and FetMSC Cell Response on Atomic Layer Deposited TiO2 Nanolayers Prepared Using Titanium Tetrachloride and Tetraisopropoxide," *Coatings, vol. 12, pp. 668-687,* 2021.

[30] B. Abendrotha, T. Moebusa, S. Rentropa and R. Strohmeyera, "Atomic layer deposition of TiO2 from tetrakis(dimethylamino)titanium and H2O," *Thin Solid Films, vol. 545, pp. 176-182*, 2013.

[31] ctechnano, "What is Atomic Layer Deposition ALD," ctechnano, San Sebastian.

[32] M. N. Mullings, C. Hagglund and S. F. Bent, "Tin oxide atomic layer deposition from tetrakis(dimethylamino)tin and water," *Journal of Vacuum Science & Technology,* vol. 31, no. 6, 061503, 2013.

[33] Q. Xie and Y. Jiang, "Atomic layer deposition of TiO2 from tetrakis-dimethyl-amido titanium or Ti isopropoxide precursors and H2O," *Journal of Applied Physics,* vol. 545, pp. 176-182, 2007.

Chapter 3

3. Theory of Experimental methods

3.1 X-ray photoelectron Spectroscopy

X-ray photoelectron Spectroscopy or XPS is a higher energy version of the photoelectric effect previously discussed in chapter 1. Its primary function is identifying the chemical species on the sample surface as well as their chemical state, electronic structure and overall density of electronic states within the sample material. The process relies on the absorption of an incident X-ray by a core atom which in turn releases an electron with a certain kinetic energy E_k. The measured kinetic energy of this electron at the spectrometer detector is directly related to the binding energy of the electron. The fermi levels of the sample and the spectrometer line up since they are in contact and thus E_k will be a function of the binding energy:

$$E_b = hv - E_{sp} - q\varphi_{sp} \tag{3.1}$$

Where hv is the incident x-ray energy, E_b is the electron binding energy and φ_{sp} is the work function of the spectrometer.

3.2 Spectroscopic Ellipsometry

Spectroscopic ellipsometry is an optical technique which uses polarized light to measure the dielectric constants of materials at and close to the surface of the sample. Ellipsometry data tells

us primarily about the thickness of the film but can also determine the bandgap of a dielectric material. Polarized light (usually linearly) falls onto the sample where it interacts with the atoms at the material surface. while the reflected beam is then directed into a detector where the difference in polarization is detected. The incident light, which can be characterized by its amplitude component Ψ and its phase difference Δ, reflects off the sample surface changing the polarity to elliptical. The polarization of incident light can be split into the s & p components for which oscillate perpendicular and parallel to the sample surface respectively. The change in polarization is then obtained by calculating the complex ratio of the resultant reflected s & p components. Bandgap cannot be directly obtained from SE and must be calculated using measured coefficients from the SE process. Because TiO_2 absorbs in the shorter visible and UV range, the Tauc Lorenz model can be employed here to fit the complex refractive index and thus calculate the bandgap [1]. Using the raw absorption and wavelength data from SE and equations3.2 and 3.3 below, a Tauc plot can be made and thus a value for bandgap can be found.

$$a = \frac{4\pi k}{\lambda} \tag{3.2}$$

$$ahv = (hv - E_g)^m \tag{3.3}$$

Where a and k are optical constants relating to Ψ and Δ, λ is the incident wavelength, hv is the energy of an incident photon, E_g is the bandgap of the material, m is related to the type of bandgap within the material (m=1/2 for a direct semiconductor and m=2 for an indirect semiconductor.

Using these equations, expressions for energy E_g and plot it against $(ahv)^{1/m}$ creating a Tauc plot. Extrapolation of the linear region and finding the x-intercept on the plot will give the material bandgap [2].

3.3 Photoelectrochemical Measurements

To carry out the photoelectrochemical experiments a PTFE photoelectrochemical cell (PEC) was constructed. As mentioned in chapter 2, the performance of the sample under test within the PEC

is measured by the generated current vs voltage which in turn is correlated to the amount of oxygen & hydrogen that are being produced. The cell in question consisted of a reference electrode (Ag/AgCl), a semiconducting working electrode (WE) and a metal counter electrode (CE) which are all immersed in the electrolyte. A circular opening above the working electrode allowed the electrolyte to come in contact with it and it is the area of this opening that tells us the illumination area. The cell also has a small opening on the top side to enable the use of a light source for photo-generated current experiments. To avoid leakage, a gasket was employed as seen below, to ensure a tight seal between the cell and the baseplate. The openings, depicted in the schematic of figure 3.1 (a), use pipe fittings to ensure that experiments can be conducted in an enclosed system or, if necessary, allow the addition of a gas detection sensor to calculate oxygen/hydrogen production or a camera to monitor bubbles forming on the electrode surface.

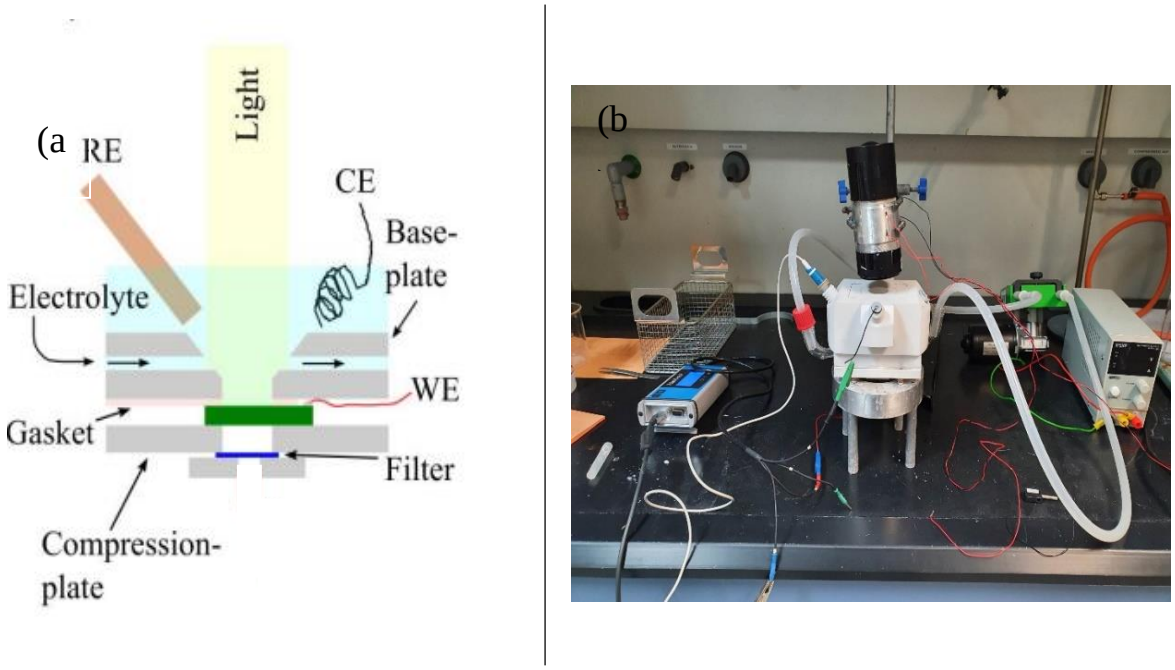

Figure 3.1: (a) a schematic cross-sectioned view of the PTFE cell used in this work. (b) Photograph of the cell setup within the lab in this instance with a high powered LED on top.

electrode. A peristaltic pump was connected to the cell to circulate the electrolyte and avoid bubble/pH build-up at the WE over prolonged measurements. It should be noted that significant optimisation of the pump speed, using a variable power source, was required to avoid bubbles forming in the electrolyte.

The standard potential V^0 of the reference electrode used in this work is + 198 mV (RedRod) versus the standard hydrogen electrode (SHE). The potential of a PEC cell is usually expressed vs the reversible hydrogen electrode (RHE) and this conversion can be done using a variation of the Nernst equation:

$$V_{RHE} = V_{Ag/AgCl} + V^0{}_{Ag/AgCl} + 0.059pH \quad (3.4)$$

$$V_{RHE} = V_{measured} + V^0{}_{ref} + 0.059pH \quad (3.5)$$

Where $V_{Ag/AgCl}$ is the measured potential, V^0 is the standard potential for Ag/AgCl electrode which is +198mV as mentioned above. A potentiostat was used for the electrochemical measurements in these experiments (PalmSens 3) in order to control the current/voltage applied. The counter electrode employed was a platinum wire mesh which would provide a much greater surface area than the working electrode which is crucial to ensure that charge transfer between the two electrodes is not the rate limiting factor of the experiments. Since the oxidation and reduction of water are the reactions, these experiments are concerned with, an aqueous electrolyte is used. In this case, the ferri/ferrocyanide ($K_3Fe(CN)_6$, $K_4Fe(CN)_6$) redox couple was employed (10 mM of both) in a supporting electrolyte of KCl (1M).

3.3.1 Chronoamperometry

Chronoamperometry is a technique used to study reaction kinetics, adsorption and diffusion of a sample within an electrolyte. Unlike cyclic voltammetry, a fixed potential is applied to across the WE & CE and the current change within the system overtime is measured. Along with high conductivity and transparency, stability is an essential property of a photoanode. A stable photo-anode would retain its initial current over time as opposed to an unstable anode which would see a decrease in current as the experiment goes on. This drop in current can be down to a number of factors like formation of a hydroxide layer, corrosion of the surface layer or even bubbles trapped at the surface of the anode if the electrolyte isn't sufficiently circulated. By applying a voltage and measuring the current drop over a time, one can get an idea of the corrosion resistive abilities of the outer protective layer of the electrode. Another form of this technique is often used in

electrochemistry also where a current is fixed at a certain value and the fluctuation of potential over time is measured which is called chronopotentiometry.

3.3.2 Cyclic Voltammetry

Cyclic voltammetry is an electrochemical technique which measures the dependence of current response of a system on an applied potential. Much like other forms of voltammetry, CV uses a 3 electrode setup consisting of a working electrode, reference electrode and a counter electrode. Measurements are obtained by ramping the potential between the working and reference electrodes (usually Ag/AgCl or SCE) while simultaneously measuring the current flow between the working and counter electrodes. To ensure the oxidative and reductive current is measured, the voltage is swept from negative to positive and then back again to ensure These two data sets are then compiled and plotted against each other to produce the cyclic voltammogram. In order for charge carriers to travel between electrodes a conducting medium is required called an electrolyte. These include most soluble salts, acids and bases which need to be dissolved in a polar solvent such as water. The Ferri/ferrocyanide redox reaction is often used due to the electron transfer between the solution and the electrodes being fast and so the reaction kinetics within the electrode itself can be studied. In this one electron reaction, the ferricyanide ion $Fe(CN)_6^{3-}$ acts as the oxidant while the ferrocyanide ion $Fe(CN)_6^{4-}$ acts as the reductant [3].

$$Fe(CN)_6^{3-} + e^- \underset{Oxidation}{\overset{Reduction}{\Longleftrightarrow}} Fe(CN)_6^{4-} \qquad (3.6)$$

As the oxidation current increases, the concentration of the $Fe(CN)_6^{-4}$ decreases until the maximum potential is reached. When the potential sweeps to negative the $Fe(CN)_6^{3-}$ is then reduced as in equation 3.6 resulting in a cathodic current which then reaches a maximum as all of the $Fe(CN)_6^{3-}$ is consumed.

.

3.4 Electron-beam Evaporation

Electron beam evaporation is a method used for thin film deposition. A stream of electrons is used to bombard a target anode, which is the source material that is being deposited, which heats the anode and transforms the target material into its gas phase. The electron beam is given off by a under high vacuum and highly controlled. Once the source material is in its gas phase it is then deposited onto the sample which is placed in the vicinity. The E-beam evaporation system allows for there to be multiple source materials within the chamber at any one time which can be rotated into the path of the electron beam allowing for sequential deposition of different materials to the same sample without the need to break vacuum.

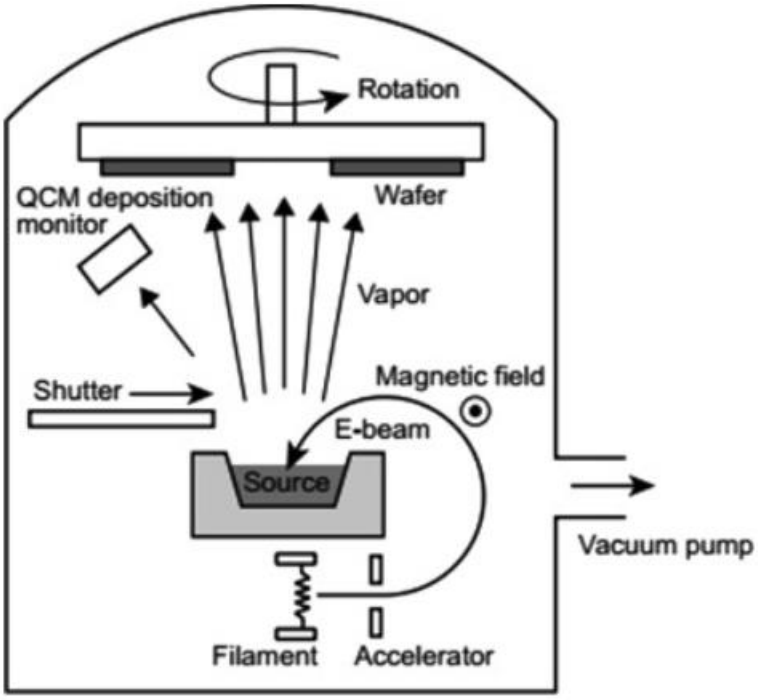

Figure 3.2: a schematic of an electron-beam evaporation system showing the main features [14]

The system is made up of two main parts as seen in figure 2.4. The electron source or gun and the crucible where the source material is housed. The electron source is usually a filament of tungsten which is surrounded by magnets which will guide the beam of electrons to the crucible. The amount of material deposited can be adjusted by the amount of current applied to the filament which in turn determines the heat of the filament. The crucible can be made from a variety of materials according to the melting point of the source material held within it. The crucible may be

made from tungsten or copper or for materials with a very high melting point, a ceramic bowl can be employed. Usually, there is 4 different segments which house 4 different crucibles of different materials. This part of the system is usually water-cooled to ensure that particles from this holder are not mixed with the source material in the gas phase [4].

Bibliography

[1] D. Abou-Ras, T. Kirchartz and U. Rau, Advanced Characterization Techniques for Thin Film Solar Cells, Weinheim, Wiley, 2011.

[2] H. Fujiwara, Spectroscopic Ellipsometry: Principles and Applications, Japan, Wiley, 2007.

[3] T. Tezuka, "ALS Co. Electrochemistry and Spectroelectrochemistry," 2020. [Online]. Avalable: https://www.als-japan.com/1822.html. [Accessed Spetember 2022].

[4] K. S. Harsha, Principles of Vapor Deposition of Thin Films, San Jose, Elsevier, 2006.

Chapter 4

4. Experimental Procedures

4.1 Sample Fabrication

4.1.1 Silicon wafers

4 different types of Silicon wafers were used in this work. Moderately phosphorous doped (100) n-type silicon wafers (ρ = 0.14 - 0.24 Ω.cm, thickness = 450μm) were used to create a Schottky junction photoanodes for electrochemical measurements. Degenerately boron doped (100) p-type silicon wafers (ρ=0.001-0.002 Ω·cm) were used to act as conducting electrodes when carrying out water oxidation experiments in the dark. Buried junction devices were also fabricated in order to provide a high concentration of charge carriers built within the silicon. The first step in this process was to clean the substrates using the Semitool spray acid tool. First the Si wafers are cleaned using deionised (DI) water and ozone, followed by NH_4OH (2000:1) exposure in order to remove particulates and organics. The last step is to add DI water and ozone along with HF (1150:1) which helps regenerate the surface oxide and removes any metallic species left over on the surface. After this clean, the wafers were then implanted with $4x10^{15}$ cm^2 of boron at 15 keV. These samples were then annealed at 950°C for 40 minutes, initially in a mixture of O_2/N_2 and then just N_2 for the remainder. The surface of the wafer was bevelled at a known angle θ through the p+ region which allowed for the determination of its depth using optical measurements and geometry. The depth of this region was calculated to be ~450 nm. The procedure for implantation of n-type region into p-type was similar however it was instead $5x10^{13}cm^2$ phosphorous at 110keV. The annealing conditions were also different with the n+p being annealed for 60 minutes in only N_2.

4.1.2 Wafer Cleaning and preparation

For these experiments, TiO_2 was deposited directly onto several different types of Silicon substrates using the ALD method. Before the native oxide can be grown on the surface, the wafers (100) were primed using a three part cleaning process: 10 minutes at 50°C exposed to 5:1:1 H_2O:H_2O_2:NH_4OH to get rid of any trace metal ions on the surface. The next step was a 30 second bath in 2% hydrofluoric acid to remove the SiO_2 that is present. The last step is then to spin dry the wafers leaving a hydrogen passivated outer layer which is then ready for deposition. The slot plane antenna (SPA) method was then used to grow a precise thickness of a native oxide layer. The deposition temperature of the system was set to 500°C and 100 sccm of Argon gas was circulated through the chamber while the system reached equilibrium giving an actual substrate temperature of ~400°C. A 2.45 GHz microwave was used for this method to generate a high density plasma just below the dielectric shower plate. Oxygen was then introduced to the chamber at 400 sccm for 10 seconds while the argon was ramped up to 1500 sccm. To start the deposition process, the microwave power was set to 3000 W, Argon set to 1200 sccm and Oxygen set to 40 sccm for 25 seconds at a chamber pressure of 5 Torr. At the conclusion of the process, Argon and Nitrogen are introduced to the chamber for 5 seconds in order to purge the system. The time of oxygen plasma exposure can be altered to create the desired thickness of SiO_2, for these samples the parameters were set to give an SiO_2 thickness of 1.5nm.

4.1.3 Atomic layer deposition

The atomic layer deposition in this work was done using the Picosun R200 system using the Tetrakisdimethylaminotitanium (TDMAT) as the metallic precursor and either O_2 plasma or H_2O as the oxygen containing co-reagent. The chamber was set at 200°C, falling within the process growth temperature window. The TDMAT precursor was kept at 75°C to ensure the vapor pressure was sufficient to dose the reaction chamber at the selected pulse duration. ALD cycle parameters for grown samples are given in Table 1.4. Purges were set at values previously determined to give a cross wafer thickness uniformity of 5% in line with the equipment site acceptance test.

Sample Name	Si Type	Number of cycles	Oxygen source	TDMAT pulse (s)	TDMAT purge (s)	Oxidizer pulse (s)	Oxidizer purge (s)
1TP1	p++	146	O_2 Plasma (3kW)	0.2	10	8	15
1TP2	n+p						
1TP3	p+n						
2TP1	p++	146	O_2 Plasma (3kW)	0.2	10	4	15
2TP2	n+p						
2TP3	p+n						
3TP1	p++	146	O_2 Plasma (3kW)	0.2	10	18	15
3TP2	n+p						
3TP3	p+n						
4TP1	p++	146	H_2O	0.2	10	0.1	10
4TP2	n+p						
4TP3	p+n						
5TP1	p++	146	H_2O	0.2	10	0.1	10
5TP2	p++	365					
5TP3	p++	731					

Table 4.1: List of samples prepared and their corresponding deposition parameters.

4.2 Material characterization

4.2.1 Oxide layer thickness

To determine the thickness of the deposited TiO_2 layer, spectroscopic ellipsometry measurements were carried out using the Woolham Co. M-2000 ellipsometer. As the majority of the samples were grown in identical conditions, one sample from each batch was tested using this technique. The thickness can also be confirmed using the SEM system by obtaining section views of the cleaved samples however the only system available did not have resolutions high enough to get images in the sub 10 nm range. As consequence, previous calibrations of the ellipsometry measurements were assumed correct.

4.2.2 Back contact & catalyst deposition

The procedure used to deposit catalysts and contacts was the Temescal UFC-4900 e-beam evaporation system. Metallic Nickel (99.99%) and metallic Platinum (99.99%) were deposited as a water oxidation catalyst and a back contact respectively. 5 nm of Ni was deposited on top of the already deposited TiO_2, and 25 nm of Pt was deposited on the back side as an ohmic contact.

4.2.3 Wiring samples

To connect the working electrode to the potentiostat system, a thin silver wire was attached to the deposited Pt on the reverse of the sample using a silver adhesive paste. It is important that the wire is positioned in the middle of the sample device to ensure charge has a direct path through the sample and into the wire.

4.2.4 Electrolyte solution preparation

The redox couple ferri/ferrocyanide was selected for this work to study the charge transport within the PEC system. A 10 mM solution of potassium ferricyanide and potassium ferrocyanide trihydrate were prepared using deionized water along with 1M potassium chloride which was used as a supporting electrolyte to increase the conductivity of the solution by providing more ions.

Chapter 5

5. Results and Discussion

5.1 TiO_2 Optical Characterization

TiO_2 is a widely studied material in the field of ALD and for this reason there is a well-established growth rate across its growth temperature window. Since the majority of the samples were deposited at 200°C The literature GPC is ~ 0.5Å under those conditions. Four different types of Si were loaded into the chamber for each growth, as they all had the same 2 nm native oxide over-layer it is assumed that the doping will not influence the growth mechanism of each TiO_2 layer. Although the position of the samples shouldn't have any bearing on the thickness an error of 5% in thickness is the accepted instrument error across a 10 cm wafer for a well-defined process. The nominal GPC of TiO_2 using our system had to be established prior to the coating of any photoanodes. This estimate was performed by depositing TiO_2 on a Si substrate at 200ºC, running a 200 cycle recipe and measuring the thickness; under these conditions the thickness was determined to be 8.2 nm. Assuming a linear growth rate and no nucleation delay this equates to a GPC at 200°C of 0.04 nm/cycle, this value was used to determine the number of cycles used for the desired thickness. It should be noted that the measured GPC of TiO_2 in our system was slightly below literature growth-rates for TDMAT and H_2O [1][2].

For all samples thickness was measured using the Woolham Spectroscopic Ellipsometry system mentioned in chapter 4. Utilizing the Woolham CompleteEASE software, a preloaded thermal

oxide on Si model was used as well as a TiO_2 Tauc-Lorenz model also on the system. The measured thicknesses and associated errors are shown in table 5.1.

Table 5.1: Thickness measurements of Si/TiO_2 samples determined by spectroscopic ellipsometry.

Sample Name	Si Doping	Number of cycles	Thickness (nm)
1TP1	p++	146	6.3 ± 0.3
1TP2	n+p		6.0 ± 0.3
1TP3	p+n		6.0 ± 0.3
2TP1	p++	146	5.9 ± 0.3
2TP2	n+p		6. 0 ± 0.3
2TP3	p+n		6.1 ± 0.3
3TP1	p++	146	5.7 ± 0.3
3TP2	n+p		6.3 ± 0.3
3TP3	p+n		6.1 ± 0.3
4TP1	p++	146	6.3 ± 0.3
4TP2	n+p		6.5 ± 0.3
4TP3	p+n		6.6 ± 0.3
5TP1	p++	146	6.1 ± 0.3
5TP2	p++	365	14.9 ± 0.7
5TP3	p++	731	30.6 ± 1.5

SEM imaging was also carried out on as deposited TiO_2 on Si, Ni/TiO_2/Si and used Ni/TiO_2/Si anode samples. This however did not give any insight into the thickness of the TiO_2 layers as the maximum resolution was not sufficient to distinguish between the multilayers and confirm the TiO_2 thickness, higher resolution SEM or TEM were not available at the time of fabrication. However, plan view SEM did provide information about the surface characteristics of the photoanodes which will be discussed in section 5.3.

5.1.2 Bandgap

The bandgap of the deposited TiO_2 was determined using the SE system. Using the absorption coefficient and wavelength along with equations 3.3 and 3.4. Figure 5.1 below shows the Tauc plots for unannealed and annealed TiO_2 on Si. A clear difference can be seen between the two data sets with annealed samples undergoing a redshift. By extrapolating the linear region of the data to the x-axis, the bandgap of the material can be estimated. Here for the unannealed and annealed TiO_2 the bandgaps were determined to be ~3.4±0.14eV and 3.2±0.15eV respectively. Annealing conditions effect the stoichiometry of the deposited film. A rise in annealing temperature corresponds to a decrease in "O" atoms present within the film which can be attributed to the out-diffusion of oxygen during annealing [3]

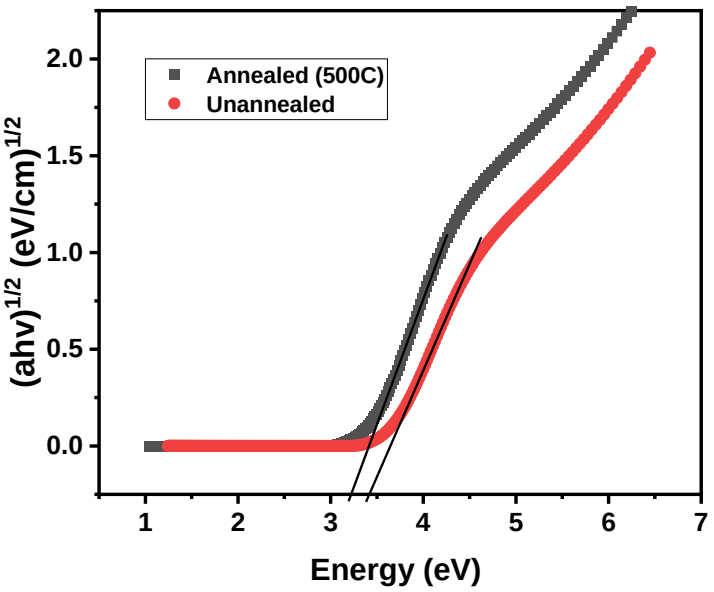

Fig 5.1: Tauc plot showing annealed vs unannealed TiO_2 with the extrapolated diagonal lines indicating the material bandgap.

It should be noted that annealing can also change the crystal phase of TiO_2. from amorphous to anatase to rutile, however, these changes take place at temperatures in excess of ~600°C, which was out of the range of our annealing temperature [4]. The oxygen deficiencies present within the annealed v the unannealed samples would also result in an increase of recombination of charges [3].

5.2 Electrochemical Experiments

Electro and photoelectrochemical experiments were carried out using the fabricated TiO_2 on Si samples. These experiments were carried out in the light and dark and in neutral and pH 14 electrolyte. The cyclic voltammetry experiments were carried out in a ferri/ferrocyanide in KCl solution while water oxidation experiments were carried out in a neutral solution and pH14 KOH solution.

Dark Electrochemical Experiments

The electrochemical work carried out in the dark was mainly carried out using the p++ Silicon samples. The work in the dark is more of a characterization of the different thicknesses and compositions of the protective TiO_2 layers as well as the catalysts. p++ Si is called so due to is highly degenerative doping. Due to its high doping, p++ silicon possesses an abundance of available charge carriers to facilitate the rapid transfer of charge at the electrode-electrolyte interface. When carrying out FFC cyclic voltammetry on these samples, well defined and symmetric oxidation and reduction peaks are expected because of this abundance of charge carriers. While light likely does have an effect on the p++ silicon in the form of inducing charge csrrier generation, the effects are essentially negligible as the surface is already over saturated with available charge carriers.

5.2.1 Different deposition conditions

Ferri/ferrocyanide (FFC) cyclic voltammetry is a technique to characterize the charge transport efficiency across the electrolyte-semiconductor interface. Due to the over-layer of metallic Ni (3nm – E-beam evaporation), the electron transfer between Ferri/ferrocyanide and the electrode is fast and so this allows for the electron transfer across the TiO_2 layer to be characterized. When using p++ Si, the oxidation of ferro cyanide to ferricyanide will be the favoured reaction due to

the abundance of holes available in the bulk. As previously discussed, this will attract negatively charged anions to form the inner Helmholtz plane.

Figure 5.2 shows the cyclic voltammetry of different Ni/TiO_2/Si samples which were deposited under different conditions. This experiment was carried out on p++ type silicon under dark conditions so as just to study the TiO_2 layer itself. The aim of this work was to produce titanium oxide films with different amounts of O incorporated into the films and study the effects this has on oxidation and reduction curves. This was achieved by altering the oxygen pulse times (either over or under pulsed) for the thermal and plasma grown films. Each of the samples in figure 5.2 was deposited at 200ºC.

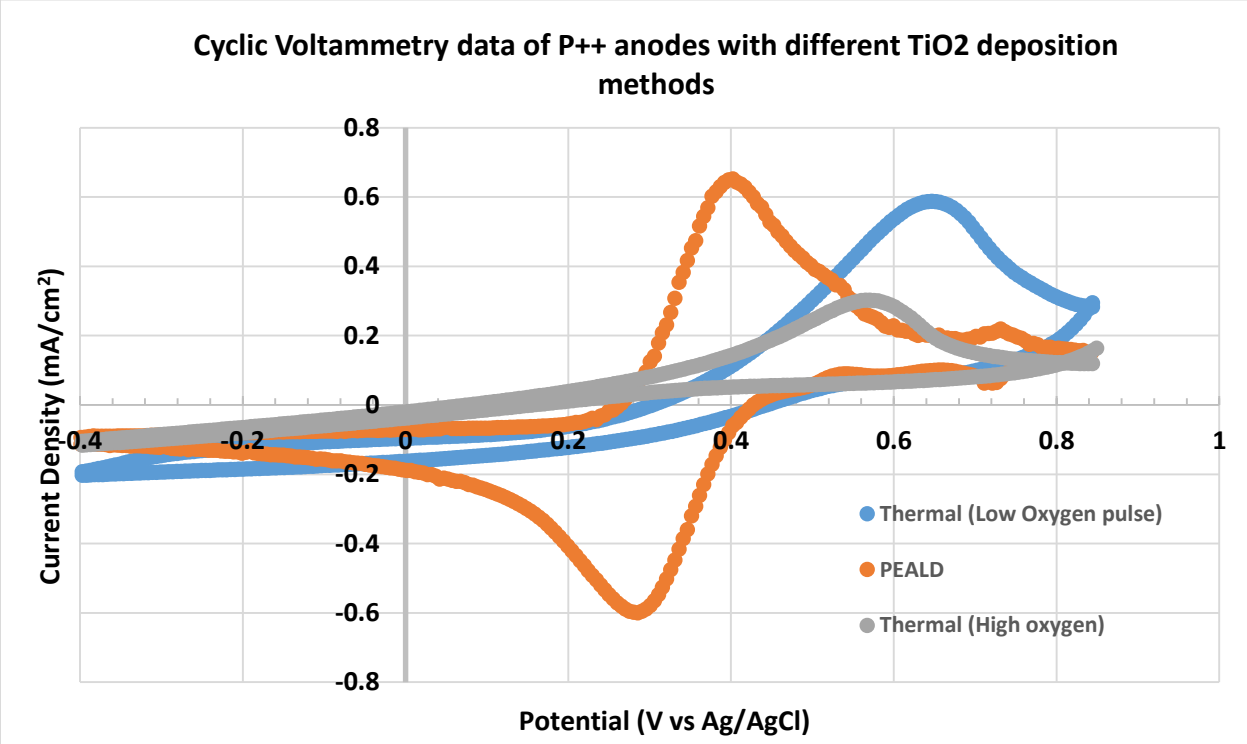

Fig 5.2: Ferri/ferrocyanide Cyclic voltammetry responses for TiO_2 protected anodes deposited under high regular and low oxygen conditions.

The reason behind changing the TiO_2 deposition parameters was to study the performance of films with different stoichiometries and to see if the oxygen vacancies caused by non-stoichiometric films plays a role in their cyclic voltammetry responses. It should be noted that the study is qualitative rather than quantitative as the XPS system was not available at the time of fabrication and as sample storage time of non-stoichiometric samples is critical for their evaluation delayed sample measurements would be of limited value. For the reduced oxygen pulse depositions, the growth rate was reduced dramatically due to the reduced amount of O available to react with the adsorbed surface ligands which will alter the ratio of Ti^{3+} to Ti^{4+}. This meant that the reaction was not surface limited but rather limited by the amount of oxygen present within the reaction chamber [5]. When organic precursors are used, they can also lead to impurities in the film such as carbon and nitrogen however the absence of XPS data prevented the quantification of impurities. The ratio of Ti^{3+} to Ti^{4+} is known to have a major effect on the electronic structure, charge transport and surface activity of the Ti thin films and ultimately controls the degree of leakage current within the film [6]. A spread out of the peak-to-peak voltages can be seen in figure 5.2 which indicates a higher resistive TiO_2 film. The high and low oxygen voltammetry reveal an asymmetry, with the cathodic peaks missing while the anodic peaks remain. Due to the underlying Si being p type, there is a high concentration of holes in the p++-si to rapidly oxidize the Fe(II) but an inherent lack of electrons to sufficiently reduce Fe(III). A result of this is that the electrolyte-anode interface essentially acts as a Schottky junction which then give rise to the asymmetry seen in figure 5.2.

5.2.3 Thickness dependence

We know intuitively, that a thicker layer of TiO2 would mean that the charge carries from the underlying Si would find it more difficult to reach the catalyst-electrolyte interface. When the protective layer is small, additional charge transfer mechanism are available such as tunnelling which would add to the overall conductivity of the device. The more resistive a device would be, the greater the peak to peak voltage would be [8]. Figure 5.3 Shows the cyclic voltammetry responses for p++ samples in a ferri/ferrocyanide solution. Similar to the previous experiments, a 5nm Ni OER catalyst layer was deposited on top as well as 25 nm of Pt on the back to act as a

back contact. Three CV responses can be seen here with a noticeable spreading out of the peak to peak voltage owing to an increase in resistivity of the samples. Greater thickness of the TiO_2 protective layer would ensure a more stable, corrosion

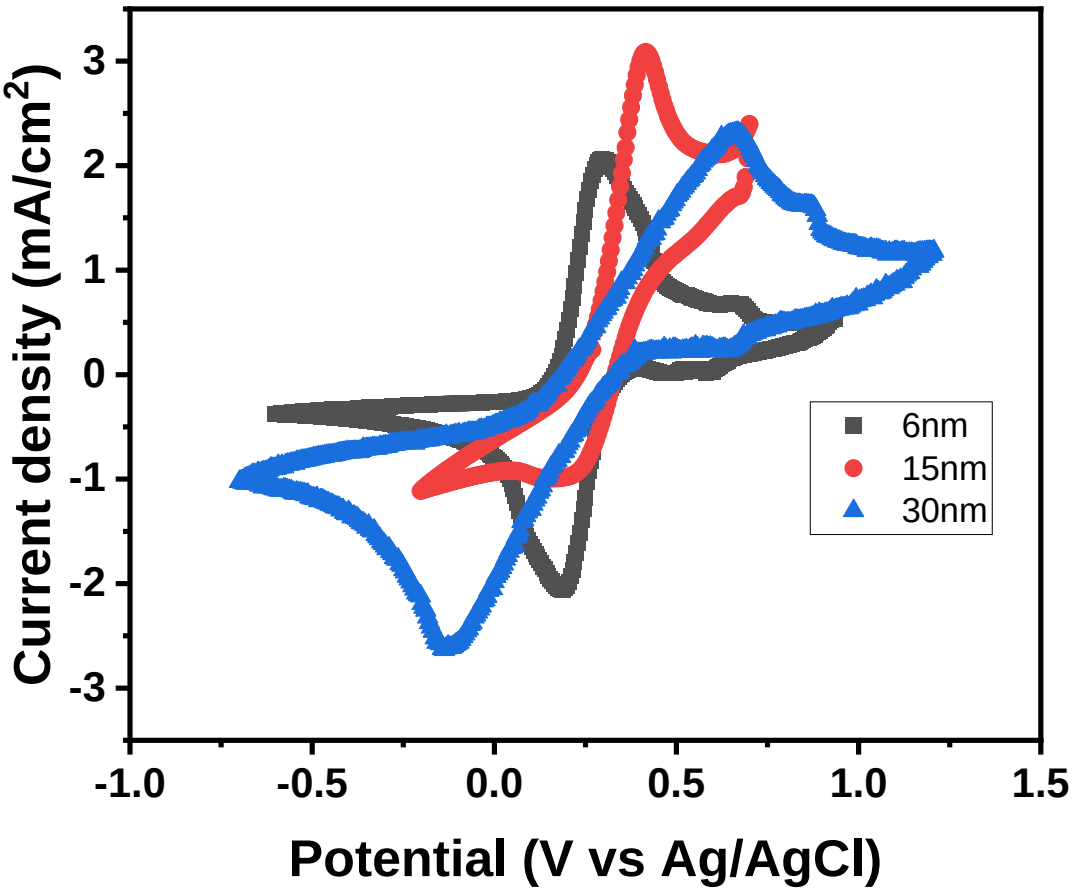

Figure 5.3: Ferri/ferrocyanide response for a Ni/TiO2/SiO2/p++-Si sample in the dark showing the peak to peak voltage dependence on protective layer thickness.

resistant film but a middle-ground must be found between corrosion resistance and conductivity. Thicker TiO_2 samples may experience more recombination within the bulk. The distance the charge carrier must travel back to the Si is greater within thicker samples and given that electron/hole mobility within TiO_2 is relatively slow, the chances of recombination increase with thickness. On the other end of the scale, TiO_2 layers cannot just be made as thin as possible either because of the possibility of surface pinholes which could extend to the Si surface, exposing it to the electrolyte.

A Protective layer thickness study was also carried out by Mcintyre et al. In this work, the thickness of the anode protective layer ranged from 1.2nm to 11.6nm where a clear spreading out of peak to peak voltage can be observed. The 5nm sample is the most comparable to the work carried out above using a 6nm protective layer. The first observation when comparing the results is the positive shift in potential of both the anodic and cathodic peaks. This could be owed to the fact that the work above is using p++ Si as opposed to the p+ used in Mcintyres work. The higher doping could lead to a decreased resistance due to an abundance of charge carriers and so could lead to a positive shift in the CV trace.

Although Mcintyre's work stops at 11.6nm, we can see a clear trend as to what affect the increased thickness has on the device performance. Going by this trend, our results for 15nm and 30nm protective layers seem to agree with this work. The shape of the CV trace for the 15nm sample should also be addressed. The could be a case that the reaction was only quasi reversible due to instability in the system oweing to sample deterioration or possibly impurities within the electrolyte itself [8].

5.2.4 Chronoamperometry Experiments

The stability of a 6nm TiO_2 protective layer was studied using the chronoamperometry technique discussed in section 3.3.1. The aim of these experiments was to compare the CV response of a photoanode sample before and after undergoing chronoamperometry to study the stability of the overlying TiO_2 layer. The current that is seen from this experiment is due to the applied potential being above the over potential required to start an maintain the oxidation reaction and so the transfer of charge is occurring and electrolysis is happening at the electrode surface. The small reduction of current over time seen is a result of the overlying Ni and TiO_2 degrading due to being exposed to the constant oxidizing conditions, but these losses seem relatively small. The difference in the two CV responses will give information of how the TiO_2 layer performed under said oxidizing conditions over time. A reduction in photocurrent density and reaction kinetics between these two responses would signify an increase in resistivity, the blocking of reactive sites on the material surface, corrosion among other facts which will be discussed. Figure 5.4 shows the

chronoamperometry tests carried out on Ni/TiO_2/Si and Ni/Si samples respectively. This tells us the resulting current while applying a fixed potential of 1.6V vs the SHE for an extended period, in this case 4 hours. The sustained near constant current throughout the experiment remained constant for the most part which tells us that the TiO_2 protective layer remained operational throughout, whereas the sample without the protective layer failed within the first 20 minutes. The slight reduction in current overtime for the TiO_2 protected sample could be contributed to the dissolution of the Ni or TiO_2 or the creation of etch holes which could expose the underlying Si. Comparing the two data sets shows a significant improvement of device stability with just a 6nm layer of TiO_2. The potential applied in order to achieve these currents during chronoamperometry tend to be higher than during CV experiments due to inefficient removal of the oxygen generated at the electrode surface (bubble build-up). A peristaltic pump was utilized for this reason when carrying out longer experiments like chronoamperometry

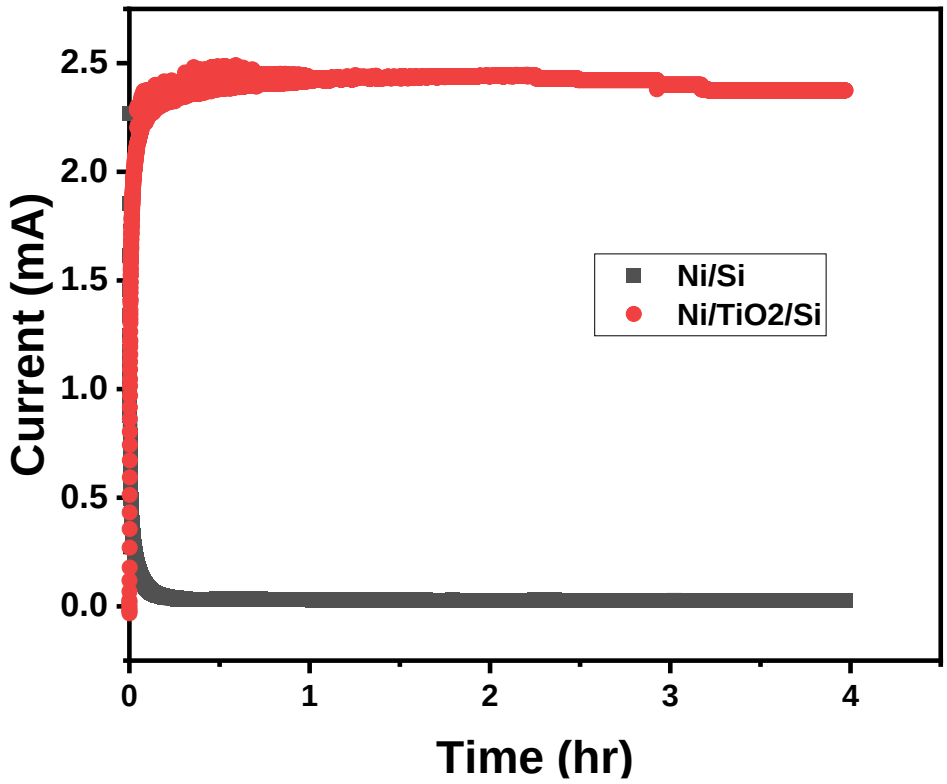

Figure 5.4: Chronoamperometry tests on p++ samples, with and without a TiO_2 protection layer, in the dark at a constant potential of 1.6V vs NHE; a 1M solution of KOH was employed as the electrolyte.

Cyclic voltammetry experiments were carried out before and after the Ni/TiO_2/Si sample underwent chronoamperometry to study the effects of long term water oxidation had on the electrochemical and corrosive resistance performance of the photoanodes. Results can be seen below in figure 5.5 where water oxidation experiments were carried out in 1M KOH before and after the samples had undergone CA. The photocurrent achieved has decreased significantly compared to the pre CA results which can be put down to corrosion of the catalyst layer resulting in a reduced amount of active surface sites. The actual amount of photocurrent achieved is a lot lower than literature values [8][9] which are usually in the 10's of mA range and show a larger onset potential that fall well outside the water oxidation potential of 1.23V. These water oxidation experiment would need to be optimized to see what the limiting factor is and would be essential if further work were to be carried out.

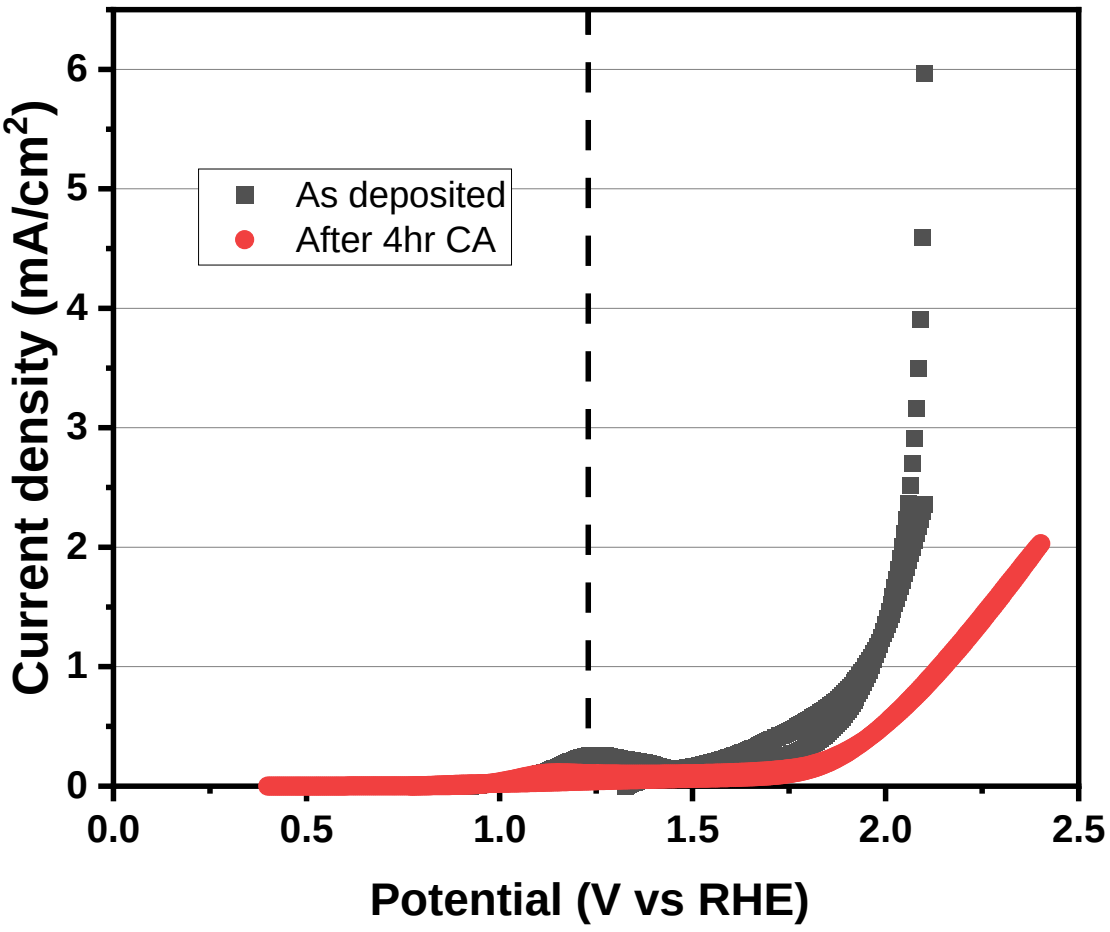

Figure 5.5: Cyclic voltammetry of TiO_2 protected Si p++ electrodes before and after 4 hour stability tests. The dotted line at 1.23V signifies the potential at which water oxidation (O_2/H_2O) occurs at. These experiments were carried out in a solution of 1M KOH.

As can be seen from the CV sweep the photocurrent density of the sample post CA is reduced in line with observations of decreased current over the course of the CA experiment. The spread of the peak potential signifies an increase in resistance of the anode which can be attributed to partial degradation of the electrode through the formation of pinholes, dissolution of the protection layer or oxidation of the Ni catalyst.

Visual inspection of the photoanodes also gives insight into the performance of the samples under test as can be seen in figure 5.6 where the used sample is on the left and the unused sample is on the right. The circle in the centre of the used sample is the area of contact between the surface and the electrolyte during PEC tests. This darker colour signifies the dissolution of the TiO_2 and Ni and so bare Si or the native SiO_2 is all that is left.

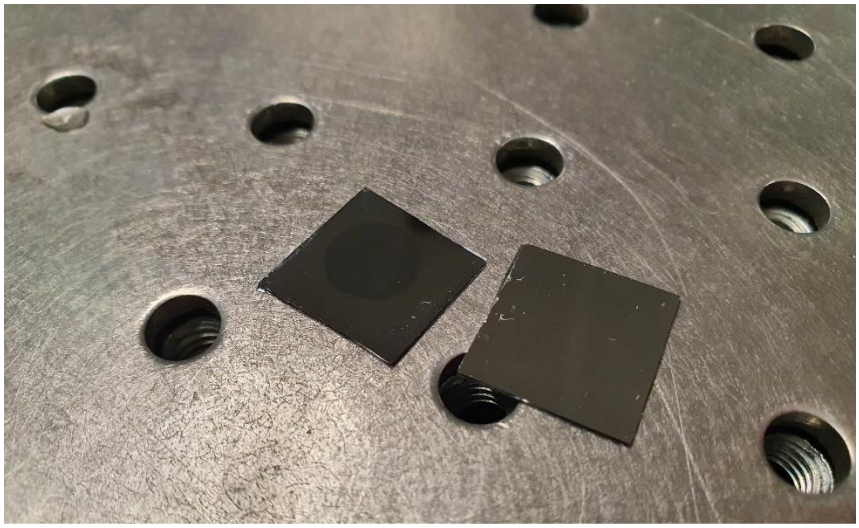

Figure 5.6: a side by side view of the Ni/TiO_2/SiO_2/Si anodes used in this work with a used sample on the left and an unused sample on the right. The circle of darker colour seen in the centre of the used sample was the area of contact with the electrolyte during experiments.

A visual inspection was done on the devices once CA testing was finished with seen in figure 5.6. On the left is the device after undergone CA stability tests and on the right is an unused anode. The darker coloured circle in the middle was the contact area of the anode with the KOH electrolyte which indicates the dissolution of the protective and or catalytic outer layers of the device. The CA results, however, show a steady current over the 4 hr test period with only minor drop over time and so this might suggest that the outer Ni OER catalyst has been corroded away but the TiO_2

protective layer is still present; XPS would confirm this but was not available at the time of this study.

The samples were then prepared for SEM by sonicating in acetone for a short time to remove all of the dried electrolyte and other organic material that may be present. Plan view SEM images are displayed in figure 5.9 of a used Ni/TiO2/Si photoanode. The purple box on each image is where EDX was also carried out on the surface of the samples, to get a further understanding of their condition after testing. Figure 5.9 (a) shows the edge of the circle test area of the used anode. For the corresponding CA results for the used anode a small reduction in current over a 4-hour experiment was observed, which would indicate that there would be little degradation of the protective layer however, comparing the used and unused parts of the SEM image corrosion is clearly visible. Higher magnification images of the test area can be seen in fig 5.9(b) and 5.9(c). An EDX sweep of the area inside the purple square shows that there is C, O, Si, Ti and Ni present with percentage weights of 3.65%, 3.15%, 88.44%, 0.97% and 3.8% respectively. The C present is either atmospheric contamination of the samples post growth or residue from the TiO_2 deposition process as an organic Ti precursor was used. The high percentage of Si present is due to EDX not only scanning the surface but the x-rays penetrating to the silicon substrate. The darker region was confirmed as the corroded area as there was no Ni and only 0.19% Ti detected from its EDX scan. The SEM and EDX data clearly show that there is degradation and in areas complete removal of the catalytic and protective layers. The corresponding EDX spectrum for each of these images is included in Appendix 1 below.

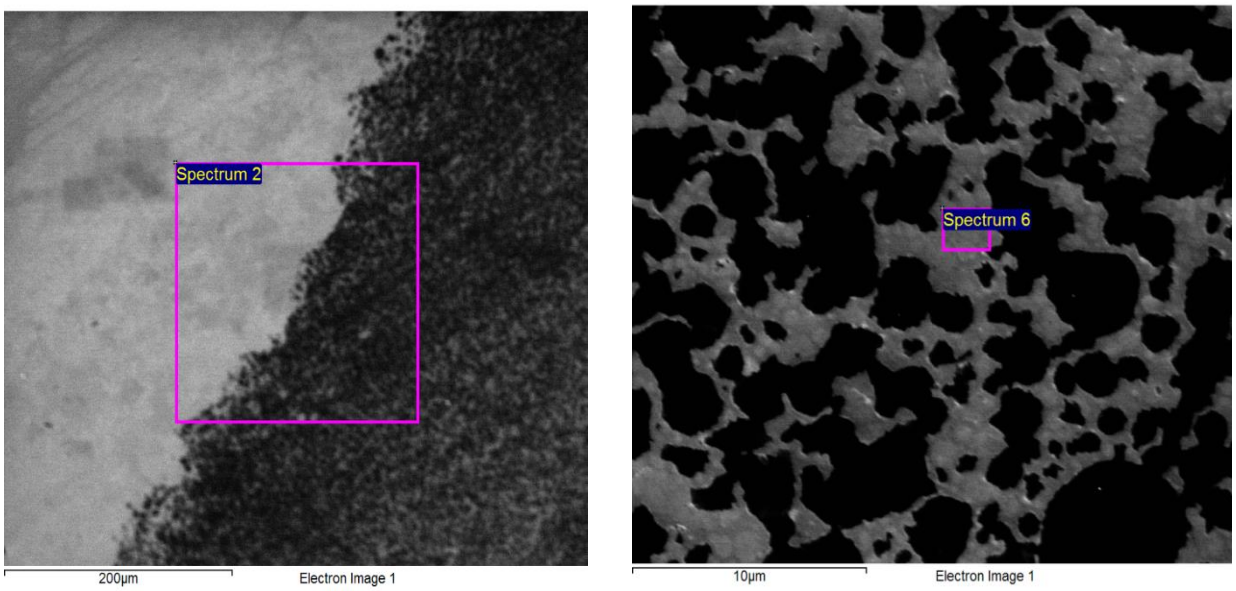

Figure 5.7: SEM images of a used Ni/TiO_2/Si anode; (a) the border region if the area under test (b) higher magnification view of the surface of a photoanode after CA experiments.

Illuminated Electrochemical Experiments

5.2.2 Photovoltage & Water Electrolysis

The photovoltage achieved was the next experiment conducted using the FCC redox couple. This was obtained by comparing the centre points of the CV sweeps for a p++ sample in the dark vs the p+n under illumination. n+p Si was also used in these experiments to try and study the performance of a tandem cell device. As previously mentioned in section 4.1.1 the p+n Si has an inbuilt junction with a hole concentration of ~ 5 x $10^{19}cm^{-3}$ which ensures a high concentration of holes at the anode surface essentially making the photovoltage less effected by the protective layer thickness. To achieve the highest possible photovoltage for a single photoelectrode device, CV of the p++ sample was measured in the dark while the p+n sample was measured under illumination.

To find out what photovoltage is incurred by each photoanode, a CV sweep must be carried out on the device in the dark and then under illumination. The work undertaken by McIntyre et al

showed a comparison of CV sweeps between Ir/TiO2/n-Si photoanodes in the dark and under illumination. The difference between the two CV sweeps can be attributed to the absence of photogenerated holes for the dark sample. With no light to generate holes at the anode surface, there is no charge carries available to oxidize the Fe(II). This is observed as a lack of an anodic peak for the sample [7]. Figure (5.8) below shows the CV sweeps of Ni/TiO2/p+n/Si under illumination and in the dark. A negative shift is seen in the illuminated sample when compared to the dark sample. This negative potential shift was about 0.1V. Another noticeable difference between this and McIntyre's work, particularly for the P+N sample is that the two sweeps look to have an anodic peak but also a somewhat noticeable cathodic peak. As previously mentioned, the p+n Si is used to ensure there is always a higher concentration of holes at the anode-electrolyte interface regardless of illumination or bias. This results in reduced hole extraction barrier causing there to be oxidation and reduction regions regardless of illumination. When the sample is illuminated the photovoltage and photocurrent is increased dramatically. This is due to the creation of electron-hole pairs in both the p and n type regions. The peak current densities are lower in the dark sample which is expected as with the illuminated sample, there is a high density of charge carries at the surface as well as increased carrier availability due to the photogeneration of holes.

For the n+p sample, it is expected to have an opposite effect as we are dealing with p type bulk Si as opposed to n type (figure 5.9). The catalyst used on these samples was platinum to promote the oxygen evolution at the electrode surface. The results here were not as pronounced as for the p+n sample. The dark sample follows similar pattern as with McIntyre's work in that there is much lower current peaks. The oxidation peak can be clearly identified but the lack of even a small reduction peak was not expected when carrying out this work. The n type region should have allowed for a concentration of charge carriers available for reaction at the electrode surface. Reasons for this and for the reduced photovoltage when compared to the illuminated vs dark p+n results could be due to the fact that hole mobility is lower than that of electrons and so the reaction kinetics were too slow in this case. When we look at the silicon samples themselves, the p+n has a much higher concentration of p-type implanted into the surface region than of n type into the p-type region, this concentration could have had an effect also.

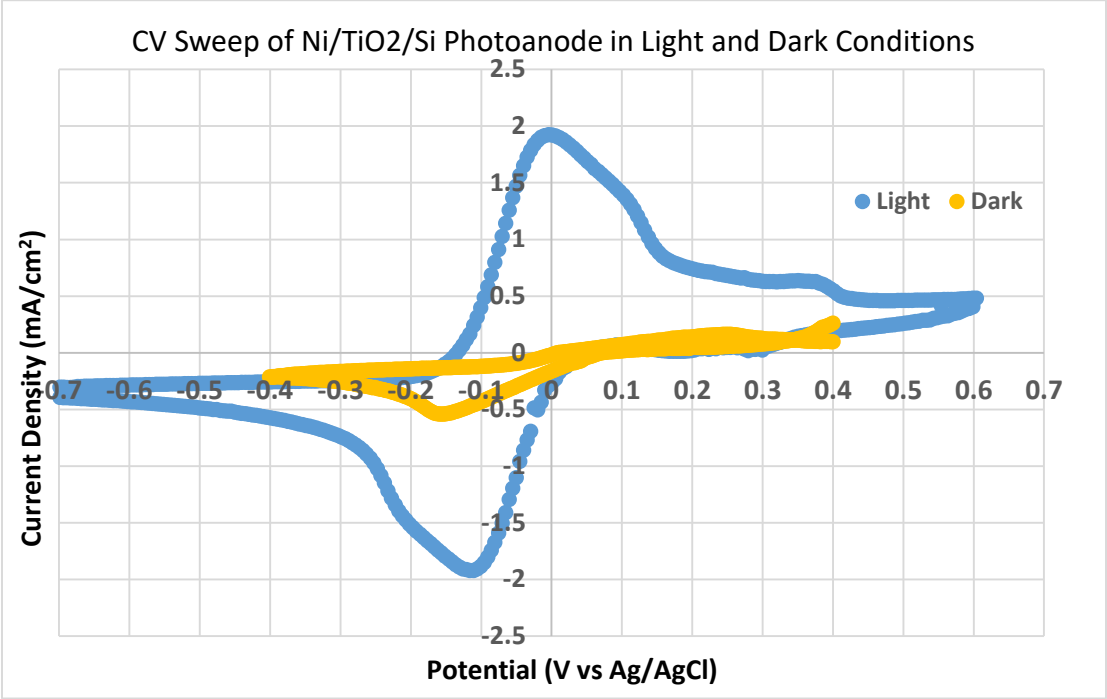

Figure 5.8: Ferri/ferrocyanide response for a Ni/TiO2/SiO2/p+n-Si sample in the dark (yellow) and in the light (blue)

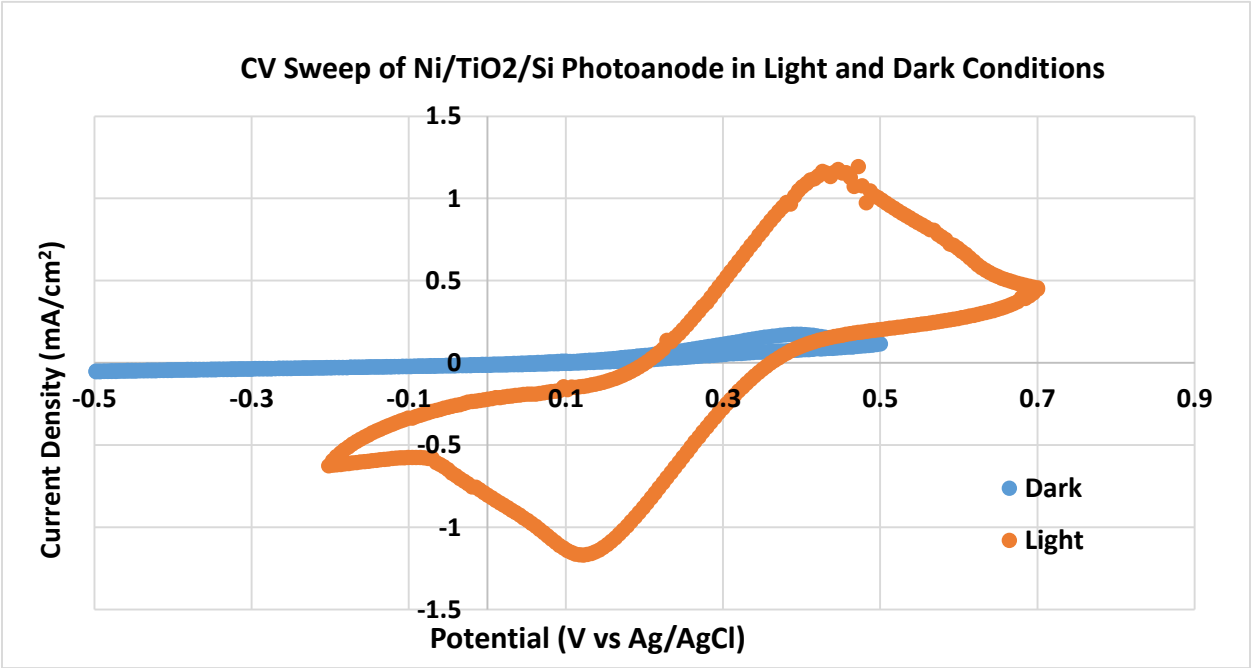

Figure 5.9: Ferri/ferrocyanide response for a Ni/TiO2/SiO2/n+p-Si sample in the dark (blue) and in the light (orange)

Figure 5.10, an illuminated n or p+n sample will retain its anodic and cathodic symmetry as well as experience a negative shift in potential. The presence of the anodic peak for n type silicon below is due to the photo-generated holes due to sample illumination [7]. Similar work was carried out by Mcintyre et al using an n-type and p+ type Si [8]. The CV trace of the p+-type anodes are too small to see the shape and peak to peak splitting but they do seem to fall in the same range as the work carried out here. The main aim of this test was to study the effect that the different types of TiO2 would have on the CV sweep and not the performance of underlying Si which is why it was carried out on the p++ type si.

As can be seen in figure 5.10 the voltage range for this experiment was set wide, a narrower range would potentially reveal further insight to the process however as the core aim was to determine the centre point this does not affect the overall aim of the experiment. Measuring the distance between the p++ and p+n. CV sweeps was the method used to obtain the amount of photovoltage achieved. The CV results for n+p Si sample can also be seen in figure 5.9 which was also tested under illumination. 4 nm of Platinum was deposited on top of the 6 nm TiO_2 protective layer to act as a HER catalyst. This n+p type silicon allows for a higher open circuit potential relative to the semiconductor electrolyte junction by decoupling the band-bending in the underlying Si and the electrode-electrolyte junction. This device is an attempt to overcome the inherent limitations that p-type Si devices encounter which is a low flat-band potential. As can be seen, there was not much of a positive shift when comparing the p++ and n+p CV scans in figure 5.9 with the final photo-voltage incurred being ~0.05V. Voltammetry using the n+p devices proved difficult with varying results and unexpected CV shapes. As these devices would be utilized in a tandem cell device it would be assumed that protons would be exchanged from the anode to the cathode through a proton exchange membrane which would acidify the area. In order to achieve better results running this experiment again in acidic media and utilizing longer wavelength light should be considered. as will be explained in following sections, the buried p+n and n+p junctions within the Si tends to lower the dependence that photo-voltage achieved has on the oxide layer thickness. One must ensure however, that light can still penetrate the protective layer and reach the underlying Si.

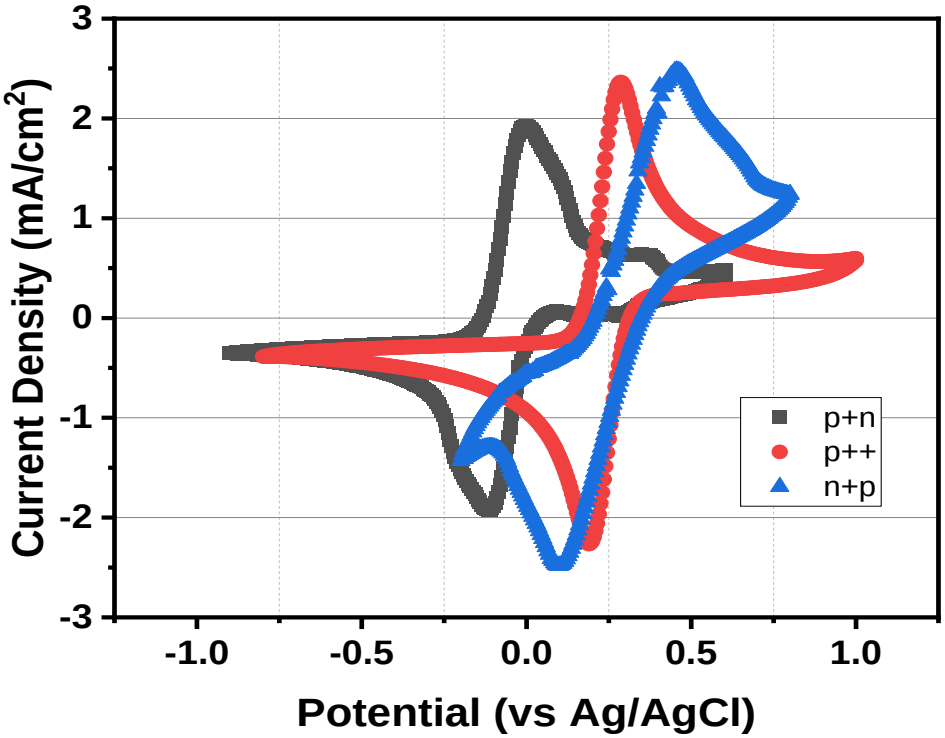

Figure 5.10: Ferri/ferrocyanide responses for p++, p+n and n+p devices. Each photoanode has a Ni/TiO2 catalytic and protective layer. Total photovoltage can be calculated by measuring the distance between the centre points of the CV response.

Approximately 0.29V for the photo-voltage using p+n and p++ and a photo-voltage of ~0.34V using the tandem p+n and n+p system was achieved in these experiments. As can be seen for the n+p device, there is an almost negligible cathodic shift when compared with the result for p++ in the dark. A higher response than this was expected but from this result, the n+p type device do not seem suitable for use in a tandem photoelectrochemical cell. More research is needed to fully characterize this material and a longer wavelength light source might give more generated photo voltage.

Water oxidation curves can be seen below in figure (5.11). These electrochemical experiments were carried out in a basic pH electrolyte under standard conditions, ie ~20ºC at atmospheric pressure. The work carried out by McIntyre et al shows the oxidation curves using n-type Si with a Ir catalytic layer and a TiO2 underlying protective layer in pH0, pH7 and pH14 electrolyte solution. In acidic conditions the potential required to facilitate the oxidation of water is ~1.23V () although a potential even greater than this would be required in reality due to the ohmic losses

(5.1)

in the system and over potential required to sustain the reaction. The pH of our electrolyte solution is ~pH11 and so:

$$E_{0_2} = (1.23V) - (0.059V)(pH)$$
$$E_{0_2} = 0.64V$$

Focusing just on the pH7 and pH14 CV sweeps, when comparing the onset potential vs the oxidation potential for water at the appropriate pH there was a 0.219V and 0.171V negative shifts observed respectively. As previously discussed, this is what is expected as when the light interacts with the underlying Si, photo-genrated hole-electron pairs are created. The holes then are available to facilitate the oxidation of water at the interface. This would be due to the higher concentration of holes being available for reaction due to the p-type region. The result below will be directly compare dwith Mcintyre's work using the n-type Si in 1MNaOH [7]. The blue trace in figure (5.11) below shows the water the data from a p+n photoanode device. A 3mm Ni catalyst was present on the surface to facilitate the reaction. As mentioned, In the case of this work p+n-Si is used instead of n-Si and so a greater negative shift in potential is expected due to the abundant availability of charge carriers however, this is not the case as can be seen when comparing the onset potential in figure 5.11 to the calculated oxidation potential of the electrolyte solution. McIntyre's onset poteintial seems to be ~0.2V while in Fig 5.11 it is ~0.6V. Granted the two enviroments are different here as different electroylyte is used as well as catalyst but with the p+n Si, a more comparable onset potential was expected. A larger negative potential shift from the oxidation potential was expected here due to the p+ region and the photocurrent is also significantly lower than in the work carried out by McIntyre. There could be a few reasons for this, number one being that McIntyre had a layer of Ir on the surface which is known to act as a better Oxygen evolution catalyst than the Ni used in this work. The second most likely reason for this result is due to the greater thickness of TiO2 protective layer which inhibits/ slows the charge carrier as it travels to the catalyst-electrolyte interface. Another factor could be that the delay between fabrication of these samples and testing could have been too long and the thick layers could have degraded or oxidised which would inhibit charge transfer, as seen in the study of different deposition techniques discussed previously. Continuous use of the samples can also cause the surface to deteriorate due to constant reactions at the surface.

Although the expected result was for a large negative shift, greater or comparable to the one seen in the work from McIntyre, the above mentioned points are the likely contributing factors to this, as well as maybe something as simple as a bad contact, or even a corroded platinum wire as the same one was used for the majority of the electrochemical work.

When calculating the photovoltage shift in this work, we are comparing results in figure 5.5 and 5.11. Figure 5.5 above shows the water oxidation curve for p++ sample in the dark where it can be seen that the oxidation started to occur at ~1.75V whereas when carrying out the same test using the p+n sample under illumination (figure 5.11) this occurs at 0.6V. this is a negative shift of 1.1V. This anodic shift seems very large when comparing results to the work of McIntyre et el [7] with FFC. He had obtained a anodic shift of 600mV using n type Si and p+ Si. In this work, p+n type Si and p++ Si was used which should have better charge transfer kinetics but it still seems high when taking this into account. The photo-voltage achieved in the work carried out in FFC earlier in the chapter was only ~0.25V and so this perhaps points to something else within the circuit causing the additional anodic shift. It is unlikely that this photo voltage is a true result but the reason for this large discrepancy is not definitively known.

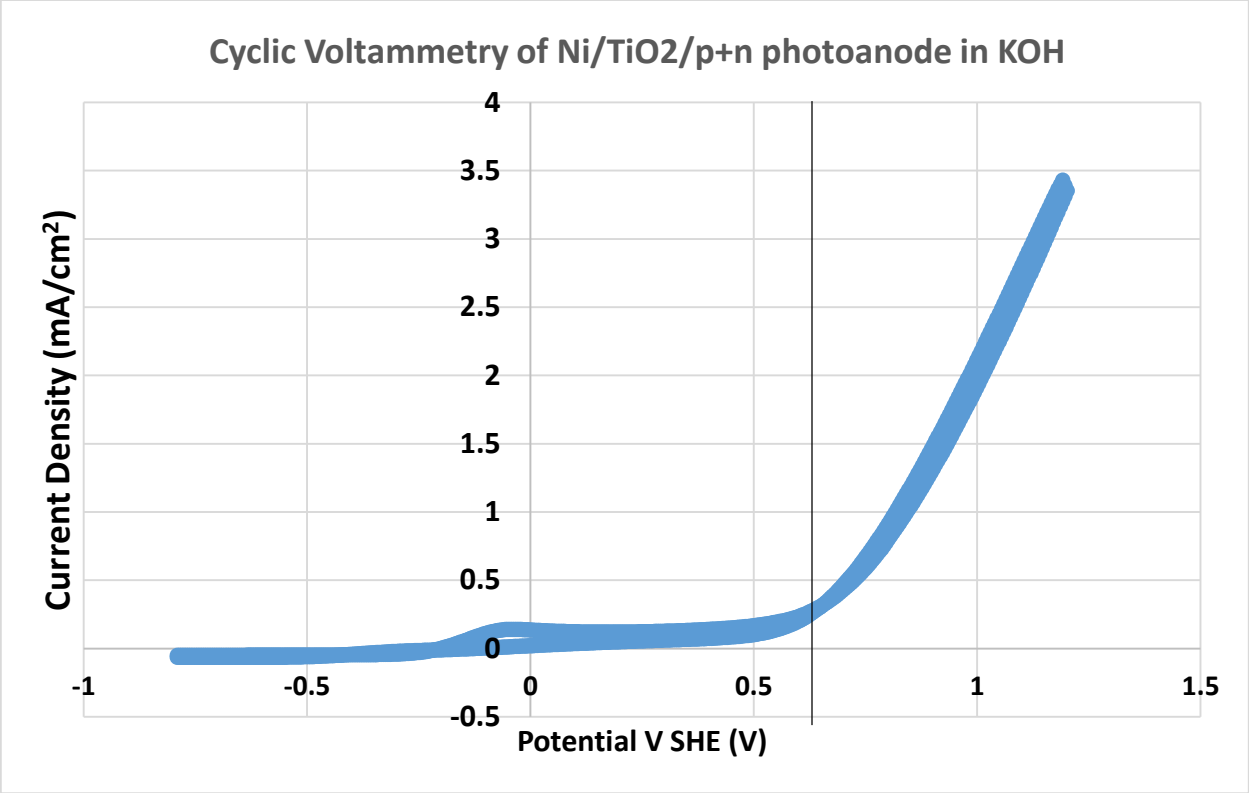

Figure 5.11: KOH cyclic voltammetry response for a Ni/TiO2/SiO2/p+n-Si sample showing the water oxidation curve. The calculated oxidation potential of water at this pH is ~ 0.6V. The black line is located at this E_{o2} potential.

Next was the n+p type silicon sample. Unfortunately, when cyclic voltammetry was carried out using these devices, regardless of illumination or dark conditions, the resulting photocurrent/ voltage was essentially 0. The reading from the potentiostat was in the 0-10µA range with no recognisable peaks or troughs when the CV was carried out over a range of -1V to 2V. As the potentiometer seemed to be working fine for other tests, this result can probably be put down to the samples themselves or the connection to the device. The gasket between the liquid and sample could have leaked causing the circuit to short, or the wire/photoelectrode sample could have disconnected.

As p-type Si is more suitable as a photocathode, due to the built in depletion region which provides a high concentration of electrons at the surface independent of the semiconductor electrolyte interface. N+p type Si has shown to be one of the most efficient types of material when it comes

to HER for this reason [10]. Looking at some other works, we can see what would have been expected from our n+p CV result. Segar et al carried out CV experiments using similar n+p Si devices but used a Moleybdenum sulphide layer as the HER catalyst. Previous work carried out by the group found that alloys of nickel and molybdenum (NiMo) may work as non-precious HER catalysts for this system. However, this system has stability issues in acid, which limits the pH to values above 4. Regardless of this, CV experiments were carried out in acidic electrolyte (1M $HClO_4$). The HER activity of the MoSx/n+pSi photoelectrode surpasses that of a pure n+p-Si electrode, suggesting a catalytic effect from MoSx. When MoSx is deposited on a Ti-protected n+p-Si electrode, the onset of photocurrent significantly shifts to more positive potentials (0.33 V vs. RHE), approaching the efficiency of a Pt electrode (0.47 V vs. RHE). Although this study was more about the performance of the overlaying catalyst than the n+p type Si, photovoltages of ~0.5V were obtained. When considering what would be expected from the n+p devices from our work, a positive potential shift would be expected when compare with the water reduction potential of ~0.8V [11].

Similar work was also carried out by Boettcher et al using the n+p type Si as a photocathode. This work utilized both planer Pt n+p and Pt/n+p Si nanowires with good photovoltaic results. These electrodes exhibit a notably high open-circuit voltage of ~0.55V with the planer electrodes achieving 28mA/cm^2. When regular planer p type Si was used in the same work under same conditions, a photocurrent of ~21mA/cm^2 was achieved which tells us that the high concentration of implanted carriers on the surface has a positive effect on the overall performance. Moreover, their high fill factor (~0.60) underscores the efficient electrocatalytic performance of the thin Pt film. The energy conversion efficiency of 9% achieved is in line with previous work already carried out using these same materials. The disparity on efficiencies between photocathodes and anodes is due to the due to the large work function, significant electron–electron scattering and strong surface reflection of incident light that p type semiconductors have [12]

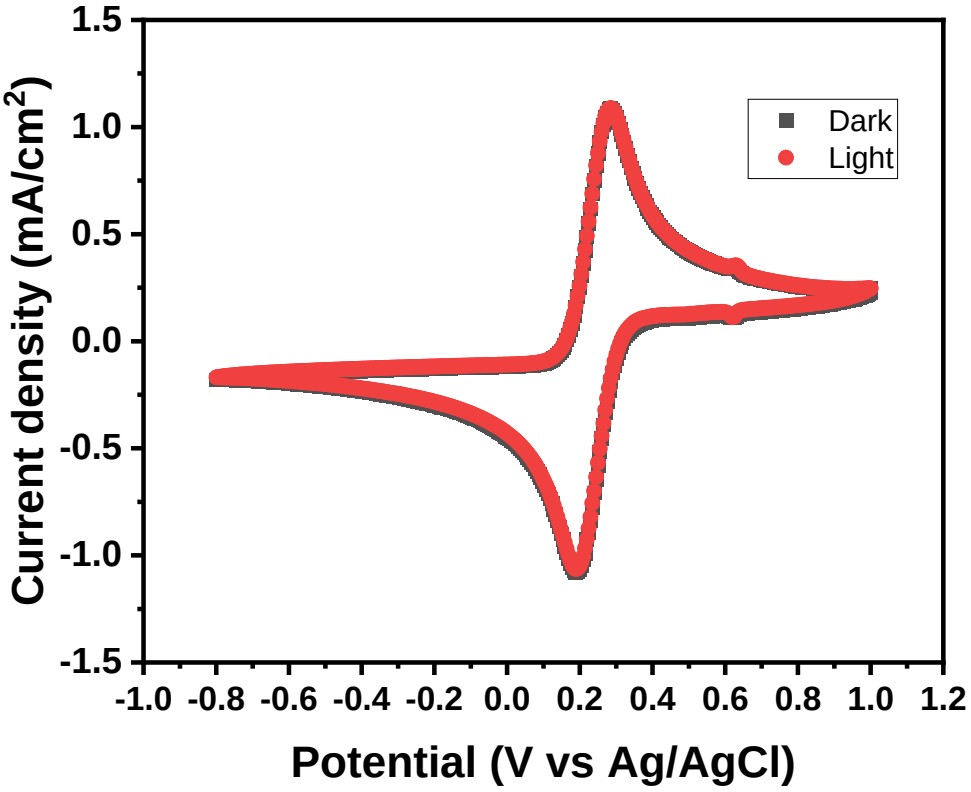

Figure 5.12: Ferri/ferrocyanide Cyclic voltammetry response for a Ni/TiO2/SiO2/p++-Si sample in the dark and under illumination

The CV responses for a p++ Si photoanode in the dark and under illumination can also be seen in figure 5.12. A catalytic layer of Ni was deposited on the surface to facilitate the electrochemical reaction. The absence of any response to the light confirms the high degree of doping present within the p++ Si due to it behaving more like a metal than a semiconductor under illumination.

5.4 Conclusion & further work

The aim of this study was to obtain a better understanding of how effective TiO_2 can be when used as a protective layer for photoanodes and to test the functionality of different types of Si as a photoelectrode. The TiO_2 was prepared using differing ALD and PEALD methodologies, for example, low oxygen environments, high oxygen environments and post deposition annealing. The non-stochiometric nature of the films produced under high oxygen, low oxygen compared to PEALD showed a spread out of peak to peak voltage and thus an increase in resistivity. This points towards the conclusion that the ratio of Ti^{3+} to Ti^{4+} is one of the main factors that affects the resistivity of the device and thus the leakage current.

The method of obtaining photovoltage here was measuring the distance between the midpoints of the CV scan for the p+n device under illumination and the p++ device measured in the dark. The p+n device produces more photocurrent than the regular n-Si device which was expected due to the higher hole density at the interface. The measured photovoltage achieved was ~ 0.41 V. The measured photovoltage using a tandem device i.e., p+n photoanode and n+p photocathode was also measured but only achieved a photovoltage of 0.07 V greater than the single photoanode device. More voltage was expected from this device and further work would need to be carried out to optimize the system. Thickness also played a part in the TiO_2 conductivity. There was a decrease in resistivity as the thickness was decreased which would point to the conclusion that tunnelling was the dominant transport mechanism. Just 6 nm of TiO_2 was found to be an effective protection layer against corrosion as can be seen from the chronoamperometry experiments although the SEM images do indicate that there is corrosion of the photoanode surface. The photocathode CV work would also be redone on the n+p device to obtain actual photo voltage and current results so that a full picture of overall efficiencies could be achieved. The photocurrent and voltage achieved during the water electrolysis experiments was substantially lower than in the work of McIntyre et al. Although different catalysts were used and different type of underlying Si, a greater effect was expected when comparing illuminated and dark CV data. This can probably put down to several small factors such as the electrolyte itself, the deterioration of the samples over time and the connection in the circuit as well as other factors mentioned in the previous section.

To back up this work more compositional characterization could be undertaken e.g., XPS, in order to further characterize the TiO_2 films. Being able to determine the Ti3+/Ti4+ ratio in section 5.2.1

would be beneficial and make the results more conclusive. Further electrical measurements would also be beneficial, for example the fabrication of a metal oxide semiconductor device to calculate the leakage current. 2 point and 4-point resistivity and AC Hall measurements were performed but the thickness of the films pushed the resistivity too high for conclusive data as measurements outside accepted error limits of the instrumentation. If these measurements were to be conducted again, several different TiO_2 samples of greater thickness could be measured and results could be extrapolated to obtain an estimate of the for Hall voltage, resistivity etc. It should however be acknowledged that thin films are needed for protection layers and any materials properties may be thickness dependant and should be treated with caution. High resolution SEM or TEM where not available at the time of this study, these would be beneficial determine not just better thickness measurements but the presence of interlayers and more detail of electrode damage after use.

Bibliography

[1] Q. Xie, J. Musschoot and D. Deduytsche, "Growth Kinetics and Crystallization Behavior of TiO2 Films Prepared by Plasma Enhanced Atomic Layer Deposition," *Journal of The Electrochemical Society*, vol. 155, pp. 688-692, 2008.

[2] X. Qi, J. Yulong and C. Detavernier, "Atomic layer deposition of TiO2 from tetrakis-dimethyl-amido titanium or Ti isopropoxide precursors and H2O," *Journal of Applied Physics, vol. 545, pp. 176-182,* 2007.

[3] S. Ali and M. Khan, "Annealing effects on structural, optical and electrical properties of TiO2/FTO heterojunction," *Applied Physics, vol. 8, pp. 249-252,* 2020.

[4] A. Bakri, M. Sahdan and F. Adriyanto, "Effect of annealing temperature of titanium dioxide thin films on structural and electrical properties," *AIP*, vol. 7(6), pp.___ 2017.

[5] Y. Xu, S. Wu, P. Wan, J. Suna and Z. Hood, "Introducing Ti3+ defects based on lattice distortion for enhanced visible light photoreactivity in TiO2 microspheres," *RSC Advances, vol. 7, pp. 32461-32467,* 2017.

[6] F. Zuo, L. Wang, T. Wu and Z. Zhang, "Self-Doped Ti3+ Enhanced Photocatalyst for Hydrogen Production under Visible Light," *American Chemical Society, vol.* 132(34), pp. 11856-11857, 2010.

[7] Y. Chen, J. Prange, S. Duhnen and Y. Park, "Atomic layer-deposited tunnel oxide stabilizes silicon photoanodes for water oxidation," *Nature Materials, vol. 10, pp.539-544,* 2011.

[8] A. Scheuermann, J. Prange, M. Gunji and C. Chidsey, "Effects of catalyst material and atomic layer deposited TiO2 oxide thickness on the water oxidation performance of metal–insulator–silicon anodes," *Royal Society of Chemistry,* vol. 6, pp. 2487-2496, 2013.

[9] J. Lawrence, A. Meng, K. Tang, H. Olivia and C. Chidsey, "Titanium Oxide Crystallization and Interface Defect Passivation for High Performance Insulator-Protected Schottky

Junction MIS Photoanodes," *Applied Materials and Interfaces*, vol. 8, no. 23, pp. 14596-14603, 2016.

[10] R. Fan, Z. Mi and M. Shen, “Silicon based photoelectrodes for photoelectrochemical water splitting,” *Optics Express*, vol. 27, no. 4, pp. 51-80, 2019.

[11] B. Seger, A. Laursen, P. Vesborg, T. Pedersen "Hydrogen Production Using a Molybdenum Sulfide Catalyst on a Titanium-Protected n+p-Silicon Photocathode" *Angewandte Chemie*, vol. 51, no. 36, pp. 9128-9131, 2012.

[12] S. Boettcher, E. Warren, M. Putnam, E. Santori, D. Turner-Evans "Photoelectrochemical hydrogen evolution using Si microwire arrays" *Journal of the American Chemical Society*, vol. 133, no. 5, pp. 1216-1219, 2011

Appendix 1

EDX Data

Figures A1 and A2 show the corresponding EDX spectrum to the light and dark regions of the SEM image 5.9 (b) above in section 5.3 as well as the percentage weight and Atomic percentage of each element within the sample area. Also included are further SEM and EDX data which was taken of the sample.

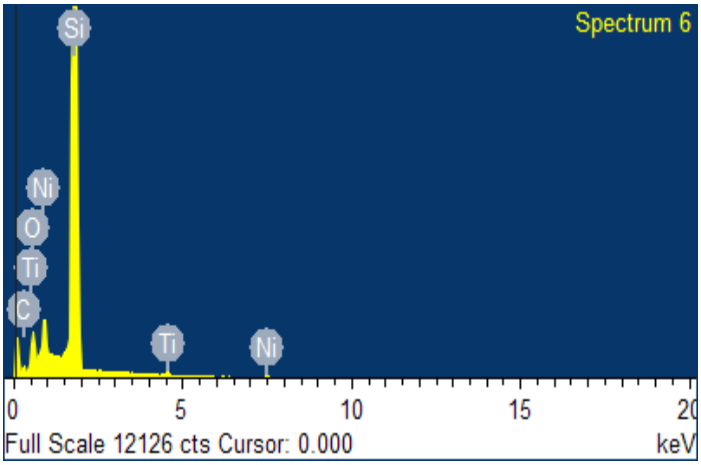

Element	Weight %	Atomic %
C K	3.65	8.15
O K	3.15	5.27
Si K	88.44	84.32
Ti K	0.97	0.54
Ni L	3.80	1.73
Totals	100.00	

Figure A1: Corresponding EDX spectrum from fig 5.9(b) of the lighter region of the used anode indicating the presence of Ti and Ni

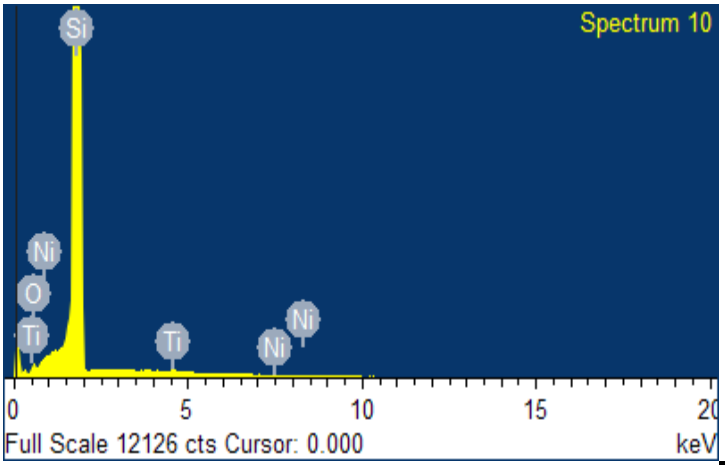

Element	Weight %	Atomic %
O K	1.56	2.70
Si K	98.30	97.22
Ti K	0.14	0.08
Ni K	0.00	0.00
Totals	100.00	

Figure A2: EDX spectrum of the darker region of the used anode where no Ni was detected and a greatly reduced amount of Ti present in comparison to the lighter regions.

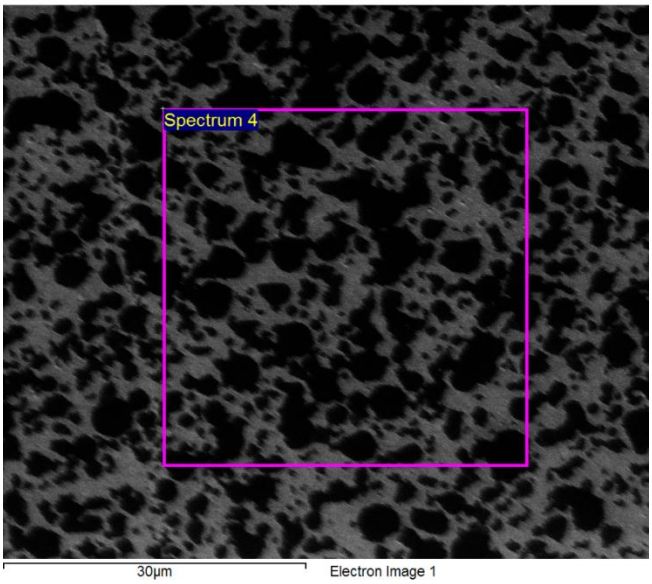

Element	Weight%	Atomic%
O K	1.94	3.36
Si K	97.55	96.38
Ti K	0.21	0.12
Ni K	0.30	0.14
Totals	100.00	

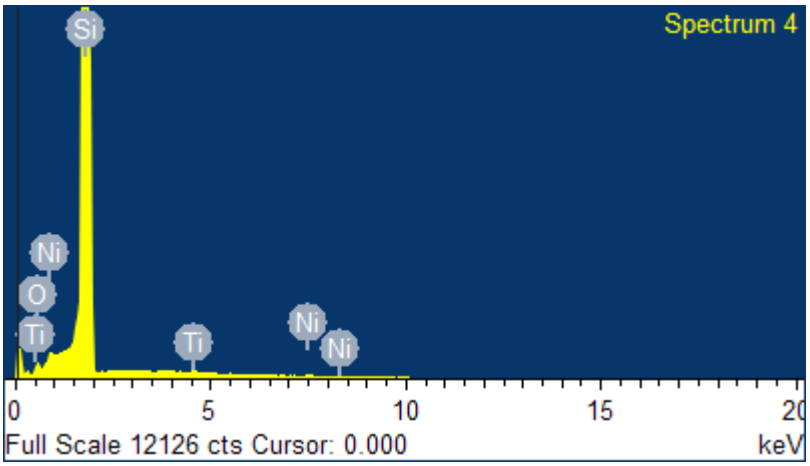

Figure A3: SEM image and EDX spectrum of a wider region of the used anode along with the percentage composition of the test area.

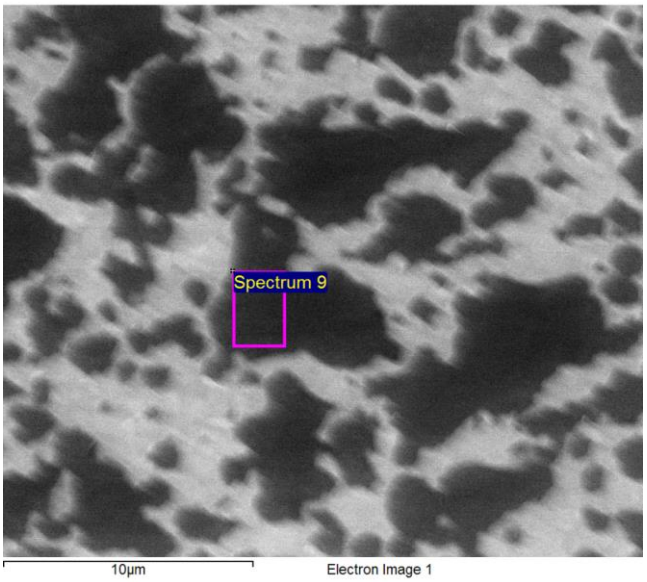

Element	Weight%	Atomic%
O K	1.43	2.49
Si K	98.38	97.40
Ti K	0.19	0.11
Ni K	0.00	0.00
Totals	100.00	

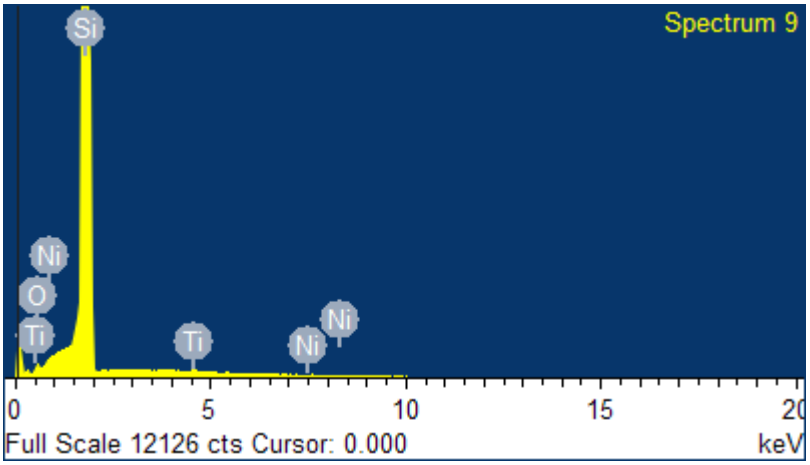

Figure A4: SEM image and EDX spectrum of a corroded area of the used anode along with the percentage composition of the test area.

Appendix 2

Extra Electrochemical experiments

Open circuit potential

When an electrode is submersed in an electrolyte, in this case KOH, it will adopt an open circuit potential. The open circuit potential is the built in voltage that exists in the system when there is no external bias is applied. This OCP was recorded for a Ni/TiO_2/SiO_2/Si anode deposited under regular ALD conditions where the thickness of the Ni and TiO_2 was 5nm and 25nm respectively. This measurement was taken over a very short time frame using a saturated calomel reference electrode (SCE) but then converted to V vs RHE. If this experiment was conducted over several hours, a decline in OCP would be expected. The OCP measured here was 0.535 V vs RHE.

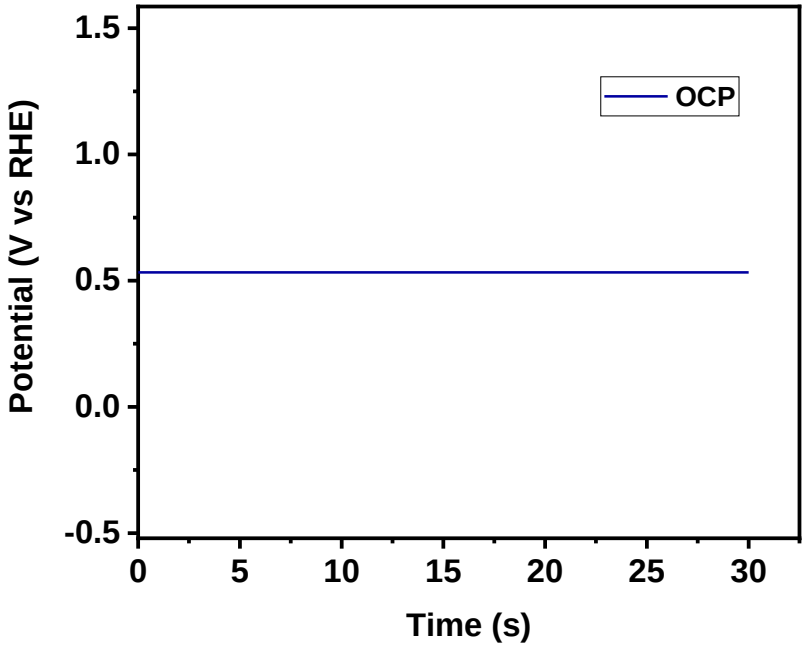

Figure 4A: Open circuit potential of Ni/TiO2/Si anode in the dark using KOH as an electrolyte.

Chronoamperometry

Chronopotentiometry, like chronoamperometry, is an electrochemical technique that characterizes the stability of a device under test. Instead of a constant potential being applied, a constant current is applied and the corresponding change in potential is recorded over time. This method resulted in relatively noisy results which wouldn't have been acceptable for this work and for this reason chronoamperometry was selected as the main stability test. These inaccuracy's could be contributed to the equipment used or due to the chosen applied which in hindsight was much too low for experiments of this nature. Both of these stability techniques return similar results and so it had no effect on the outcome of the experiments. Figure 4B shows one of the better chronopotentiometry experiments which was conducted on a p++Ni/TiO_2/Si sample using an Ag/AgCl reference electrode. This experiment was concluded early as can be seen by the time scale whereas these experiments would usually be conducted for hours at a time.

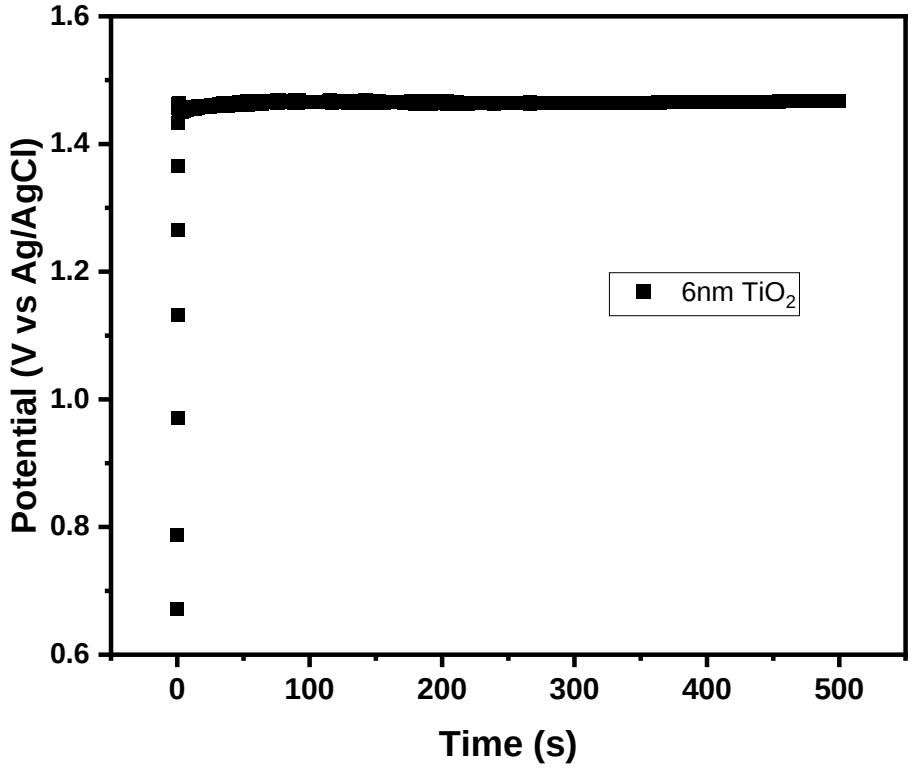

Figure 4A: Chronopotentiometry result for 6nm of TiO_2 on Ni/TiO_2/p++Si sample submerged in pH 14 KOH where 1.5 mA is applied.

Appendix 3

Further works.

Currently preparing a paper from this work titled *"A study of degradation and performance of a TiO_2 photoanode protective layer under oxidative conditions".*

The Electrochemical Society

(Digital Presentation) Electrode and Electrolyte Materials for Thin Film Microbatteries

Contributed to this work by way of surface modification of the V_2O_5 via thermal annealing and depositing a thin Al_2O_3 layer on top to help improve charge-discharge kinetics of the battery.

Appendix 4

Research presentation (Tyndall, QUB, Stanford)

Emerald Project: Emerging Materials for Energy storage and Environmental Research enabled through Atomic Layer Deposition

Tyndall National Institute

► *Overall goal*: Create alternative fuel source (Hydrogen) from the sustained photoelectrochemical splitting of brine and the production of Cl_2 / NaOH / NaOCl (Hypochlorite) from this process.

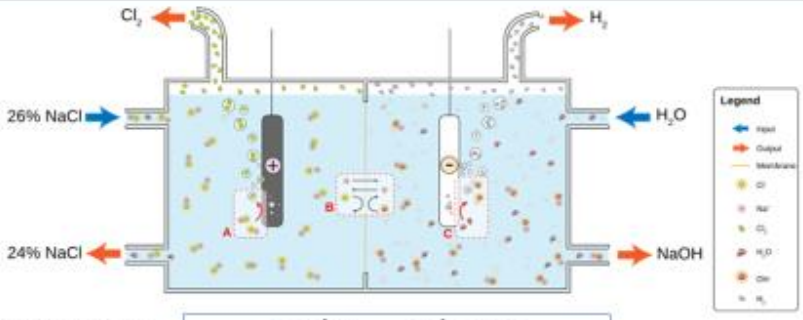

► Reaction at Anode ► $2Cl^- \longrightarrow Cl_2 + 2e^-$

► Reaction at Cathode ► $2H_2O + 2e^- \longrightarrow H_2 + 2OH^-$

► Reaction near Anode ► $Cl_2 + 2NaOH \longrightarrow NaCl + NaOCl + H_2O$

Previous Project Work

RENEW Project

TiO2 – RuO2 alloyed thin films were produced by method of ALD.
Photo voltages above 500 mV were consistently achieved regardless of film thickness.

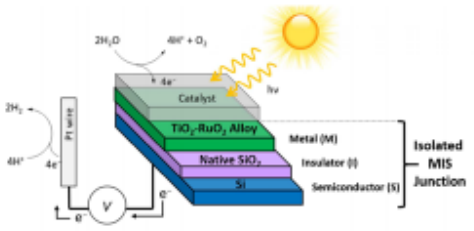

Photoanode using the isolated MIS structure

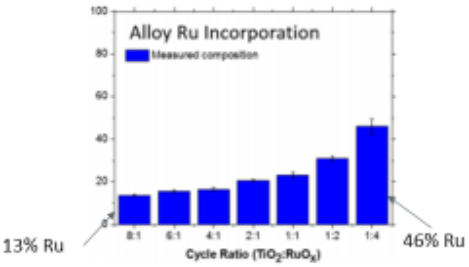

- Alloying TiO_2 and RuO_2 has stabilizing effect, reduces TiO_2 resistivity
- Boosted Work function to ~ 5.2eV
- TiO_2 highly stable under water oxidation conditions.

A. Scheuermann, O. Hendricks, M. Schmidt, *Applied Materials and Interfaces*, vol. 8, no. 36, p. 23763–23773, 2016.

Substrates

Si wafers used:

- n-type
- p++
- p+n
- n+p

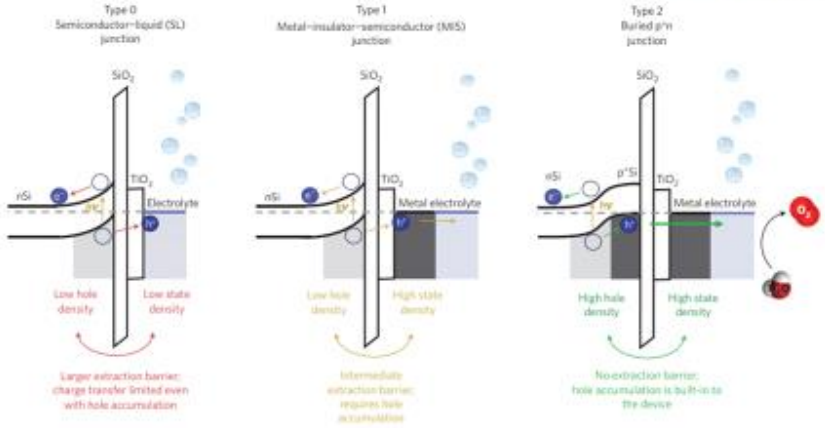

Schematic of an n+p Si substrate with a TiO2 protective layer

Scheuermann, J. Lawrence, K. Kemp "Design principles for maximizing photovoltage in metal-oxide-protected water-splitting photoanodes," Nature Materials, vol. 15, pp. 99-105, 2016.

Results

Hall Measurements

► *Deposition temp: 100°C*

AC Hall measurements				
Property	Units	AC Geo. C	AC Geo. D	AC Geo. avg.
Frequency	Hz	100m		
Response	none	slow		
Sensitivity	V	0.0005		
AC Gain	dB	0		
Hall B-field RMS	T	1.24		
Hall excitation current	A	2E-7		
AC Hall hold time	s	2		
AC Hall voltage	V			5.11712E-4
Phase	degree	174.3, 179.9	176.2, 176.1	173.4
Type/100%	none	N/100%	N/100%	N
AC Hall mobility μa	$cm^2V^{-1}s^{-1}$			0.22418
Sheet carrier concentration	cm^{-2}			7.4627E10
Carrier concentration	cm^{-3}			
$R_{H\text{-}sheet}$	cm^3/C	1.3969E7	1.3391E7	8.4126550E7
R_H	cm^3/C			
AC Hall SNR est.	none			14.9:1

► *Deposition temp: 130°C*

AC Hall measurements				
Property	Units	AC Geo. C	AC Geo. D	AC Geo. avg.
Frequency	Hz	100m		
Response	none	slow		
Sensitivity	V	0.0005		
AC Gain	dB	0		
Hall B-field RMS	T	1.24		
Hall excitation current	A	2E-7		
AC Hall hold time	s	2		
AC Hall voltage	V			4.87931E-4
Phase	degree	174.3, 179.9	176.2, 176.1	177.88
Type/100%	none	N/100%	N/100%	N
AC Hall mobility μa	$cm^2V^{-1}s^{-1}$			0.19798
Sheet carrier concentration	cm^{-2}			8.1589E11
Carrier concentration	cm^{-3}			
$R_{H\text{-}sheet}$	cm^3/C	1.3969E7	1.3391E7	1.5757E7
R_H	cm^3/C			
AC Hall SNR est.	none			28.5:1

► *Deposition temp: 150°C*

AC Hall measurements				
Property	Units	AC Geo. C	AC Geo. D	AC Geo. avg.
Frequency	Hz	100m		
Response	none	slow		
Sensitivity	V	500μ		
AC Gain	dB	0		
Hall B-Field RMS	T	1.24		
Hall excitation current	A	100n		
AC Hall hold time	s	2		
AC Hall voltage	V			3.3725E-4
Phase	degree	174.3, 179.9	176.2, 176.1	176.65
Type/100%	none			N
AC Hall mobility μa	$cm^2V^{-1}s^{-1}$			0.153
Sheet carrier conc.	cm^{-2}			4.5730E11
Carrier concentration	cm^{-3}			
$R_{H\text{-}sheet}$	cm^3/C	1.3969E7	1.3391E7	1.3680E7
R_H	cm^3/C			
AC Hall SNR est.	none			5.8?:1

4

Hall Results (SnO2 @ 100, 130, 150°C)

Recorded data graphed vs deposition temperature:

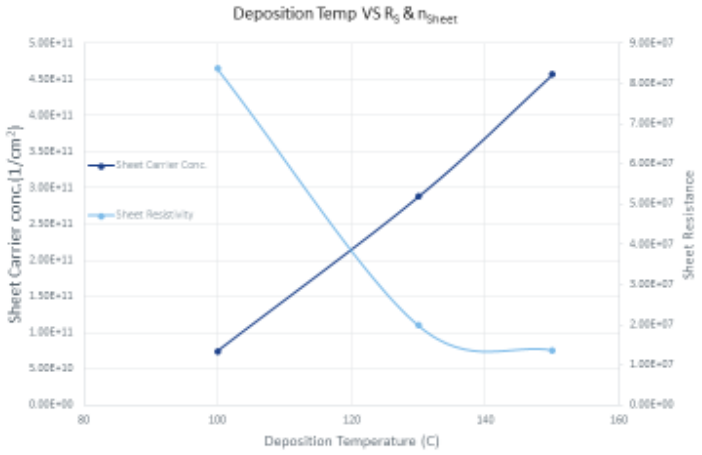

Samples

All films were deposited on each of the 4 substrates, n-type, p++, p+n, n+p

Thermal ALD (°C)	PE-ALD (°C)
125	125
170	170
200	200
250	250

- Regular conditions
- Under dosed O* plasma
- Plasma pulse followed by O gas pulse

- Desired thickness of 6nm of TiO_2
- Anything less would not have longevity in CV conditions
- Thicker films would inhibit carrier transport to the Si substrate

Photo-electrochemical Characterization

Cell Design

- Central part of system is PFTE cell
- Electrolyte is pumped through to allow circulation
- Opening roughly 1cm^2 but illumination area determined by base plate

- Reference electrode to be used is Ag/AgCl which has standard potential of +199mV vs SHE

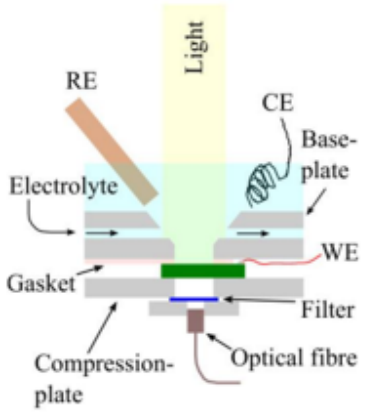

J. Kegal, 2018 'Fabrication and characterization of ZnO-based water splitting devices by atomic layer deposition and hydrothermal synthesis', PhD, Tyndall National University

Cyclic voltammetry / Linear sweep voltammetry

- CV monitors the redox behavior of a known chemical species:

$$Fe(CN)_6^{-4} \longrightarrow Fe(CN)_6^{-3} + e$$

- Potential applied across *working* & *reference* electrode while current measured across *working* & *counter* electrodes.
- Reference electrode Ag/AgCl

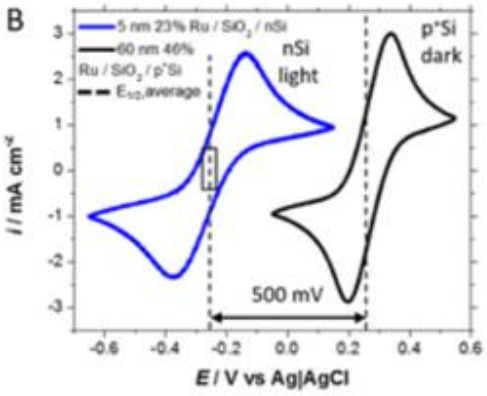

O. Hendricks, A. Scheuermann, M. Schmidt "Isolating the photovoltaic junction: atomic layer deposited TiO2-RuO2 alloy" *Applied Materials and Interfaces*, vol. 8, no. 36, p. 23763–23773, 2016.